

UNIVERSITY OF OKLAHOMA

GRADUATE COLLEGE

OBSERVATION AND PROPERTIES OF  $X(3872)$  AT DØ

A DISSERTATION

SUBMITTED TO THE GRADUATE FACULTY

in partial fulfillment of the requirements for the

degree of

Doctor of Philosophy

By

ISAAC N. C. HALL

Norman, Oklahoma

2007

UMI Number: 3293145



---

UMI Microform 3293145

Copyright 2008 by ProQuest Information and Learning Company.  
All rights reserved. This microform edition is protected against  
unauthorized copying under Title 17, United States Code.

---

ProQuest Information and Learning Company  
300 North Zeeb Road  
P.O. Box 1346  
Ann Arbor, MI 48106-1346

OBSERVATION AND PROPERTIES OF  $X(3872)$  AT DØ

A DISSERTATION APPROVED for THE  
HOMER L. DODGE DEPARTMENT OF PHYSICS AND ASTRONOMY

BY

---

Braden Abbott, CHAIR

---

Chung Kao

---

Phillip Gutierrez

---

Neil Shaffer-Ray

---

John Albert

©Copyright by ISAAC N. C. HALL 2007  
All Rights Reserved.

*To my wife, Heather*

*and*

*To my parents, Phillip and Marian*

## Acknowledgments.

I would like to acknowledge the help and assistance given to me by my many friends and family members. Without their help, none of this would be possible. My parents, Phillip and Marian, my wife, Heather, and my sisters, Felicia, Monica and Amelia.

I would also like to thank the many friends I have made over the course of these years (in no particular order). In Oklahoma, Dave Hawkins, Will Hawkins, Kevin Lewis, Larry Maddox, Jim Hicks, and Blake Laing, and many more. In Illinois, Andrew Askew, Angela Bellavance, Greg Davis, Mike Cooke, Amber Johnson, Marty Murphy, Tom Diehl, Brenna Flaughner, Satish Desai, Mandy Rominsky, Reinhard Schweinhorst, Sorhab Hossain, and Miroslav Kopal, as well as Erik Plotner, Andrew Lohse, and all of the members of the Chicago Athletics Baseball Club.

I would like to acknowledge the hard work by my advisor, Brad Abbott, that helped me get to this point and my undergraduate advisor, Saeed Shadfar, without whom, I may never have chosen physics as my major. I would also like to thank the many baseball coaches I have had over the years, especially Denney Crabaugh and Keith Lytle at Oklahoma City University. Playing for them was perhaps one of the

greatest experiences of my life, and a big factor in making me the person I am today.

# Contents

<b>List of Tables</b>	<b>xiii</b>
<b>List of Figures</b>	<b>xix</b>
<b>1 Introduction</b>	<b>1</b>
1.1 Overview of the Standard Model	1
1.1.1 Mesons and Baryons	4
1.1.2 Isospin, $C$ and $P$ Parity	5
1.2 Discovery of $X(3872)$ at Belle and Motivation for Study at DØ	8
<b>2 Theoretical Interpretations of <math>X(3872)</math></b>	<b>10</b>
2.1 Observed Properties of the $X(3872)$	10
2.2 Charmonium Interpretation	13
2.2.1 $1^1D_{2-+}$ State	16
2.2.2 $2^3P_{0++}$ State	17
2.2.3 $2^3P_{1++}$ State	17



2.2.4	$2^3P_{2++}$ State . . . . .	18
2.2.5	$3^1S_{0-+}$ State . . . . .	18
2.2.6	Summary of Charmonium States . . . . .	19
2.3	Meson-Molecule Interpretation . . . . .	19
2.4	Diquark-Antidiquark Interpretation . . . . .	21
2.5	Summary . . . . .	21
<b>3</b>	<b>Experimental Apparatus . . . . .</b>	<b>23</b>
3.1	Introduction . . . . .	23
3.2	The Tevatron Accelerator . . . . .	23
3.3	Interactions of Particles with matter . . . . .	26
3.3.1	Electrons and Photons . . . . .	27
3.3.2	Muons . . . . .	28
3.3.3	Hadrons . . . . .	29
3.3.4	Neutrinos . . . . .	29
3.4	The DØ Detector . . . . .	29
3.4.1	Coordinate System . . . . .	30
3.4.2	The Central Tracking System . . . . .	32
3.4.3	Solenoid . . . . .	38
3.4.4	Pre-shower Detector . . . . .	39
3.4.5	The DØ Calorimeter . . . . .	41

3.4.6	Muon System . . . . .	46
3.5	Trigger . . . . .	48
3.5.1	Level 1 Trigger . . . . .	49
3.5.2	Level 2 Trigger . . . . .	50
3.5.3	Level 3 Trigger . . . . .	52
<b>4</b>	<b>Event Reconstruction . . . . .</b>	<b>53</b>
4.1	Track Reconstruction . . . . .	54
4.1.1	AATrack . . . . .	54
4.1.2	Histogramming Track Finder . . . . .	56
4.1.3	Track Selection . . . . .	56
4.2	Vertex Reconstruction . . . . .	60
4.2.1	Vertex Fitting . . . . .	62
4.3	Muons . . . . .	62
4.4	Photon Reconstruction . . . . .	66
4.4.1	The CellNN Algorithm . . . . .	66
<b>5</b>	<b>Event Selection . . . . .</b>	<b>69</b>
5.1	Dimuon triggers . . . . .	70
5.2	Dimuon Skim . . . . .	71
5.3	$J/\psi\pi^+\pi^-$ candidate selection . . . . .	73
5.4	$J/\psi\gamma$ selection . . . . .	79

<b>6</b>	<b>Analysis of <math>X(3872) \rightarrow J/\psi\pi^+\pi^-</math></b>	<b>82</b>
6.1	Monte Carlo Simulation	82
6.2	Mass Measurement	83
6.2.1	Systematic Error	86
6.3	Comparison to $\psi(2S)$ Charmonium State	88
6.4	Lifetime Analysis	90
6.5	Summary of Results	98
<b>7</b>	<b><math>X(3872) \rightarrow J/\psi\gamma</math> Analysis</b>	<b>99</b>
7.1	Monte Carlo Simulation of Expected Signals	101
7.2	Backgrounds	105
7.2.1	Sources of Background	106
7.3	Lifetime Analysis	109
7.3.1	Simultaneous Mass and Lifetime Fitting	112
7.4	Limit on the ratio $\frac{BR(X(3872) \rightarrow J/\psi\gamma)}{BR(X(3872) \rightarrow J/\psi\pi^+\pi^-)}$	116
7.4.1	Bayesian Limit Calculation	120
7.5	Summary of Results	123
<b>8</b>	<b>Summary of Results</b>	<b>127</b>
8.1	Observation of $X(3872)$	127
8.2	Search for $X(3872)$ Decaying to $J/\psi\gamma$	128

<b>Bibliography</b>	<b>129</b>
---------------------	------------

## List of Tables

1.1	The three generations of quarks and leptons . . . . .	3
1.2	The force carriers of the Standard Model . . . . .	4
2.1	Summary of charmonium spectrum. States that have yet to be observed by experiment are given masses at their expected values. States at $2D$ , $3P$ , $3D$ and higher are not listed as they are expected to be too heavy to even consider as candidates for the $X(3872)$ , as are states with $L > 2$ . . . . .	16
3.1	Specifications of the various sensors in the DØ silicon detector. $i$ indicates the inner H-disk sensor while $o$ indicates the outer H-disk sensor.	35
3.2	DØ Central Calorimeter Parameters. . . . .	43
3.3	DØ Endcap Calorimeter Parameters. IH denotes Inner Hadronic cells. MH denotes Middle Hadronic cells. OH denotes Outer Hadronic cells.	44
4.1	Muon nseg definitions. . . . .	65
6.1	$J/\psi\pi^+\pi^-$ mass fit results with a bin width of 0.01 GeV. . . . .	87

6.2	Yields of $\psi(2S)$ and $X(3872)$ for different ranges of variables. The fitted widths of $\psi(2S)$ and $X(3872)$ are not constrained in the initial selection, however over the ranges listed in these tables, the Gaussian widths for $\psi(2S)$ and $X(3872)$ are fixed to the values obtained in the fit over the full sample. The uncertainties in this table reflect only the uncertainty in fitted Gaussian normalization and do not reflect the small uncertainties in background . . . . .	90
7.1	Results of separate methods of mass fitting. Due to the similarity of the $B$ decay and sideband contributions, mass fit results are unstable.	111
7.2	Results of $J/\psi\gamma$ simultaneous mass and lifetime fit. Note that widths of prompt double Gaussian were fixed from the $J/\psi$ lifetime fit, as were their relative normalizations. . . . .	117
7.3	Values of parameters used to determine $N_{X \rightarrow J/\psi\gamma}^{pred R=1}$ . The terms $N_{X \rightarrow J/\psi\pi\pi}^{obs}$ , $N_{\psi(2S)}^{obs}$ are determined by imposing additional cuts on the muons of sample used in Chapter 6. Those cuts are $nseg > 1$ for each muon, and $p_T(J/\psi) > 7$ GeV and applying the same fitting procedure as in section 6.2 . . . . .	122

## List of Figures

3.1	Diagram of the Fermilab Tevatron Complex. . . . .	24
3.2	DØ Detector cutaway view. This is a standard DØ figure . . . . .	31
3.3	Closeup schematic of the DØ detector subsystems[54]. . . . .	33
3.4	Three dimensional view of the DØ Silicon Micro-strip Detector assembly. This is a standard DØ figure. . . . .	35
3.5	Track impact parameter resolution as a function of track transverse momentum for SMT only configuration and SMT+CFT configuration.[56]	36
3.6	One 'ribbon' assembly of the CFT showing the staggered configuration of two layers of fibers. This figure is a standard DØ figure. . . . .	38
3.7	Fractional $p_T$ resolution as a function of $\eta$ [54]. . . . .	39
3.8	Geometry of scintillating fibers in the pre-shower detectors.[54] . . . .	41
3.9	Geometry of forward pre-shower detector wedges.[54] . . . . .	41
3.10	Geometry of a Calorimeter Cell.[54] . . . . .	43

3.11	Layout of cells in the calorimeter. This figure is rotationally symmetric about the horizontal axis and exhibits symmetry of reflection about the vertical axis at $\eta = 0$ . [54]	45
3.12	Expanded view of PDT and MDT layout in the muon system. [54]	47
3.13	Expanded view of the scintillator layout in the muon system. [54]	48
3.14	Configuration of the Level 1 and Level 2 trigger systems. [54]	50
4.1	Sample track reconstruction with HTF. Plot a) shows the family of tracks that can be associated with a given hit. Plot b) shows the representation of the family of tracks associated with a given hit in curvature-azimuthal angle ( $\rho - \phi_0$ ) space. Plot c) shows the representation of 5 hits in $\rho - \phi_0$ space. The intersection of these lines indicate the values of the true parameter values for the track that generated these hits. Plot d) illustrates how these lines are used to fill a histogram, where the intersection is determined as the local maximum. [59]	57
4.2	Tracking efficiency in data measured with single muons. [61]	59
4.3	Distribution of $\log_{10}(p_T)$ for tracks from minimum bias events. The data distribution is taken from from a sample of $Z \rightarrow \mu\mu$ events.	61
4.4	Sample of a muon traversing a drift chamber. Tracks are constrained by the hits timing information to lie on circles (red) around the wires that contain hits. [63]	63



4.5	Floor cluster merging procedure in the CellNN algorithm.[68] . . . . .	67
5.1	Integrated luminosity at DØ from 2002 to the present. The data sample used in the following analyses were collected before August 2004, which is denoted by the vertical line. . . . .	70
5.2	Dimuon invariant mass spectrum in the $J/\psi$ mass window. . . . .	74
5.3	$M(\mu^+\mu^-\pi^+\pi^-) - M(\mu^+\mu^-)$ With only basic quality cuts applied. The invariant mass difference between the 4-particle candidate and the dimuon candidate is used in place of the 4 particle invariant mass in order to cancel resolution effects. . . . .	75
5.4	Transverse momentum of tracks in events selected by the dimuon skim. . . . .	76
5.5	$M(\mu^+\mu^-\pi^+\pi^-) - M(\mu^+\mu^-)$ with only basic quality cuts in addition to a pion $p_T$ cut. . . . .	77
5.6	$M(\mu^+\mu^-\pi^+\pi^-) - M(\mu^+\mu^-)$ with only basic quality cuts in addition to a cut on each pions $p_T$ and $\Delta R$ . . . . .	77
5.7	$M(\mu^+\mu^-\pi^+\pi^-) - M(\mu^+\mu^-)$ with all analysis cuts applied. . . . .	78
5.8	$M(\mu^+\mu^-\gamma) - M(\mu^+\mu^-)$ with all analysis cuts applied. . . . .	81
6.1	Invariant mass difference distribution in Monte Carlo for combined $X(3872)$ and $\psi(2S)$ samples. . . . .	83
6.2	Result of fitting $\chi^2$ fit with fixed $\psi(2S)$ signal Gaussian, and large errors in $X(3872)$ mass window. . . . .	86

6.3	Result of fitting with $\psi(2S)$ Gaussian released, ignoring the $X(3872)$ mass window. . . . .	86
6.4	Result of final fit with Gaussian for $X(3872)$ added. . . . .	87
6.5	$\Delta M$ distribution for the two ranges of rapidity in the $\mu^+\mu^-\pi^+\pi^-$ system.	91
6.6	$\Delta M$ distribution for the two ranges of $ \cos\theta_\mu $ in the $\mu^+\mu^-\pi^+\pi^-$ system.	91
6.7	$\Delta M$ distribution for the two ranges of $ \cos\theta_\pi $ in the $\mu^+\mu^-\pi^+\pi^-$ system.	92
6.8	$\Delta M$ distribution for the two ranges of $p_T$ in the $\mu^+\mu^-\pi^+\pi^-$ system. .	92
6.9	$\Delta M$ distribution for the two ranges of $dl_{xy}$ in the $\mu^+\mu^-\pi^+\pi^-$ system.	93
6.10	$\Delta M$ distribution for the two ranges of isolation in the $\mu^+\mu^-\pi^+\pi^-$ system.	93
6.11	Comparison of event-yield fractions for $X(3872)$ and $\psi(2S)$ in the regions: (a) $ y $ of $J/\psi\pi^+\pi^- < 1$ ; (b) $\cos\theta_\mu < 0.4$ ; (c) $\cos\theta_\pi < 0.4$ ; (d) $p_T(J/\psi\pi^+\pi^-) > 15$ GeV/ $c$ ; (e) effective transverse proper decay length, $dl_{xy} < 0.01$ cm; (e) isolation = 1 . . . . .	94
6.12	Mass regions used in the $\psi(2S)$ lifetime fit. . . . .	95
6.13	Mass regions used in the $X(3872)$ lifetime fit. . . . .	96
6.14	Lifetime distribution for the $\mu^+\mu^-\pi^+\pi^-$ system in the $X(3872)$ mass window. . . . .	96
6.15	Lifetime distribution for the $\mu^+\mu^-\pi^+\pi^-$ system in the $\psi(2S)$ mass window. . . . .	97
7.1	$\chi_{c1} \rightarrow J/\psi\gamma$ Monte Carlo after applying analysis cuts. . . . .	103

7.2	$\chi_{c2} \rightarrow J/\psi\gamma$ Monte Carlo after applying analysis cuts . . . . .	103
7.3	Monte Carlo simulation of $X(3872) \rightarrow J/\psi\gamma$ , by creating $\chi_{c1}$ particles with a mass of 3872 MeV. . . . .	104
7.4	$\chi_{c1} \rightarrow J/\psi\gamma$ fitted to a Gaussian plus an exponential tail, shown in log scale. . . . .	104
7.5	$X(3872) \rightarrow J/\psi\gamma$ fitted to a Gaussian plus symmetric exponential tails, shown in log scale. . . . .	105
7.6	$J/\psi$ sideband plus photon $\Delta M$ distribution. . . . .	107
7.7	$J/\psi$ plus “Event mixed” photon $\Delta M$ distribution. . . . .	108
7.8	$J/\psi$ plus photon from B decay Monte Carlo $\Delta M$ distribution. . . . .	108
7.9	Fit to $J/\psi\gamma$ mass distribution with fixed sideband contribution. The $\chi_c$ and $X(3872)$ components are left out of the plot. . . . .	109
7.10	Fit to $J/\psi\gamma$ mass distribution with floating sideband contribution. The $\chi_c$ and $X(3872)$ components are left out of the plot. . . . .	110
7.11	$\eta$ distribution of all $J/\psi$ candidates. . . . .	112
7.12	$\eta$ distribution of $J/\psi$ candidates in $J/\psi\gamma$ sample. . . . .	113
7.13	weight, as a function of $\eta$ applied to $J/\psi$ candidates for lifetime fitting. . . . .	113
7.14	Result of lifetime fit on $J/\psi$ sample. . . . .	114
7.15	Lifetime fitting results on the $J/\psi\gamma$ sideband. . . . .	117
7.16	Lifetime fitting results in the $\chi_c$ signal region. . . . .	118

7.17	$J/\psi\gamma$ mass distribution with the contribution from each background component overlaid as determined by simultaneous mass/lifetime fit.	118
7.18	$J/\psi\gamma$ mass distribution with background components subtracted and fit to a Gaussian with an exponential tail. . . . .	119
7.19	data in expected $X(3872)$ mass window. . . . .	122
7.20	$J/\psi$ sideband background contribution in expected $X(3872)$ mass window. . . . .	123
7.21	Uncorrelated background contribution in expected $X(3872)$ mass window. . . . .	123
7.22	$B$ meson decay background contribution in expected $X(3872)$ mass window. . . . .	124
7.23	$\chi_c$ contribution in expected $X(3872)$ mass window. . . . .	124
7.24	$X(3872)$ mass distribution expected $X(3872)$ mass window. . . . .	125
7.25	Posterior probability density. . . . .	125

# Chapter 1

## Introduction

In 2003 the Belle[1] collaboration announced the discovery of a new particle[2] known as  $X(3872)$ , so named for its mass at 3872 MeV. In this paper, the study of this particle at the DØ detector will be discussed, as well as attempts to identify the quark content and properties of this new state.

### 1.1 Overview of the Standard Model

The theoretical framework currently used to make sense of the world at length scales smaller than  $1 \times 10^{-15}$  meters is known as the Standard Model of Particle Physics, or just the Standard Model. The Standard Model describes the strong, electromagnetic, and weak forces and their interactions with the most fundamental building blocks of matter known to mankind. Gravity, the weakest of the four forces is excluded from the Standard Model due to the fact that its effect at the quantum

level is too small to be observed. To date, the Standard Model is sufficient to account for all observed phenomena in high energy physics.

The Standard Model states that there exist only two types of particles, fermions and bosons. Fermions, so named for their adherence to Fermi-Dirac statistics, carry half-integer spin and are responsible for all of the matter in the universe. Bosons, named for their adherence to Bose-Einstein statistics, carry integer spin and mediate the fundamental forces through emission and absorption by fermions.

The fermions that are described by the Standard Model are divided into two families, quarks and leptons, which are further divided into three generations, see Table 1.1. The charged leptons, known as the electron, muon, and tau, interact only through the electromagnetic and weak forces. Each of these has a corresponding neutral lepton, called a neutrino, which interacts only through the weak force. The quarks are the only known particles to carry fractional electric charge and may interact through the strong, electromagnetic, and weak forces. Quarks also possess an additional internal cyclic degree of freedom known as color. Color charge affects how quarks interact with one another through the strong force. The description of the interaction of the strong force and the quarks is known as Quantum Chromodynamics (QCD). QCD does not allow for the existence of free quarks due to the fact that gluons, the mediating bosons of the strong force, may interact with each other as well as with quarks. These interactions require that the force between two quarks increases as the distance between them increases. This means that at large

	name	symbol	charge	mass(GeV/ $c^2$ )	type
first generation	up	$u$	2/3	$4 \times 10^{-3}$	quark
	down	$d$	-1/3	$7 \times 10^{-3}$	quark
	$e$ -neutrino	$\nu_e$	0	$< 2 \times 10^{-9}$	lepton
	electron	$e$	-1	$5.1 \times 10^{-4}$	lepton
second generation	charm	$c$	2/3	1.3	quark
	strange	$s$	-1/3	.13	quark
	$\mu$ -neutrino	$\nu_\mu$	0	$< 1.9 \times 10^{-4}$	lepton
	muon	$\mu$	-1	0.106	lepton
third generation	top	$t$	2/3	178	quark
	bottom	$b$	-1/3	4.4	quark
	$\tau$ -neutrino	$\nu_\tau$	0	$< 1.8 \times 10^{-2}$	lepton
	tau	$\tau$	-1	1.78	lepton

Table 1.1: The three generations of quarks and leptons

inter-quark distances, it becomes energetically favorable for a new quark-antiquark pair to “pop” out of the vacuum rather than allow the distance between the quarks to grow. Thus, all matter observed by experiment consist of two or more quarks in a color-neutral configuration, and free quarks are not observed.

The bosons that mediate the Standard Model forces are listed in Table 1.2. The gluon and photon, the mediators of the strong and electromagnetic forces respectively, are both massless and electrically neutral. The mediators of the weak force, the  $W^\pm$  and  $Z$ , have non-zero masses with the  $W$  carrying electric charge (and thus interacting with the electromagnetic force) as well.

name	symbol	charge	mass (GeV/ $c^2$ )	associated force
photon	$\gamma$	0	0	electromagnetic
W	$W^\pm$	$\pm 1$	80	weak
Z	$Z^0$	0	91	weak
gluon	$g$	0	0	weak

Table 1.2: The force carriers of the Standard Model

In order to accommodate the masses of the  $W$  and  $Z$ , the Standard Model must contain at least one more boson, known as the Higgs boson. It is through interactions with the Higgs that the  $W$  and  $Z$  bosons acquire their masses. To date, mass limits have been set on the Higgs in collider experiments but no direct experimental evidence for its existence has been found. The observation of the Higgs and the measurement of its mass will be an important test of the Standard Model.

### 1.1.1 Mesons and Baryons

The matter observed in nature consist of two or more quarks arranged in a color neutral configuration. All naturally occurring configurations of quarks observed to date are known as mesons and baryons. Mesons consist of a quark-antiquark pair and are unstable. The most commonly observed mesons are known as pions ( $\pi$ ). Baryons consist of three quarks (or three anti-quarks). The most commonly known baryons are the proton and neutron, of which the proton is the only stable baryon.



the Standard Model does not forbid states of matter consisting of more than 3 quarks, however, to date none have been confirmed to exist.

### 1.1.2 Isospin, $C$ and $P$ Parity

When discussing the properties of mesons, baryons and other quark states, it is often useful to understand their characteristics under certain transformations. One of these transformations is known as  $C$  conjugation, which replaces all particles with their anti-particles. Another important transformation,  $P$  transformation reverses the signs of all coordinates. Many quark states are eigenstates of these transformations, meaning that the wavefunctions before,  $\phi$ , and after  $\phi'$  such a transformation will be proportional to one another, such that  $\phi' = C\phi = \lambda_C\phi$  and  $\phi' = P\phi = \lambda_P\phi$ . The numbers  $\lambda_P$  and  $\lambda_C$  are the eigenvalues of these transformations and often called  $C$  and  $P$ . These transformations have the important property that being applied twice is equivalent to not being applied at all. Thus  $C^2\phi = \phi$  and likewise for  $P$  transformation, which requires that  $\lambda_C^2 = 1$  and  $\lambda_P^2 = 1$ . In other words, this property constrains the values of  $\lambda_C$  and  $\lambda_P$  to  $\pm 1$ . One very important property of the  $C$  and  $P$  parities is that they are conserved in strong and electromagnetic interactions. Thus it is possible to determine the  $C$  and  $P$  parities of a particle through the  $C$  and  $P$  parities of its decay products if the observed decay occurred through a strong or electromagnetic process. The  $C$  and  $P$  parity of a system of fermions (i.e. a

quark-antiquark pair) with orbital angular momentum  $L$  and spin  $S$  is given by the formulae

$$P = (-1)^{L+1}, C = (-1)^{L+S}. \quad (1.1)$$

The  $C$  and  $P$  parity for a system of bosons (i.e. a system of  $\pi^+\pi^-$  mesons) with orbital momentum  $L$  is somewhat different.

$$P = C = (-1)^L. \quad (1.2)$$

Systems of particles are commonly identified through their total angular momentum  $J$ ,  $C$  parity and  $P$  parity, denoted as  $J^{PC}$ . This is called the *spin-parity* of a particle.

Another characteristic of mesons and baryons is that of isospin,  $I$ . This is a quantum number that is *nearly* conserved in strong interactions, and obeys the same algebraic rules as regular spin  $S$ . Because of this it is often convenient to characterize a state by the combination of its total isospin  $I$  and the projection of isospin on the third axis  $I_3$ , analogous with the characterization of spin states as  $|S, S_z\rangle$ . The projection  $I_3$  is conserved in both the strong and electromagnetic interactions, however the total isospin is not conserved in electromagnetic interactions. The isospin of  $u$  and  $d$  quarks is equal to  $\frac{1}{2}$ , while it is zero for all other quarks, with the  $u$  quark having positive isospin projection  $I_3 = +\frac{1}{2}$ , and the  $d$  quark having negative isospin projection  $I_3 = -\frac{1}{2}$ . Isospin can be used as an approximate symmetry due to the fact that at high energies, the mass difference between the  $u$  and  $d$  quarks can be considered negligible. At low energy and masses where the masses of the  $u$  and  $d$  quarks are approximately

equal, this symmetry is broken.

Further, there exists a relationship between the  $C$  and  $P$  parities of a system of bosons (pions) and the isospin of such a system. Consider the swapping of particles on a system of two charged pions ( $\pi^+\pi^-$ ). The total wave function for any system of bosons must be symmetric under such a transformation. The total wavefunction of this system can be factorized into a spatial, spin (irrelevant due to  $S = 0$ ) and isospin components. The spatial part of this wavefunction acquires a factor of  $(-1)^L$ . The isospin component of the wavefunction behaves just like normal spin and is symmetric if  $I$  is even and antisymmetric if  $I$  is odd, giving an additional factor of  $(-1)^I$ . Thus the total factor is  $(-1)^{L+I}$  and must equal 1. From equation 1.2 it is then apparent that

$$P = C = (-1)^I. \tag{1.3}$$

These properties will become important in Chapter 2 as possible  $J^{PC}$  assignments for the  $X(3872)$  are discussed.

## 1.2 Discovery of $X(3872)$ at Belle and Motivation for Study at DØ

The  $X(3872)$  was announced by the Belle Collaboration in August 2003. It was discovered in the exclusive decay  $B^+ \rightarrow K^+ X(3872) \rightarrow K^+ J/\psi \pi^+ \pi^-$  [2]. Belle observed a signal of  $34.4 \pm 6.5$  events and a measured mass of  $3872.0 \pm 0.6(\text{stat}) \pm 0.5(\text{syst})$  MeV/ $c^2$ . Belle also set a limit on the decay width,

$$\Gamma(X(3872)) < 2.3\text{MeV}, 90\% \text{ CL.} \quad (1.4)$$

Belle also observed that the dipion mass spectrum in  $X(3872)$  decays exhibited strong peaking near the kinematic upper limit[2], hinting that the two pions may come from a virtual  $\rho^0$  meson.

From the beginning, the discovery of the  $X(3872)$  has been puzzling. The most natural assumption is that it must be a charmonium ( $c\bar{c}$ ) state. The reason to assume this is that the  $X(3872)$  mass is too small to have any  $b$  quark content, and its decay to  $J/\psi \pi^+ \pi^-$  suggests that it contains  $c$  and  $\bar{c}$  quarks. However, the mass of the  $X(3872)$  does not seem to fit well with predicted masses in the charmonium spectrum. The potential models that calculate the charmonium masses have been very reliable, but have not yet been able to interpret the  $X(3872)$ .

Because of the problems associating the  $X(3872)$  with charmonium, many other models were proposed for the nature of the  $X(3872)$ . These included meson molecules

(a two meson system loosely bound through pion exchange), more general 4 quark interpretations, such as a diquark-antidiquark model, hybrid models, and so on.

In the following chapters, the leading interpretations of the  $X(3872)$  will be discussed as well as efforts at the DØ experiment to confirm its existence, compare its properties to those of known charmonium states, and to search for  $X(3872)$  in electromagnetic decays to  $J/\psi\gamma$ .

## Chapter 2

### Theoretical Interpretations of $X(3872)$

#### 2.1 Observed Properties of the $X(3872)$

As stated in the previous chapter, the state now known as  $X(3872)$  was first announced by the Belle Collaboration in 2003. It was found in the exclusive decay  $B^+ \rightarrow K^+ X(3872) \rightarrow K^+ J/\psi \pi^+ \pi^-$  [2]. Belle measured the mass of this new state to be:

$$M(X(3872)) = 3872.0 \pm 0.6(\text{stat.}) \pm 0.5 (\text{syst.}) \text{ MeV}/c^2 \quad (2.1)$$

, and set an upper limit on the total decay width:

$$\Gamma(X(3872)) < 2.3 \text{ MeV (90\% CL)}. \quad (2.2)$$

Belle also provides a measurement of the relative  $B^+$  branching fraction:

$$\begin{aligned} & \frac{\text{Br}(B^+ \rightarrow X(3872)K^+) \times \text{Br}(X(3872) \rightarrow J/\psi \pi^+ \pi^-)}{\text{Br}(B^+ \rightarrow \psi(2S)K^+) \times \text{Br}(\psi(2S) \rightarrow J/\psi \pi^+ \pi^-)} \\ &= 0.063 \pm 0.012(\text{stat}) \pm 0.007(\text{syst}). \end{aligned} \quad (2.3)$$

At the same time, Belle searched for the radiative decay  $X(3872) \rightarrow \gamma\chi_{c1}$ . Finding no evidence for the  $X(3872)$  in this decay channel, they set an upper limit on the ratio of partial widths

$$\frac{\Gamma(X(3872) \rightarrow \gamma\chi_{c1})}{\Gamma(X(3872) \rightarrow J/\psi\pi^+\pi^-)} < 0.89(90\%CL). \quad (2.4)$$

In the dipion invariant mass spectrum in  $X(3872) \rightarrow J/\psi\pi^+\pi^-$  decays, Belle also observed a strong peaking near the kinematic upper limit. Belle has also embarked on many searches for  $X(3872)$  in other decay channels, with most of the results coming up negative. In initial searches for additional radiative decays, Belle has found:

$$\frac{\Gamma(X(3872) \rightarrow \gamma\chi_{c2})}{\Gamma(X(3872) \rightarrow J/\psi\pi^+\pi^-)} < 1.1 \quad (90\% \text{ CL})[3] \quad (2.5)$$

$$\frac{\Gamma(X(3872) \rightarrow J/\psi\gamma)}{\Gamma(X(3872) \rightarrow J/\psi\pi^+\pi^-)} < 1.1 \quad (90\% \text{ CL})[3]. \quad (2.6)$$

In initial searches for double charm, or open charm decays involving 2  $D$  mesons, Belle has set less stringent limits[4]:

$$\text{Br}(B^+ \rightarrow K^+ X(3872)) \times \text{Br}(X(3872) \rightarrow D^+ D^-) < 4 \times 10^{-5} \quad (90\% \text{ CL}) \quad (2.7)$$

$$\text{Br}(B^+ \rightarrow K^+ X(3872)) \times \text{Br}(X(3872) \rightarrow D^0 \overline{D}^0) < 6 \times 10^{-5} \quad (90\% \text{ CL}) \quad (2.8)$$

$$\text{Br}(B^+ \rightarrow K^+ X(3872)) \times \text{Br}(X(3872) \rightarrow D^0 \overline{D}^0 \pi^0) < 6 \times 10^{-5} \quad (90\% \text{ CL}) \quad (2.9)$$

A later search by Belle with much more data revealed that the  $X(3872)$  may decay through the  $D^0 \overline{D}^0 \pi^0$  channel with quite a high rate[5], although the measured  $D^0 \overline{D}^0 \pi^0$  mass in this channel is  $2\sigma$  higher than the current world average  $X(3872)$  mass.

One search for the  $X(3872)$  performed by Belle that did yield positive results was a search for  $X(3872) \rightarrow J/\psi \pi^+ \pi^- \pi^0$ [3], prompted by predictions of a “meson molecule” model outlined later in this chapter. This decay channel was interpreted as  $J/\psi \omega$ , due to the fact that the tripion mass spectrum sharply peaks at the upper kinematic limit as one would expect for such a hypothesis. The relative width for this decay was found to be:

$$\frac{\Gamma(X(3872) \rightarrow J/\psi \omega)}{\Gamma(X(3872) \rightarrow J/\psi \pi^+ \pi^-)} = 0.8 \pm 0.3(\text{ stat}) \pm 0.1(\text{ syst}). \quad (2.10)$$

The BaBar[6] Collaboration performed a search for  $X(3872)$  decaying to  $J/\psi \eta$ [7] as well as searches for charged partners of the  $X(3872)$ [8, 9]. The upper limits obtained in these searches are:

$$\text{Br}(B^+ \rightarrow X(3872)K^+) \times \text{Br}(X(3872) \rightarrow J/\psi \eta) < 7.7 \times 10^{-6}(\text{ 90\% CL}), \quad (2.11)$$

$$\text{Br}(B^0/\overline{B}^0 \rightarrow X^\pm K^\mp) \times \text{Br}(X^\pm \rightarrow J/\psi \pi^\pm \pi^0) < 5.8 \times 10^{-6}(\text{ 90\% CL}), \quad (2.12)$$

$$\text{Br}(B^\pm \rightarrow X^\pm K_s^0) \times \text{Br}(X^\pm \rightarrow J/\psi \pi^\pm \pi^0) < 11 \times 10^{-6}(\text{ 90\% CL}). \quad (2.13)$$

The BES[10] Collaboration and the CLEO III[11] Collaboration also set strong limits on the relative width of the decay  $X(3872) \rightarrow e^+ e^-$ :

$$\Gamma(X(3872) \rightarrow e^+ e^-) \times \text{Br}(X(3872) \rightarrow J/\psi \pi^+ \pi^-) < 10 \text{ eV (90\% CL)}[12] \quad (2.14)$$

$$\Gamma(X(3872) \rightarrow e^+ e^-) \times \text{Br}(X(3872) \rightarrow J/\psi \pi^+ \pi^-) < 8.3 \text{ eV (90\% CL)}[13] \quad (2.15)$$



CLEO II also searched for production of  $C$  positive  $X(3872)$  in gamma-gamma fusion and obtained the upper limit[13]

$$(2J+1)\Gamma(X(3872) \rightarrow \gamma\gamma) \times \text{Br}(X(3872) \rightarrow J/\psi\pi^+\pi^-) < 12.9 \text{ eV (90\% CL)}, \quad (2.16)$$

where  $J$  represents the unknown spin of the  $X(3872)$ .

Belle[14] and CDF[15, 16, 17] have performed angular analyses of  $X(3872) \rightarrow J/\psi\pi^+\pi^-$  decay products, as well as analyses of the dipion mass spectrum in attempts to determine the  $J^{PC}$  quantum numbers of the  $X(3872)$ . The Belle experiment claims to rule out all  $J^{PC}$  states except  $1^{++}$  and  $2^{++}$ , while CDF claims to rule out all  $J^{PC}$  states except  $1^{++}$  and  $2^{-+}$ .

## 2.2 Charmonium Interpretation

There are many possible charmonium states that have to date, not been observed experimentally. As charmonium is the most natural interpretation for the  $X(3872)$  it is worth taking a look at the candidates, and strengths and weaknesses of all of them in describing the  $X(3872)$ . The  $c\bar{c}$  system, as a system of two fermions, is very similar to the hydrogen atom, or more accurately, positronium. As such, it can be characterized with the same quantum numbers that are used to characterize the hydrogen atom:  $n$ , the radial quantum number,  $L$ , the orbital angular momentum, total spin  $S$ , and total angular momentum  $J$ . These numbers are expressed compactly in the spectroscopic notation as  $n^{2S+1}L_J$ . In this notation  $L$  is often expressed as a

letter:  $S, P, D, F \dots$  ( $L = 0, 1, 2, 3 \dots$ ). For completeness, the  $J^{PC}$  quantum numbers are also listed with these states. The charmonium states also follow a pre-defined nomenclature. States with even  $J$  and  $PC = -+$  are called  $\eta_c(nL)$ , states with odd  $J$  and  $PC = +-$  are called  $h_c(nL)$ , states with  $PC = ++$  are called  $\chi_{cJ}(nL)$ , and states with  $PC = --$  are called  $\psi(nL)$  states. The lowest  $\psi$  state,  $\psi(1S)$  is also called the  $J/\psi$  for historical reasons, and the three lowest  $\chi$  states,  $\chi_J(1P)$  often simply called  $\chi_{c0}$ ,  $\chi_{c1}$ , and  $\chi_{c2}$ .

Most of the low lying charmonium states have been observed and their properties well established. These include the  $\eta_c(1S)$ ,  $J/\psi$ ,  $\chi_{c0}$ ,  $\chi_{c1}$ ,  $\chi_{c2}$ , and the  $\psi(2S)$ . Others have only been seen recently, such as the  $h_c(1^1P_1)$ . While the  $\eta_c(2S)$  was seen over 20 years ago by the Crystal Ball collaboration, it was only recently seen by Belle, but at a different mass.

Only a few states above the  $D\bar{D}$  threshold have been seen experimentally. Those that are allowed to decay to  $D\bar{D}$  by spin-parity conservation are expected to be very broad (and thus difficult to find) due to the rapid decays through this channel (sometimes called the open-charm channel).

Table 2.1 shows the known charmonium states as well as the as yet unobserved charmonium states which may be candidates for the  $X(3872)$ . Below, each of the possible options will be discussed in greater detail. The candidate states with positive  $C$  parity force the dipion system in the decay  $X(3872) \rightarrow J/\psi \pi^+ \pi^-$  to have negative  $C$  parity due to the negative  $C$  parity of the  $J/\psi$ . As shown in Section 1.1.2, this requires

the dipions to have isospin  $I = 1$ . This means that for all charmonium  $X(3872)$  assignments with positive  $C$  parity, the decay  $X(3872) \rightarrow J/\psi\pi^+\pi^-$  is an isospin violating decay. In general, this would seem to indicate that this decay channel is strongly suppressed. If a parallel is drawn between the  $X(3872)$  and the  $\psi(2S)$ , which has the isospin conserving decay  $\psi(2S) \rightarrow J/\psi\pi^+\pi^-$  and the isospin violating decay  $\psi(2S) \rightarrow J/\psi\pi^0$ , one sees that the isospin violating decay has a partial width 200 times smaller than the isospin conserving decay[18], and 3-60 times smaller than the 4 dominant radiative decays. Thus one may reasonably expect that a positive  $C$  parity charmonium assignment should dominantly decay through some isospin conserving process. However, large isospin violation could be explained through virtual coupling to the  $D^0D^{*0}$  system. The mass of the  $X(3872)$  is very close to the mass of the  $D^0D^{*0}$  system, which is not an isospin eigenstate. As such, virtual couplings may allow conventional charmonium to ignore isospin conservation and decay to  $C$  parity negative dipions through this channel[19, 20].

Also note that analyses by CDF[16, 17] and Belle[14] of angular distributions and the dipion mass spectrum in  $X(3872) \rightarrow J/\psi\pi^+\pi^-$  decays are all compatible with either  $S$  or  $P$  wave decays through  $J/\psi\rho^0$ . These results strongly imply that the  $X(3872)$  does indeed possess positive  $C$  parity, and that if the  $X(3872)$  is a charmonium state, its decay to  $J/\psi\pi^+\pi^-$  must be isospin violating. As such, the negative  $C$  parity states are immediately eliminated from consideration.

### 2.2.1 $1^1D_{2-+}$ State

This state cannot decay via the open-charm channel  $D\bar{D}$  due to spin-parity conservation, and as such it is expected to have a total width of about 1 MeV [24],

$n^{2S+1}L_{JPC}$	Known States	Mass MeV/ $c^2$	Width MeV
$1^1S_{0-+}$	$\eta_c(1S)$	2980[18]	17[18]
$1^3S_{1--}$	$J/\psi$	3097[18]	0.1[18]
$1^1P_{1+-}$	$h_c(1P)$	3526[18]	
$1^3P_{0++}$	$\chi_c(1P)$	3415[18]	10[18]
$1^3P_{1++}$	$\chi_c(1P)$	3511[18]	1[18]
$1^3P_{2++}$	$\chi_c(1P)$	3556[18]	2[18]
$1^1D_{2-+}$		3838[21]	
$1^3D_{1--}$	$\psi(3770)$	3770[18]	25[18]
$1^3D_{2--}$		3830[21]	
$1^3D_{3--}$		3868[21]	
$2^1S_{0-+}$	$\eta_c(2S)$	3654[18]	17[22, 23]
$2^3S_{1--}$	$\psi(2S)$	3686[18]	0.3[18]
$2^1P_{1+-}$		3968[21]	
$2^3P_{0++}$		3932[21]	
$2^3P_{1++}$		4008[21]	
$2^3P_{2++}$		3966[21]	
$3^1S_{0-+}$			
$3^3S_{1--}$	$\psi(4040)$	4040[18]	52[18]

Table 2.1: Summary of charmonium spectrum. States that have yet to be observed by experiment are given masses at their expected values. States at  $2D$ ,  $3P$ ,  $3D$  and higher are not listed as they are expected to be too heavy to even consider as candidates for the  $X(3872)$ , as are states with  $L > 2$ .

which makes it a plausible candidate for the  $X(3872)$ . However, the fact that the isospin conserving decay to  $\eta_c\pi^+\pi^-$  has not yet been observed makes this description unlikely. CDF [17, 16] found that the dipion mass distribution in  $X(3872)$  decays supports the hypotheses of  $J^{PC} = 2^{-+}$  and  $J^{PC} = 1^{++}$ , however Belle has claimed [14] that this state is ruled out by the dipion mass distribution. Belle has also recently observed  $X(3872)$  decaying to  $D^0\overline{D}^0\pi^0$ [5] at a rate much higher than that  $J/\psi\pi^+\pi^-$ , which seems to disfavor this state.

### 2.2.2 $2^3P_{0++}$ State

Open charm channel decay for this state is allowed. Due to this fact, the predicted total width is an order of magnitude higher than the 2.3 MeV upper limit set by Belle, which makes this state a very unlikely candidate. This state also suffers from the non-observation of the  $X(3872)$  in  $\gamma\gamma$  fusion at CLEO-III[13]. The limit set by CLEO in this mode is four times greater than the partial width of  $\chi_{c0}$ , this state's lighter companion, to  $\gamma\gamma$ . If the partial widths of these two states to  $\gamma\gamma$  are comparable, then this state can be safely dismissed.

### 2.2.3 $2^3P_{1++}$ State

Although this state's predicted mass and width are much higher than 3872 MeV/ $c^2$ [25, 24, 26, 27], if this state's mass is set to 3872 MeV/ $c^2$ , it's width could

shrink to the order of 1-2 MeV[24]. This state is also predicted to have dominant decays to  $J/\psi\gamma$  and  $\psi(2S)\gamma$ [24], however predicting the branching fraction for these modes is very difficult and highly dependent upon model details. The dipion mass spectrum analyses and angular analyses carried out by CDF and Belle both support the  $J^{PC} = 1^{++}$  assignment[14, 16, 17]. This state is also supported by the evidence for decays to  $J/\psi\omega$ [3].

#### **2.2.4 $2^3P_{2++}$ State**

This state is very similar to the  $2^3P_{0++}$  state. Its width is expected to be an order of magnitude larger than 2.3 MeV [24], and the non-observation in  $\gamma\gamma$  fusion[13] would seem to rule this out.

#### **2.2.5 $3^1S_{0-+}$ State**

As part of the  $3S_J$  doublet, this state is highly unlikely. Its mass is believed to be set by the observation of  $\psi(4040)$ , the  $3^3S_{1--}$  state. From the 1S and 2S states, it is known that the mass splittings between the  $^1S_{0-+}$  states and  $^1S_{0-+}$  states are about 120 MeV/ $c^2$  and 50 MeV/ $c^2$  respectively. This pattern of decreasing mass splittings is expected to continue on up the potential well, as is also observed in the  $\Upsilon$  meson family. This fact makes this state a very unlikely interpretation for the  $X(3872)$ .

### 2.2.6 Summary of Charmonium States

Taking all of the experimental data gathered to date, and the expectations from the charmonium models, there are only two charmonium states that deserve strong consideration as candidates for the  $X(3872)$ :  $2^3P_{1++}$  and  $1^1D_{2-+}$ . Of these two, the more likely interpretation is the  $2^3P_{1++}$  charmonium state. In Chapter 7, this model will be tested by searching for decays to  $J/\psi\gamma$  at DØ.

## 2.3 Meson-Molecule Interpretation

Due to the problems associating  $X(3872)$  with a charmonium state, the interpretation that the  $X(3872)$  may be a weakly bound  $D - D^*$  “meson-molecule” has gained popularity since the discovery of  $X(3872)$ . This is due primarily to the close proximity of the  $X(3872)$  mass, for which the world average is currently [2, 28, 29, 30]:

$$m(X(3872)) = 3871.2 \pm 0.5 \text{ MeV}/c^2. \quad (2.17)$$

Compare this with the PDG world average value for the  $D - D^*$  mass threshold (recently CLEO-III has provided a precision measurement of this threshold which is quoted below the world average):

$$m(D^0 D^{*0}) = 3870.32 \pm 2.0 \text{ MeV}/c^2 [18] \quad (2.18)$$

$$m(D^0 D^{*0}) = 3871.81 \pm 0.36 \text{ MeV}/c^2 [31] \quad (2.19)$$

The proximity of the  $X(3872)$  mass to this threshold has made the possibility that the  $X(3872)$  is some kind of  $D^0 - \overline{D}^{*0}$  compound, bound through pion exchange, very attractive. Indeed, the existence of such a molecular state at precisely this mass was predicted as far back as the early nineties[32, 33].

The concept of meson molecules dates back to the late sixties, and has since been used as an attempt to explain many phenomena before eventually losing out to conventional meson states[34, 35, 36, 37, 38, 39, 40, 41, 42, 43, 44, 45].

The molecular model has several aspects that make it appealing as an interpretation for the  $X(3872)$ . Perhaps the most notable is that the  $DD^*$  system is not an isospin eigenstate, and thus isospin is not expected to be conserved. In pure molecular models, the decay to  $D^0 \overline{D}^0 \pi^0$  is expected to be the primary decay mode[33], which does agree with the Belle Collaborations recent observation of this decay mode. However, in a similar model which assumes that the  $X(3872)$  is not a simple  $D^0 \overline{D}^{*0}$  molecule, but rather a  $J^{PC} = 1^{++}$  state composed primarily of  $D^0 \overline{D}^{*0}$  with a mix of  $D^+ \overline{D}^{*-}$ ,  $J/\psi \omega$ , and  $J/\psi \rho$ [46]. This model predicted  $X(3872)$  decaying into both  $J/\psi \rho$  and  $J/\psi \omega$ . Following this prediction, Belle searched for  $X(3872)$  decaying to  $J/\psi \omega$ , and found evidence for this decay channel with a rate comparable to the decay rate to  $J/\psi \pi^+ \pi^-$ . This model also predicts that the decay rate to  $J/\psi \gamma$  should be small, as should the decay to  $D^0 \overline{D}^0 \pi^0$ . Belle however has shown quite strong evidence that  $D^0 \overline{D}^0 \pi^0$  may be a dominant decay mode of the  $X(3872)$ .



## 2.4 Diquark-Antidiquark Interpretation

This model for interpretation is a more general four quark model in which all four quarks interact with each other equally rather than in a bound state of bound states. In this model, a so-called diquark  $[cq]$  and antidiquark  $[\bar{c}q']$  ( $q, q' = u$  or  $d$ ) act as composite antiquarks and quarks. This leads to a number of  $X$  states in addition to the observed state at  $3872 \text{ MeV}/c^2$ [47]. In particular, two  $0^{++}$  states, two  $1^{-+}$  states, one  $1^{++}$  state, and one  $2^{++}$  state. The  $1^{++}$  is proposed for the  $X(3872)$  because it does match many of the observed properties, such as the narrow width, and the allowed decays to both  $J/\psi\rho$  and  $J/\psi\omega$ . This model also predicts that each of these states should exhibit a small mass splitting due to the mixing of  $u$  and  $d$  choices for  $q$  and  $q'$ . The predicted maximal mass splitting is on the order of  $7 \text{ MeV}/c^2$ , and to date no such mass splitting has been observed. This model also requires the existence of charged partners to the  $X$  as well. To date, no such charged partners have been observed, although the limits on charged  $X(3872)$  partner production set by BaBar[8, 9] are not in contradiction with this model yet.

## 2.5 Summary

As outlined above, the theoretical interpretation for the  $X(3872)$  is currently unresolved. In addition to the leading models mentioned above, other models have been proposed such as hybrid charmonium[48], a glueball-charmonium mixture[49]

and a dynamic cusp[50]. These models however are not in very good agreement with recent data however. Of the models mentioned, likely interpretations include conventional charmonium, with  $^1D_{2-+}, ^3P_{1++}$  being the most likely assignments, a  $D\overline{D}^*$  molecule, or a diquark-antidiquark state. Note that these hypotheses do not necessarily exclude one another, as it is possible for the  $X(3872)$  to be some mixture of any of them[25, 51]. With such a wide range of options, it is possible that the  $X(3872)$  may remain a mystery for some time. In the following chapters, the confirmation of the existence of the  $X(3872)$  decaying to  $J/\psi\pi^+\pi^-$  at DØ will be discussed in Chapter 6. These results were published in [29] on a smaller dataset than the results presented here. Chapter 7 will detail search for  $X(3872)$  decaying to  $J/\psi\gamma$ , a characteristic decay of the  $2^3P_1$  charmonium state, which is naively expected to be a dominant decay channel with respect to  $J/\psi\pi^+\pi^-$ .

## **Chapter 3**

### **Experimental Apparatus**

#### **3.1 Introduction**

The Fermilab Tevatron is currently the world's highest energy accelerator, producing collisions of protons and anti-protons at a center of mass energy of 1.96 TeV. This chapter will describe the Tevatron in detail as well as the DØ detector elements most important to the analysis performed.

#### **3.2 The Tevatron Accelerator**

The Tevatron accelerator is the last in a series of seven accelerators which is used to bring beams of protons and anti-protons up to energies of 0.98 TeV. At this energy, the beams of protons and anti-protons are steered to collide at two interaction regions. These interaction regions are named B0 and D0 for their location along the

Tevatron ring, as shown in Figure 3.1, which are surrounded by the general purpose detectors CDF and DØ. The analyses presented in this paper were performed using data from the DØ detector. Below is a brief overview of the complex that provides the DØ experiment with the  $p\bar{p}$  collision data. The interested reader is referred to [52] and [53] for more detail.

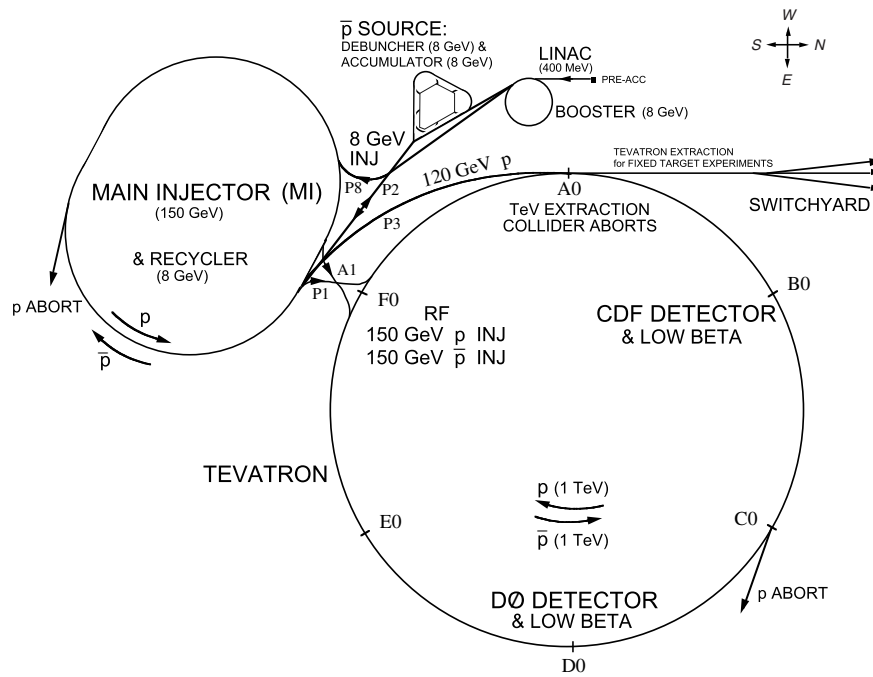


Figure 3.1: Diagram of the Fermilab Tevatron Complex. This figure is a standard Fermilab figure.

The Pre-Accelerator (Preacc) produces and accelerates negatively charged hydrogen ( $H^-$ ) atoms, and accelerates them to an energy of 750 KeV by means of a Cockcroft-Walton accelerator. After leaving the Preacc, the beam of  $H^-$  atoms are bunched and fed into the Linac, which accelerates the ions by means of RF cavities

to an energy of 400 MeV. From the Linac, the 400 MeV  $H^-$  atoms are transferred to the first synchrotron accelerator in the chain, known as the Booster. The Booster contains a series of magnets around 18 RF cavities arranged in a circle of 75 meters. The Booster strips the  $H^-$  atoms of their electrons, leaving only bare protons, and then accelerates these protons to an energy of 8 GeV.

From the Booster, 8 GeV beams of protons are sent to the Main Injector where they are either accelerated to 120 GeV and transferred to the anti-proton ( $\bar{p}$ ) source, or accelerated to 150 GeV and inserted into the Tevatron. At the  $\bar{p}$  source, protons collide with a nickel target and produce many secondary particles. Approximately one out of every  $10^5$  of these collisions will produce an anti-proton. The anti-protons are captured by the debuncher and temporarily stored in the accumulator at 8 GeV until enough ( $\simeq 10^{11}$ ) anti-protons have been produced for a Tevatron store. The Debuncher uses RF 'bunch rotation' and adiabatic debunching to reduce the momentum spread of the anti-protons from the anti-proton source for transfer to the Accumulator. In the Accumulator, stochastic cooling is used to reduce the beams emittance. This is accomplished by sampling the anti-protons motion in the beam with a pickup, and then correcting that motion downstream with a kicker. From the Accumulator, anti-protons are transferred into the main injector and accelerated to 150 GeV for transfer to the Tevatron. The Main Injector then transfers 150 GeV protons and anti-protons into the Tevatron where they are then accelerated to an energy of 0.98 TeV.

The protons and anti-protons circle the Tevatron in 36 groups or bunches. At the interaction regions, proton bunches are steered to intersect with anti-proton bunches. These bunch crossings occur once every 396 nanoseconds. A measure for the number of hard scatters or collisions that are taking place is the instantaneous luminosity. Instantaneous luminosity is typically expressed in units of  $\text{cm}^{-2}\text{s}^{-1}$ , or collisions per unit cross section per second. Each experiment has a dedicated detector subsystem for measuring the instantaneous luminosity. The integrated luminosity is a measure of how many collisions have taken place over a given time. Integrated luminosity is given in units of inverse barns ( $\text{b}^{-1}$ ), where one barn is equal to  $100\text{fm}^2$ , or, in the case of the Tevatron, inverse picobarns ( $\text{pb}^{-1}$ ) or inverse femtobarns ( $\text{fb}^{-1}$ ).

A typical 'store' of protons and anti-protons will collide in the Tevatron for approximately one day. When the instantaneous luminosity drops too low, the particles are removed from the Tevatron and a new set of protons and anti-protons are injected into the machine. Since the process of building up the necessary numbers of anti-protons can be time consuming, this process occurs while the previous store is colliding to limit downtime for the experiments.

### 3.3 Interactions of Particles with matter

The DØ detector examines the remnants of  $p\bar{p}$  collisions through a series of instruments that record a particles position and energy as a result of a particles interaction

with matter in the detector. In order to understand the signals in the detector, it is thus necessary to understand how particles interact with matter. Tracking detectors are designed to record the position of a charged particle with minimal energy loss, while calorimeters are designed to fully absorb the energy of most particles and its resulting shower and to measure the energy and position of the particle in the process. The interactions which make these measurements possible are described below.

### 3.3.1 Electrons and Photons

Electrons passing through matter lose energy primarily through bremsstrahlung radiation and ionization. Above a critical energy,  $E_c$  [18]:

$$E_c = \frac{800}{Z + 1.2} \text{ MeV} \quad (3.1)$$

where  $Z$  is the atomic number of the medium. At DØ, bremsstrahlung radiation is the dominant process for energy loss for electrons and photons. High energy photons interacting with matter produce electron-positron pairs. Thus, both electrons and photons produce showers of electrons and photons until the energy of the electrons falls below the critical energy. Below the critical energy the electrons interact primarily through ionization. The mean distance over which an electron loses all but  $1/e$  of its energy is known as the radiation length,  $X_0$ [18]

$$X_0 = \frac{716.4A}{Z(Z + 1) \ln(287/\sqrt{Z})} \text{ g cm}^{-2} \quad (3.2)$$

where  $A$  is the atomic mass of the medium. The radiation length  $X_0$  is also  $\frac{7}{9}$  of the mean free path of pair production for high energy photons through a medium.

The longitudinal shower behavior of electromagnetic cascades can be reasonably described by a gamma distribution[18]:

$$\frac{dE}{dt} = E_0 b \frac{(bt)^{a-1} e^{-bt}}{\Gamma(a)} \quad (3.3)$$

where  $a$  and  $b$  are constants and  $t = x/X_0$ , where  $x$  represents longitudinal distance within the shower. The maximum,  $t_{max}$  then occurs at  $(a - 1)/b$ . The Particle Data Group[18] have made fits to shower profiles in elements ranging from carbon to uranium at energies ranging from 1 GeV to 100 GeV and found that the energy deposition profiles are well described by equation (3.3), with[18]:

$$t_{max} = (a - 1)/b = 1.0 \times (\ln y + C_j), j = e, \gamma \quad (3.4)$$

where  $y = E/E_c$ , with  $E$  representing energy, and  $C_e = -0.5$  for electron showers and  $C_\gamma = +0.5$  for photon showers.

### 3.3.2 Muons

Muon interaction through bremsstrahlung radiation occurs at a much lower rate than that of electrons due to the much larger mass of the muon. The critical energy of muons is on the order of 1 TeV[18]. Muons produced at the Tevatron have energies on the order of 1 GeV and thus muon energy loss in the DØ detector occurs primarily through ionization. These muons are minimum ionizing particles, or MIPs, and



typically deposit only minimal energy in all of the detector subsystems.

### 3.3.3 Hadrons

Hadronic particles interact inelastically with the nuclei of the medium, producing pions and nucleons. At high energies these resulting particles also interact with nearby nuclei producing showers of hadronic particles. The characteristic length scale for hadronic showers is the nuclear interaction length,  $\lambda_I$ , which is roughly independent of energy[18].

$$\lambda_I \approx 35 A^{1/3} \text{ g cm}^{-2} \quad (3.5)$$

### 3.3.4 Neutrinos

Neutrinos interact with matter only through weak interactions. Direct detection of neutrinos at DØ is impossible, however the presence of high energy neutrinos can be inferred from transverse momentum conservation constraints.

## 3.4 The DØ Detector

The Run II DØ detector is a multi-purpose detector designed to measure the kinematics of the remnants of  $p\bar{p}$  collisions. The detector consists of 3 major subsystems. In the core of the detector is the tracking system. The tracking system is surrounded by a solenoid which produces a 2 Tesla magnetic field oriented along the

beam axis. The tracking system allows for precision measurements of the position of charged particles as they travel outward from the interaction point. The magnetic field in the tracking volume allows the tracking system to also measure the transverse momentum of charged particles by measuring their radius of curvature. Just outside of the tracking volume and solenoid are the DØ calorimeters, a system of finely grained Uranium and Liquid Argon calorimeters which record the energies and positions of hadronic and electromagnetic showers. Finally, a large 3 layer muon spectrometer detects the presence and measures the momentum of muons which escape the calorimeter. The interested reader is encouraged to see [54] and [55] for more detail.

### 3.4.1 Coordinate System

The DØ coordinate system is a right handed system that places the beam-line on the  $z$  axis, with protons flowing in the positive  $z$  direction and anti-protons in the negative  $z$  direction. The  $y$  axis is then vertical, with the positive direction pointing upward, and the positive  $x$  axis points away from the center of the Tevatron ring. Because the DØ detector has cylindrical symmetry about the  $z$  axis, it is often useful to use standard cylindrical coordinates about the  $z$  axis  $(r, \phi)$ , which is transformed from the standard Cartesian  $(x, y, z)$  coordinate system through:

$$r = \sqrt{x^2 + y^2} \tag{3.6}$$

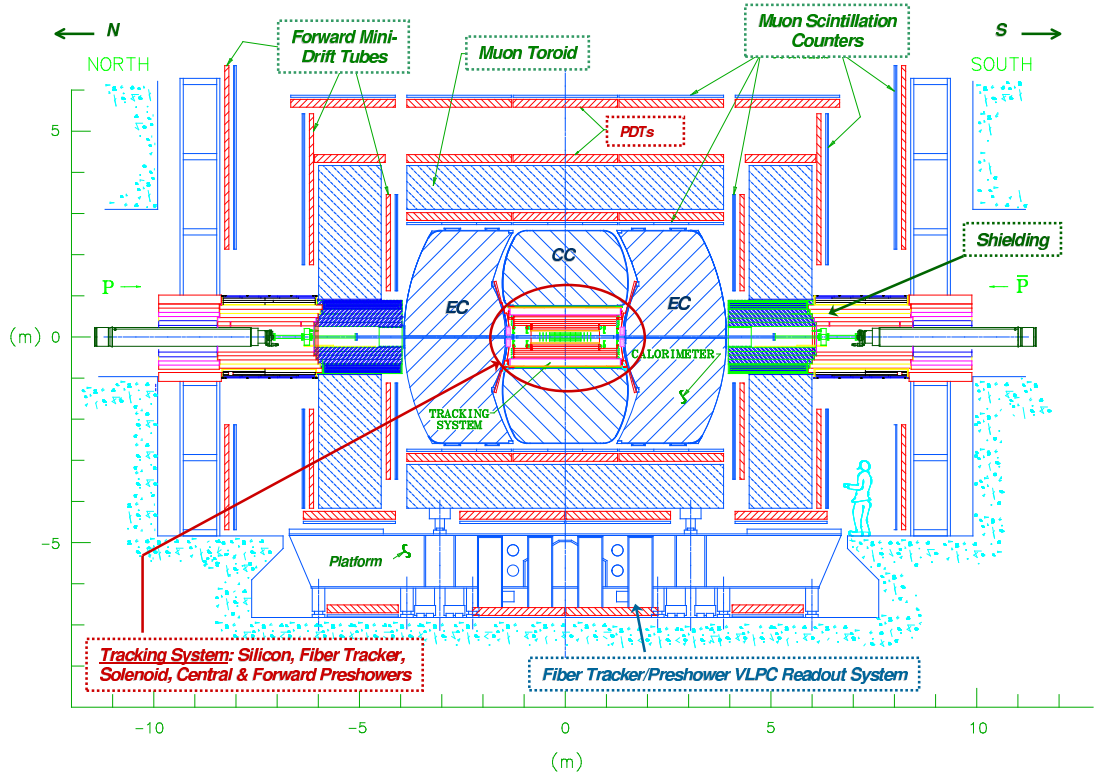


Figure 3.2: DØ Detector cutaway view. This is a standard DØ figure

$$\phi = \tan^{-1}\left(\frac{y}{x}\right) \quad (3.7)$$

Additionally, it is often convenient to utilize a new coordinate, pseudo-rapidity,

$\eta$ :

$$\eta = -\ln \tan \frac{\Theta}{2} \quad (3.8)$$

where  $\Theta$  is the polar angle defined by,

$$\Theta = \cos^{-1} \frac{z}{\sqrt{x^2 + y^2 + z^2}}. \quad (3.9)$$

Pseudo-rapidity is a convenient choice at DØ and other detectors because of the fact that it approaches the rapidity,  $y = \frac{1}{2} \ln\left(\frac{E+p_z}{E-p_z}\right)$  in the zero mass limit. The

rapidity,  $y$  is Lorentz-invariant under boosts along the  $z$  axis, and additionally, the multiplicity of high energy particles is approximately constant in  $\eta$ .

The choice of the origin is the last piece to completely define the coordinate system at DØ. There are two common choices that are often used, physics coordinates, where the origin is located at the reconstructed vertex of the interaction, and detector coordinates, where the origin is chosen to be at the center of the DØ detector. All coordinates used here will be physics coordinates unless otherwise noted.

### **3.4.2 The Central Tracking System**

The central tracking system is designed to measure the momentum, direction, and sign of the electric charge for charged particles produced in an event. The system has a mean radius of 60 cm and resides inside a 2 Tesla solenoid. The central tracking system consists of two tracking detectors, a silicon micro-strip detector (SMT) positioned just around the beam pipe and a central fiber tracker (CFT) positioned just around the SMT, see Figure 3.3

#### **The SMT**

The SMT was designed to give an accurate measurement of track impact parameters, or the distance of closest approach (DCA) of a track to the primary interaction point (primary vertex). The SMT also allows for the identification of primary and secondary vertices, and optimizes tracking efficiency over a large range of  $\eta$  and a

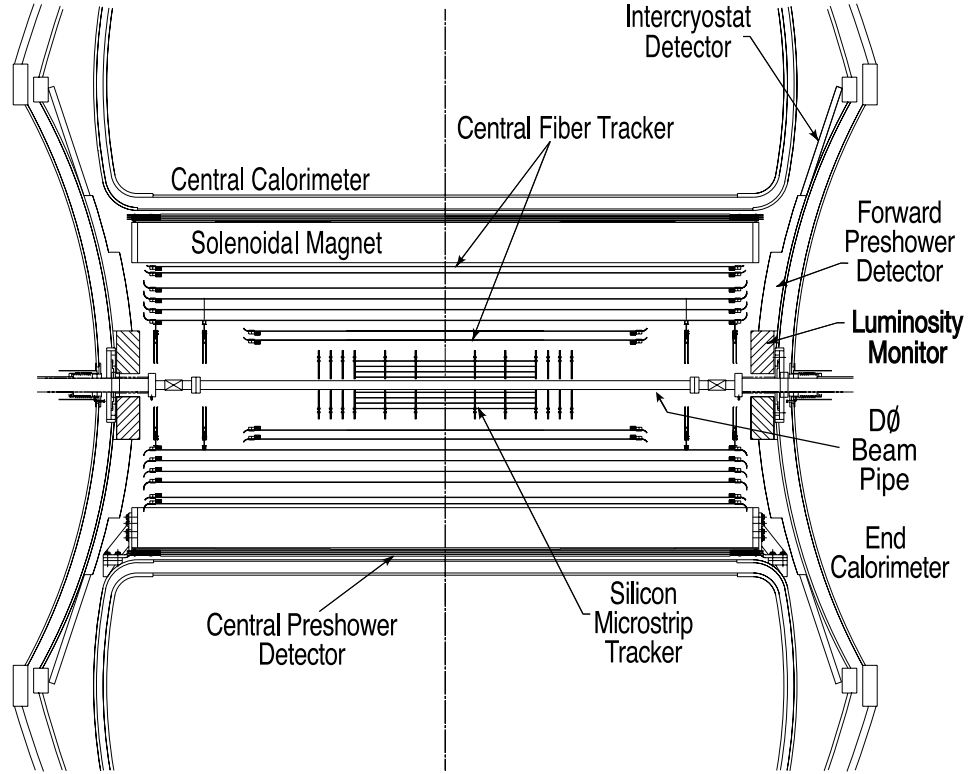


Figure 3.3: Closeup schematic of the DØ detector subsystems[54].

large spread in vertex  $z$  position. The silicon modules that make up the SMT are thin  $n$ -type silicon wafers with  $p$ -type strips etched onto the surface. The silicon modules are reverse-biased when in operation which creates a depletion region within the silicon wafer. A charged particle passing through the depletion region of a silicon module will deposit a small amount of energy through ionization. This leads to the production of electron/hole pairs. Due to the bias voltage, the ionized charge is accelerated toward the conductive strips, where the charge is collected and read by readout chips at the end of the strips.

The SMT consists of six barrels of eight layers each, organized as four super-layers, with an inner radius of 2.5 cm and an outer radius of 10 cm. Interspersed between the barrels and appended to the ends of the structure are 12 'F-disks' as well as 4 larger 'H-disks'. These disks allow for greater tracking efficiency at high values of  $\eta$  and measurement of a particles momentum in the  $z$  direction. This configuration is illustrated in Figure 3.4

The silicon modules are known as 'ladders' in the barrels and 'wedges' in the disks. They are  $300\mu\text{m}$  thick, with strips of  $50\mu\text{m}$  pitch. All of the ladders, except for those in layers 1 and 3 of the outermost barrels, are double-sided, capable of both axial (parallel to the beam axis) and stereo (at some angle relative to the beam axis) readout. In super-layers 1 and 3 the stereo angle is  $90^\circ$  with a strip pitch of  $153.5\mu\text{m}$ . These modules with  $90^\circ$  stereo angle are known as double sided, double metal (DSDM) modules. In super-layers 2-4 the stereo angle is  $2^\circ$  with  $62.5\mu\text{m}$  strip pitch. Super-layers 1 and 2 of the barrels have 12 ladders each while super-layers 3 and 4 have 24 ladders. The F disks each contain 12 double sided (DS) wedges with  $30^\circ$  stereo angle. The H disks contain 24 wedges made of two single sided (SS) silicon wafers glued back to back which give an effective stereo angle of  $15^\circ$ . The properties of the various sensor types in the SMT are shown in Table 3.1[54].

This configuration of the SMT subsystem, when combined with the central fiber tracker, provides a resolution on the primary vertex of approximately 10 microns over the range where the primary vertex  $z$  position is within  $\pm 40$  cm of the center of the

Module	Type	Layer	Pitch ( $\mu\text{m}$ ) p/n	Stereo angle	Length (cm)	Inner/Outer radius(cm)
F-Disks	DS	-	50/62.5	30°	7.93	2.57/9.96
H-Disks	SS	-	40 80 <sup>readout</sup>	15° (effective)	7.63 <sup>i</sup> 6.33 <sup>o</sup>	9.5/26
Central barrels(4)	DSDM	1,3	50/153.5	90°	12.0	2.715/7.582
	DS	2,4	50/62.5	2°	6.0	4.55/10.51
Outer barrels(2)	SS	1,3	50	-	6.0	2.715/10.51
	DS	2,4	50/62.5	2°	6.0	4.55/10.51

Table 3.1: Specifications of the various sensors in the DØ silicon detector. *i* indicates the inner H-disk sensor while *o* indicates the outer H-disk sensor.

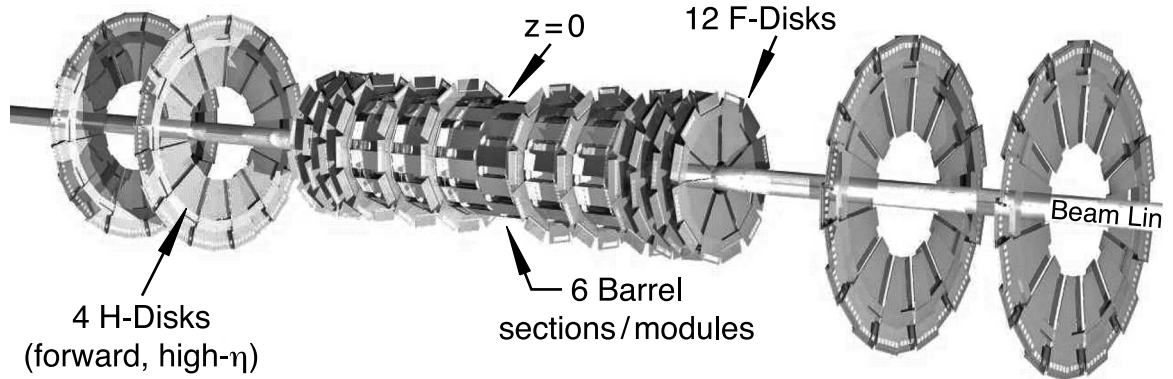


Figure 3.4: Three dimensional view of the DØ Silicon Micro-strip Detector assembly. This is a standard DØ figure.

detector[56], and a track impact parameter resolution of approximately 20 microns as shown in Figure 3.5.

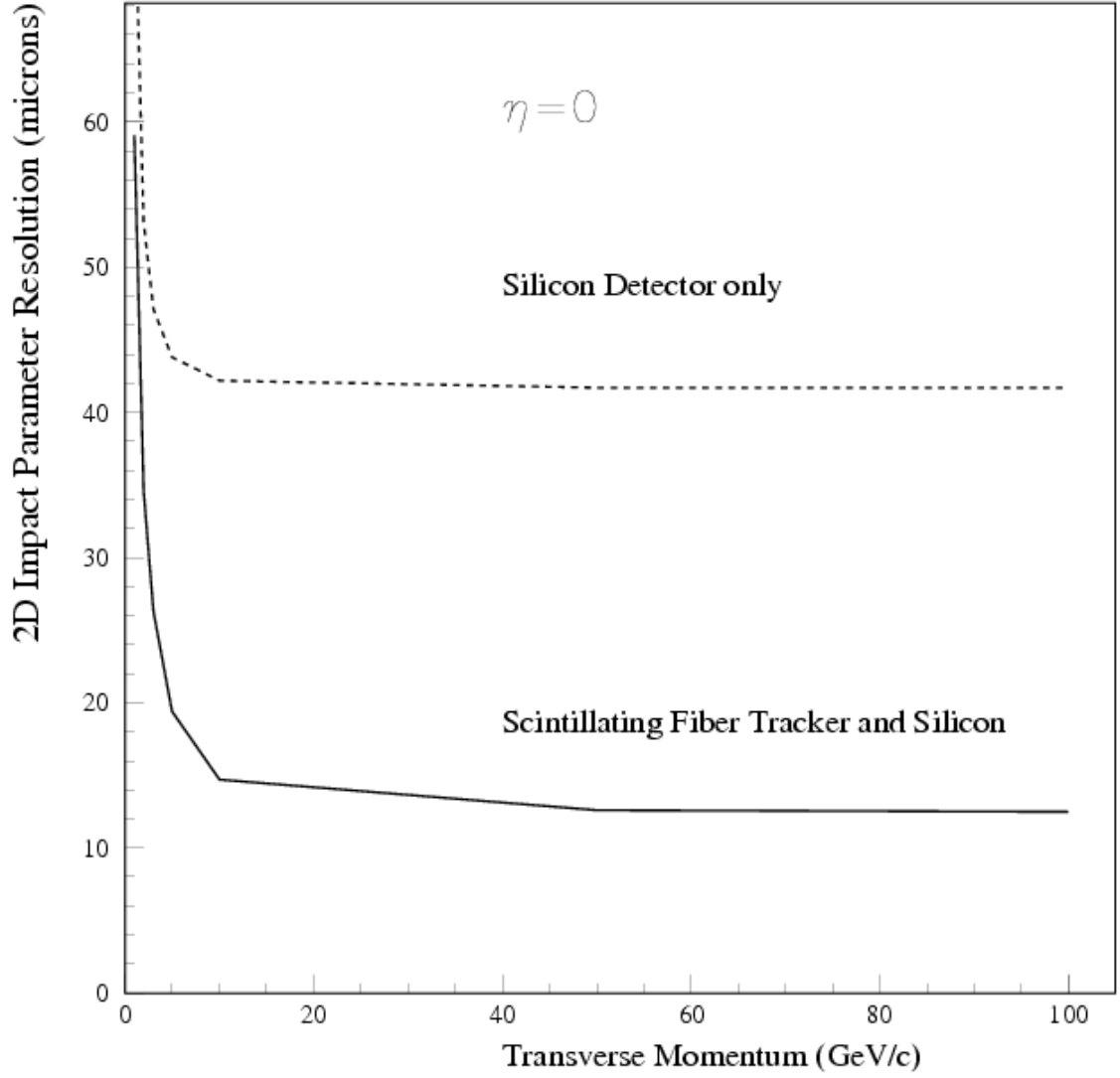


Figure 3.5: Track impact parameter resolution as a function of track transverse momentum for SMT only configuration and SMT+CFT configuration.[56]

### The Central Fiber Tracker

The central fiber tracker (CFT) is a larger tracking detector just outside the SMT. Its purpose is to complete tracking coverage throughout the tracking volume,



as well as to provide transverse momentum ( $p_T$ ) and total momentum measurements of charged particles as they make their way to the calorimeter. The CFT is composed of approximately 200km of scintillating fiber. When a charged particle passes through one of the scintillating fibers, it will deposit a small amount of energy through ionization. As the fibers are non-conductive, this leaves behind a wake of excited molecules. The core substance of the fibers, polystyrene, rapidly transfers this energy to a 1% concentration paraterphenyl dye, then releases a small fraction of this energy ( $\approx 3\%$ ) in the form of optical photons of 340nm wavelength over just a few nanoseconds through a rapid fluorescence decay. In the fiber, these photons are absorbed by a wave-shifting dye, 3-hydroxyflavone, and re-emitted at 530nm. These photons then traverse the fibers through total internal reflection until they arrive at longer clear fiber waveguides that transmit them to visible light photon counters (VLPCs) to read out the signal. Because the fibers are read out from only one end, the end of the fiber opposite the readout is mirrored to reflect the light back to the readout.

The fibers that make up the CFT have a diameter of  $835\mu\text{m}$  and are mounted in 32 concentric layers over 8 barrels. Each barrel consists of two double layers of fibers, one axial double layer and one double layer of either  $u(+3^\circ)$  or  $v(-3^\circ)$  stereo fibers. To provide maximal coverage, the fibers of a doublet layer are offset by half a fiber width, as shown in Figure 3.6. The 8 cylinders alternate between  $zu$  doublet layers and  $zv$  doublet layers. In total the CFT contains 76,800 fibers over its 32 layers. The design of the CFT gives an inherent doublet position resolution of approximately 100

$\mu\text{m}$  provided that the position of each individual fiber is known to within  $50\ \mu\text{m}$ .

The VLPCs are solid state photo-multipliers that operate at a temperature of 9K and detect photons with a quantum efficiency of approximately 85%. They produce between 30,000 and 60,000 electrons per photon which makes them ideally suited for CFT readout.

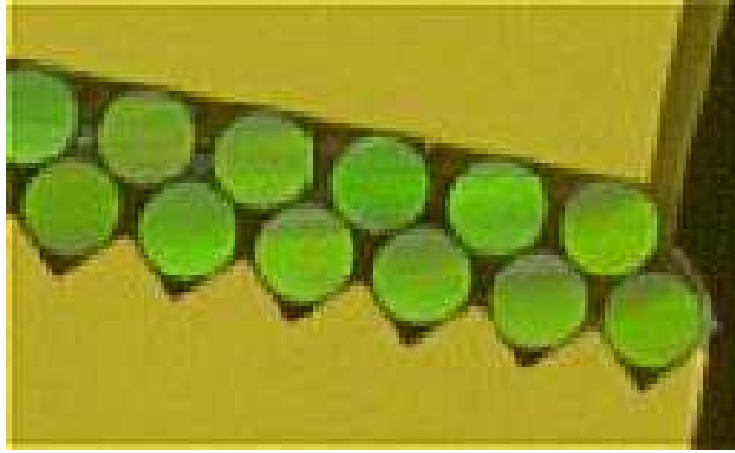


Figure 3.6: One 'ribbon' assembly of the CFT showing the staggered configuration of two layers of fibers. This figure is a standard DØ figure.

This CFT configuration provides good transverse momentum resolution,  $\frac{\sigma_{p_T}}{p_T} \approx 0.02$ , as shown in Figure 3.7.

### 3.4.3 Solenoid

The transverse momenta of charged particles are determined from their curvature in the 2 Tesla magnetic field produced by the DØ solenoid magnet. The solenoid is a 2.7 meter long superconducting magnet with a two layer coil and mean radius of 60

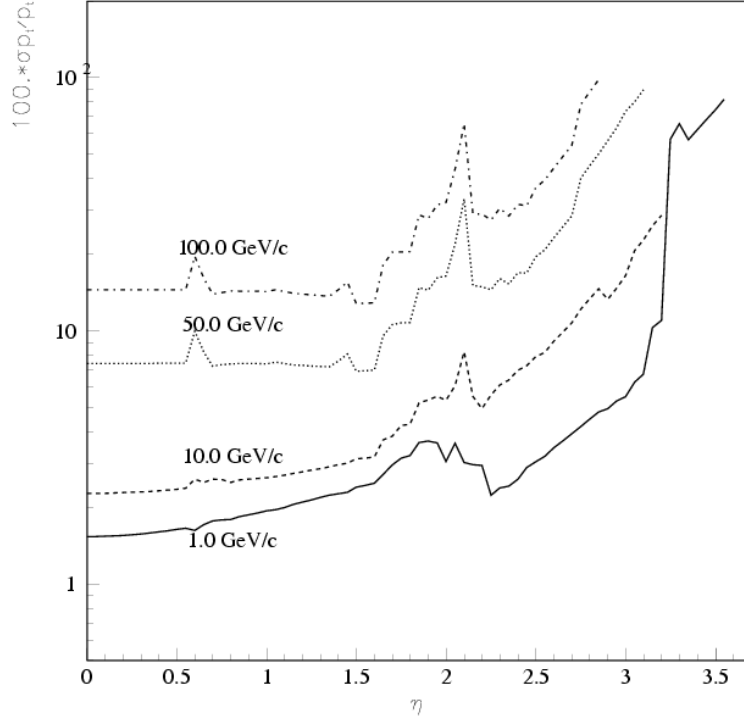


Figure 3.7: Fractional  $p_T$  resolution as a function of  $\eta$ [54].

cm. It has a stored energy of 5 MJ and operates at 10K. The magnetic field inside the tracking volume is kept uniform by the use of two grades of conductor in order to minimize the radiation length of the solenoid. The uniformity of the field inside the tracking volume is within 0.5%, and the solenoid has a thickness of approximately 0.9 radiation lengths.

### 3.4.4 Pre-shower Detector

The pre-shower detectors are situated just outside of the solenoid and just before the calorimeter and are used to aid in electron identification and background rejection.

Both the forward and central pre-shower detectors are constructed with interleaved triangular strips of scintillator shown in Figure 3.8. The triangular design was chosen to eliminate dead space between strips and to improve the position measurements since most tracks will traverse more than one strip. Embedded in the center of the pre-shower strips are wavelength shifting fibers that collect and carry the light to the end of the detector where they are read out by VLPCs in the same manner as for the CFT.

The central pre-shower detector consists of 3 concentric cylindrical layers of scintillating fibers arranged in an axial- $u$ - $v$  configuration, with a  $u$  stereo angle of  $23.774^\circ$  and a  $v$  stereo angle of  $24.016^\circ$ . Between the solenoid and the CPS is a lead radiator that is approximately 1 radiation length in thickness covering  $|\eta_{det}| < 1.3$

The forward pre-shower detectors are located just inside the calorimeter end-caps, and cover the region of  $1.5 < |\eta_{det}| < 2.5$ . Within the region  $1.5 < |\eta_{det}| < 1.65$  electrons and photons are expected to shower as they pass through the solenoid. In this region there are two layers of scintillating pre-shower fibers. In the region  $|\eta_{det}| > 1.65$  there is no appreciable material to induce showering, so a two radiation length lead absorber is placed in front of the double layer of scintillating fiber. Directly in front of the lead absorber are two additional layers of scintillating pre-shower fibers which are known as the MIP layers. This configuration is constructed with wedges that are illustrated in Figure 3.9. Because there is no appreciable material prior to the MIP layers, they can be used as tracking detectors as well.

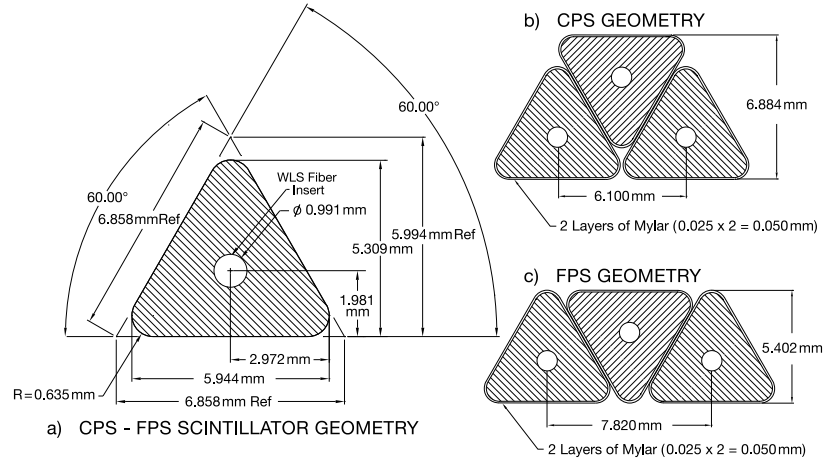


Figure 3.8: Geometry of scintillating fibers in the pre-shower detectors.[54]

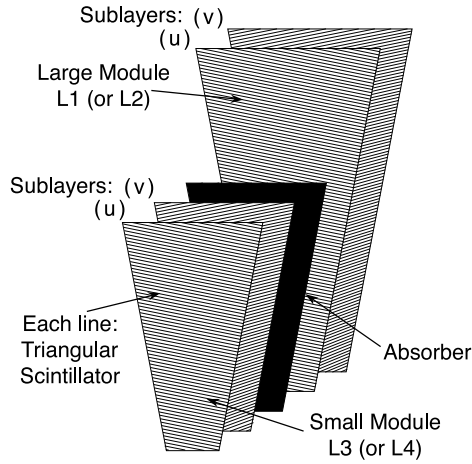


Figure 3.9: Geometry of forward pre-shower detector wedges.[54]

### 3.4.5 The DØ Calorimeter

The DØ calorimeter itself has been left unchanged from Run I. To accommodate the higher luminosity and faster bunch crossing times of the Run II Tevatron however, the readout of the calorimeter had to be upgraded. The calorimeter is a liquid argon-uranium sampling compensating calorimeter. Particles which pass through

the calorimeter interact with the material of the calorimeter and shower. The particles leaving the material (absorber) then ionize the liquid argon (active medium) and charge from the ionized liquid argon is collected at high voltage pads in each calorimeter cell. The geometry of a calorimeter cell is shown in Figure 3.10. The amount of charge collected is proportional to the amount of energy deposited in each cell. The DØ calorimeter also attempts to equalize the response of calorimeter signals from hadrons and electrons. This is accomplished by tuning the thickness and the material chosen for the absorbers.

The calorimeter is separated into 3 regions. The four innermost layers of the calorimeter are the electromagnetic layers. These layers are finely segmented and utilize depleted uranium absorbers. Just outside the electromagnetic layers are the fine hadronic layers. These are three layers of larger segmentation and utilize thicker uranium-niobium alloy absorbers. Beyond the fine hadronic layers is a single coarse hadronic layer, which utilizes a coarsely segmented absorber made of thick copper (stainless steel in the end-caps). The parameters of each layer are summarized in Tables 3.2 and 3.3[57], and the physical layout of the calorimeter is illustrated in Figure 3.11.

The electromagnetic calorimeter layers are designed to stop the showers that are produced by electrons and photons. The maximum of the electromagnetic showers (shower-max) for high energy EM particles is calculated to take place in the third

Module Type	EM	Fine Had.	Coarse Had.
Central			
$\eta_{det}$ coverage	$\pm 1.1$	$\pm 1.0$	$\pm 0.7$
Absorber Material	Uranium	Uranium (1.7% Niobium)	Copper
Readout Layers	4	3	1
Segmentation ( $\Delta\eta \times \Delta\phi$ )	$0.1 \times 0.1$ (Layers 1,2,4), $0.05 \times 0.05$ (Layer 3)	$0.1 \times 0.1$	$0.1 \times 0.1$
Thickness	1.4, 2.0, 6.8, 9.6 $X_0$	1.3, 1.1, 0.76 $\lambda_a$	3.2 $\lambda_a$
Total $X_0$	19.8	96	33
Total $\lambda_a$	0.76	3.16	3.2

Table 3.2: DØ Central Calorimeter Parameters.

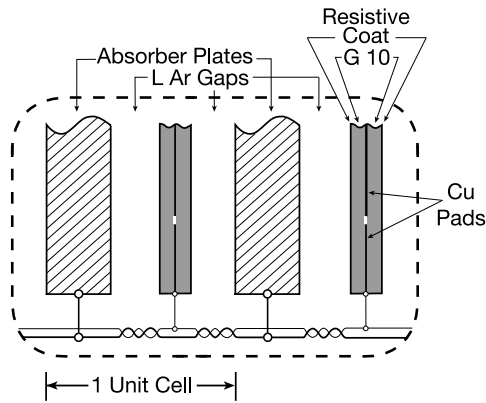


Figure 3.10: Geometry of a Calorimeter Cell.[54]

electromagnetic region, and thus this region is more finely segmented for a more precise measurement. This calculation still holds despite the fact that it was originally performed for the Run I detector which did not have the additional material of the

Module Type	EM	Fine Had.	Coarse Had.
Endcap			
$\eta_{det}$ coverage	$\pm(1.3-4.1)$	$\pm(1.6-4.5)$	$\pm(2.0-4.5)$
Absorber Material	Uranium	Uranium (1.7% Niobium)	Copper
Readout Layers	4	4 (IH) 4 (MH) 0 (OH)	1 (IH) 1 (MH) 1 (OH)
Segmentation ( $\Delta\eta \times \Delta\phi$ )	$0.1 \times 0.1$ (Layers 1,2,4), $0.05 \times 0.05$ (Layer 3)	$0.1 \times 0.1$	$0.1 \times 0.1$
Thickness	1.6, 2.6, 7.9, 9.3 $X_0$	$1.1\lambda_a$ (IH) $0.9\lambda_a$ (MH)	$4.1\lambda_a$ (IH) $4.4\lambda_a$ (MH) $< 6.0\lambda_a$ (OH)
Total Depth	$21.4 X_0$ ( $0.96 \lambda_a$ )	$4.4 \lambda_a$ (IH) $3.6 \lambda_a$ (MH)	$4.1 \lambda_a$ (IH) $4.4 \lambda_a$ (MH) $< 6.0\lambda_a$ (OH)

Table 3.3: DØ Endcap Calorimeter Parameters. IH denotes Inner Hadronic cells. MH denotes Middle Hadronic cells. OH denotes Outer Hadronic cells.

solenoid and the pre-shower absorber. Because it is more finely segmented and expected to absorb most of the energy of electromagnetic showers, the third layer (or floor) of the EM calorimeter is used to calculate the position of EM-objects identified by the calorimeter.

The readout electronics had to undergo a significant upgrade to accommodate the much faster bunch crossing rate in Run II. The rate changed from one bunch crossing



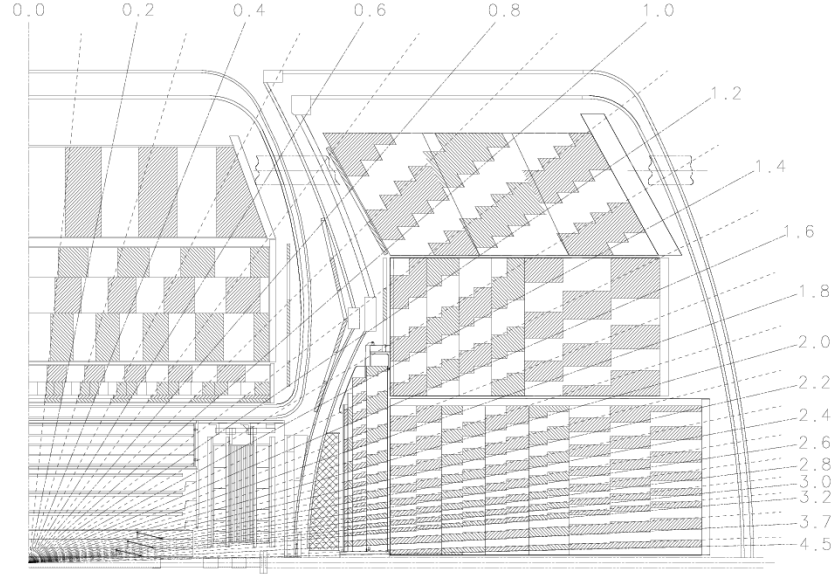


Figure 3.11: Layout of cells in the calorimeter. This figure is rotationally symmetric about the horizontal axis and exhibits symmetry of reflection about the vertical axis at  $\eta = 0$ . [54]

every three microseconds in Run I, to one bunch crossing every 396 nanoseconds in Run II. This increased interaction rate greatly complicates calorimeter readout due to the fact that charge from previous events are still being collected while additional events are taking place. This complication is handled through a process known as baseline subtraction, where the calorimeter dynamically assigns a value to the amount of energy at the time of a beam crossing and then subtracts that value from the energy deposited at a later time after the collision to obtain a measure of the charge collected for the current event [58].

### 3.4.6 Muon System

The outermost detector subsystem is devoted exclusively to the detection of muons. Because muons will not shower in the calorimeter, and because all other particles other than neutrinos should be contained by the calorimeter, the muon system is naturally placed outside of the calorimeter. The system is composed of sheets of scintillating pixels, proportional drift tubes (PDTs) and mini drift tubes (MDTs) for both a time measurement, to reject cosmic ray muons, and for a position measurement. A 1.8 T iron toroid magnet provides the ability for a momentum measurement independent of the central tracking system. The muon system is divided into a central muon system which gives coverage for  $|\eta_{det}| \leq 1$  and utilizes PDTs for position measurements, and a forward muon system which covers  $1 < |\eta_{det}| \leq 2$  with MDTs. Both systems employ scintillating counters for triggering and cosmic muon vetoing. Each muon subsystem has 3 layers known as the A, B, and C layers. The A layer is the innermost layer, and is positioned just outside the calorimeter, but inside the toroid. The B and C layers are positioned outside the toroid. In the region below the calorimeter, only partial muon coverage is possible due to the fact that the DØ support structure and readout electronics are located in this region.

The PDTs are rectangular gas filled volumes. Charged particles traversing this volume ionize the gas. Electrons from this ionization are collected and amplified by tungsten sense wires that run through the center of the chamber to provide a position

measurement of a charged particle. Comparison of the arrival time of the pulse signal from adjacent wires, and a measurement of charge deposition on vernier cathode pads located above and below wires allows for a position measurement resolution of approximately 1 mm[54]. The MDTs which cover the forward region are similar to the PDTs but have shorter electron drift time ( $< 132$  ns, as opposed to approximately 500 ns in the PDTs), and slightly better coordinate resolution of  $\approx 0.7$  mm [54].

Figure 3.12 shows the layout of PDTs and MDTs in an expanded view.

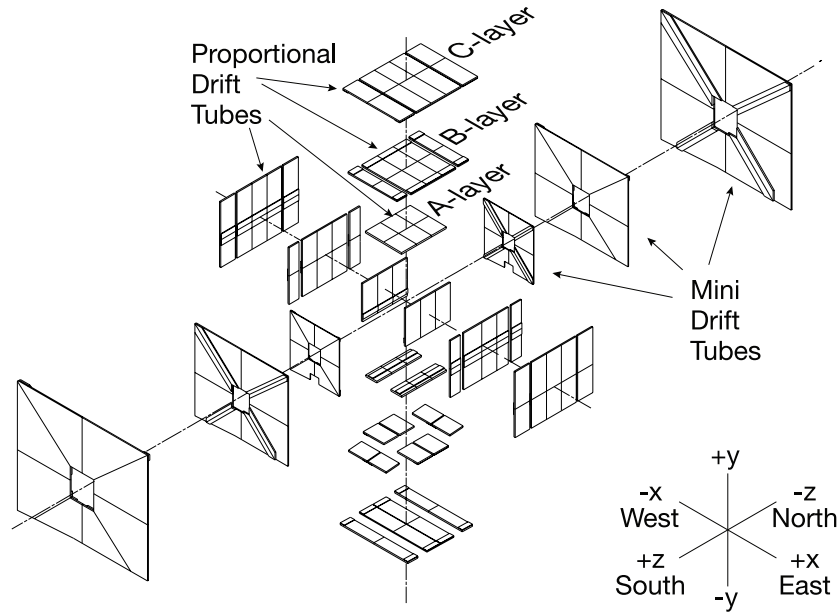


Figure 3.12: Expanded view of PDT and MDT layout in the muon system.[54]

Sheets of scintillating material serve to provide additional position measurements and are used for triggering, cosmic ray veto and track reconstruction. These sheets collect scintillation light from passing particles with a photomultiplier tube attached to one corner. Scintillating muon detectors are arranged in each layer except the B

layer of the central muon system as shown in Figure 3.13

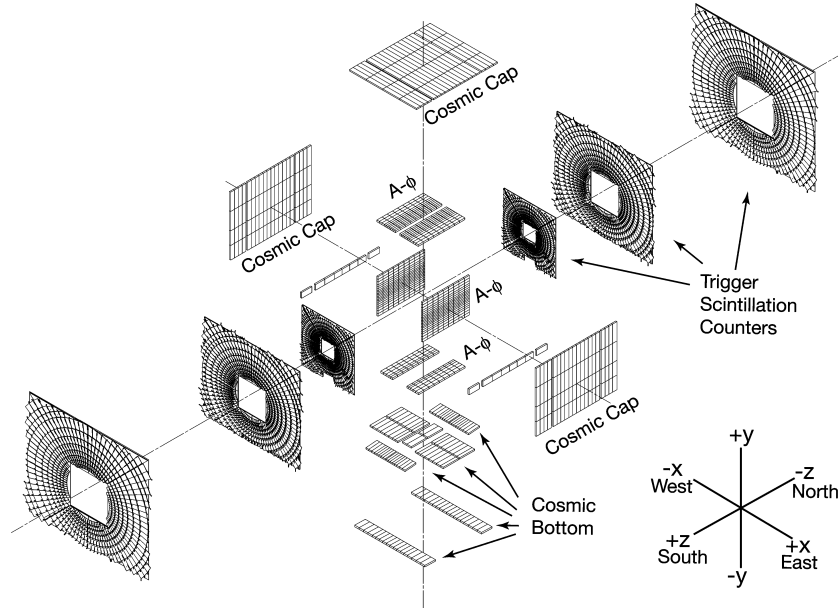


Figure 3.13: Expanded view of the scintillator layout in the muon system.[54]

## 3.5 Trigger

The DØ trigger system is a three tiered system whose purpose is to filter through events occurring in the DØ detector at a rate of 2.5 MHz and select only those events which have the signature of interesting physics for recording to tape. The recording rate is limited to approximately 50 Hz. This is acceptable because an overwhelming fraction (99.996%) of the bunch crossings in the Tevatron result in simple soft scatters. The trigger is designed to determine when a hard scatter has occurred and to select that event for recording. some of the telltale signs of hard scatters are the presence of

leptons, jets, central tracks, electromagnetic objects, and missing transverse energy. The trigger system looks for the signatures of one or more of these conditions in the detector as the data arrive. At  $D\bar{O}$  this is accomplished through a 3 tiered trigger system, the first two layers of which are illustrated in Figure 3.14. The first tier, level 1, is a hardware based system designed to make very quick decisions based upon the readout of individual components. The second tier, level 2, consists of a set of 5 pre-processors associated with the sub-detectors that build physics objects from the detector readout which are then passed to a global level 2 triggering computer that makes a selection decision. The third tier, level 3 consists of a farm of approximately 200 PCs that run the full reconstruction code on an event and decide whether any pre-defined criteria are met.

### **3.5.1 Level 1 Trigger**

The level 1 trigger system is a purely hardware based trigger designed to read events at a rate of 2.5 MhZ and pass events on at a rate of approximately 2 kHz. The level 1 system is divided into 4 subsystems. These subsystems are the calorimeter trigger (L1Cal), which selects events based on energy deposits in the calorimeter exceeding pre-defined limits; the muon system trigger (L1Muon) and the central track trigger (L1CTT), and checks them against pre-defined transverse momentum thresholds.

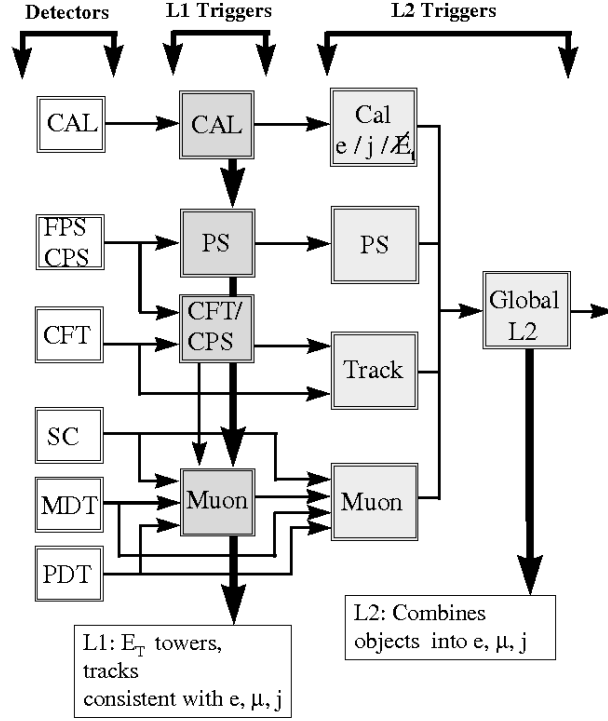


Figure 3.14: Configuration of the Level 1 and Level 2 trigger systems.[54]

### 3.5.2 Level 2 Trigger

The level 2 trigger system takes its inputs from the level 1 triggers as well as from the detector components themselves. It consists of 6 preprocessors and one global trigger. The preprocessors are each associated with a detector subsystem and receive their inputs from the detector subsystem(s) they are associated with and/or the level 1 trigger they are associated with. The preprocessors create physics objects(tracks, muons, jets, missing  $E_T$ ) for each event which are then taken as inputs by the global L2 trigger which makes a decision of pass or fail based upon the contents of the physics

objects in the event. In this way level 2 can utilize the matchings of physics objects in its decision making process. The six pre-processors at level 2 are: L2 calorimeter (L2CAL) which is used for the fast identification of jets, electromagnetic objects, and missing transverse energy; L2 Central Muon and L2 Forward Muon (L2MUC and L2MUF), which both serve the purpose of identifying muons from the muon system and utilizes calibration and precise timing information to improve the quality of the muon candidates from level 1; L2 Pre-shower (L2PS), which takes information for the forward and central pre-shower detectors and provides evidence for early shower development by giving a good spatial point for comparison with calorimeter clusters; The level 2 central track trigger (L2CTT) takes inputs from L1CTT and L2STT, the level 2 silicon track trigger, and provides the global processor with information on track isolation and track pointing information for future matching to calorimeter clusters and muon objects; L2STT uses the list of L1CTT tracks as seeds and takes its inputs from the SMT to improve rejection of spurious L1 triggers and provides the ability to trigger on tracks with a large impact parameter, which is a signature of the decay of long lived particles, such as  $B$  hadrons. These preprocessors send their results to the level 2 global trigger which combines all of the information available and makes a decision based upon a number of pre-defined criteria, such as matches of tracks to muons or calorimeter clusters, or jets plus a displaced track, etc. The events that pass these criteria are passed on to level 3, at a rate of approximately 1 kHz

### **3.5.3 Level 3 Trigger**

The level 3 trigger system is a full software based system running on a farm of Linux computers. These computers run the events through a more complete reconstruction and base their decisions on the complete physics objects and the relationships between them. This system is designed to read events in at approximately 1 kHz, and to output the events to tape at a rate of approximately 50 Hz.



## Chapter 4

### Event Reconstruction

The raw data from the DØ detector consists of digitized readout for each channel of each sub-detector. These readouts consist of pulse heights of collected charge in the calorimeter and silicon, light yields from the scintillators, and time differences in the muon drift chambers. In order to put all this data together for physics analyses, a computer program called DØ Reco is run over the raw data. DØ Reco applies corrections from calibration and alignment studies and groups 'hits' in various parts of the sub-detectors into "physics objects", such as electrons, muon, taus, jets, missing transverse energy, calorimeter clusters, vertices, and tracks. In many cases these base physics objects can be combined to improve efficiencies and reduce backgrounds. For instance, muons found in the muon system (local muons) can be matched to a track to create a "global muon" in order to get a better measurement of the muon momentum and its production vertex.

## 4.1 Track Reconstruction

In order to reconstruct tracks of charged particles through the detector, DØ Reco first finds clusters of hits in each layer of the SMT and the CFT. The energy weighted centroids of these clusters serve as inputs to the two tracking algorithms that run in parallel and form a set of candidate tracks. These candidate tracks are then subjected to a set of quality requirements in order to produce the final set of tracks. The two tracking algorithms which run in DØ Reco are known as the Histogramming Track Finder (HTF) and the Alternative Algorithm (AA). The AA algorithm finds track candidates by performing both an “inside-out” and “outside-in” extrapolation of clusters of hits in the detector. The HTF algorithm finds tracks by filling a histogram of track parameter space with values consistent with each hit in the CFT and SMT. Local maxima in this histogram are taken to be physical tracks.

### 4.1.1 AATrack

When the AA algorithm runs, it begins by looking for track candidates that begin in the SMT. It starts by finding “seed clusters” that may occur on any SMT barrel or F-disk. Track segments are then formed by searching for a second hit in any silicon layer of greater radius within a window in  $\phi$  of  $|\Delta\phi| < 0.08$ . If a second hit is found, a third hit is searched for in any further SMT layer. If a third hit is found, these three points are projected onto the  $x - y$  plane and are fit to a circle.

The resulting track segment candidate is kept if it passes all of the following criteria:

- The fitted circle's impact parameter (or distance of closest approach) with respect to the beam spot is less than 2.5 cm.
- The radius of curvature is at least 30 cm ( $p_T > 180$  MeV)
- The  $\chi^2$  of the fit is less than 16

For track segments meeting these requirements, the algorithm continues by searching the remaining layers of the SMT and CFT, in order of increasing radius, for hits to associate with the track segment. A hit is kept if the resulting  $\chi^2$  of the fit to a circle in the  $x - y$  plane increases by less than 16 for each new hit. If multiple hits in the same layer match the candidate, then the hypothetical track is split and each result is considered separately. The number of layers with missed hits is monitored, adjusted for dead and disabled channels. This process continues for each track hypothesis until the outermost layer is reached, at which point the track is accepted and passed onto the track selection stage, or until three contiguous layers are passed with a missed hit, at which point a track is rejected.

To locate tracks that have few or no hits in the SMT, the same algorithm is repeated, but starting from the outer layers of the CFT. Because the combinatoric background is much worse in the CFT, due to the lack of  $z$ -segmentation, the track candidates found in this manner are rejected if they are not consistent with a vertex that was identified in the track selection stage.

### 4.1.2 Histogramming Track Finder

The HTF algorithm finds tracks through local maxima of a histogram in track parameter space which is filled for track parameters consistent with each hit[59], as illustrated in Figure 4.1. The projection of a track on the  $x - y$  plane can be expressed in terms of three parameters. The radius of curvature  $\rho = qB/p_t$ , where  $q$  is the charge,  $B$  is the magnetic field and  $p_T$  is the transverse momentum of the particle; the impact parameter  $b$ ; and the azimuthal angle of the track trajectory at the point of closest approach  $\phi_0$ . For illustrative purposes we can assume that  $b \approx 0$ . In this limiting case, each point in the  $x - y$  plane maps to a line in the parameter space in the  $\rho - \phi_0$  plane. By examining the lines in parameter space associated with all points of a physical trajectory, the lines should form a vertex at the trajectories true curvature and direction. HTF discretizes this parameter space into a set of bins, and each hit in the detector fills a number of associated bins, and the vertices in parameter space are identified by searching for local maxima in the histograms. These vertices are used then to define a set of track candidates that are passed to the track selection algorithm along with the AA track candidates.

### 4.1.3 Track Selection

The track hypotheses given by the AA and HTF algorithms are first filtered by requirements on the number and type of missed hits along the track trajectory. The

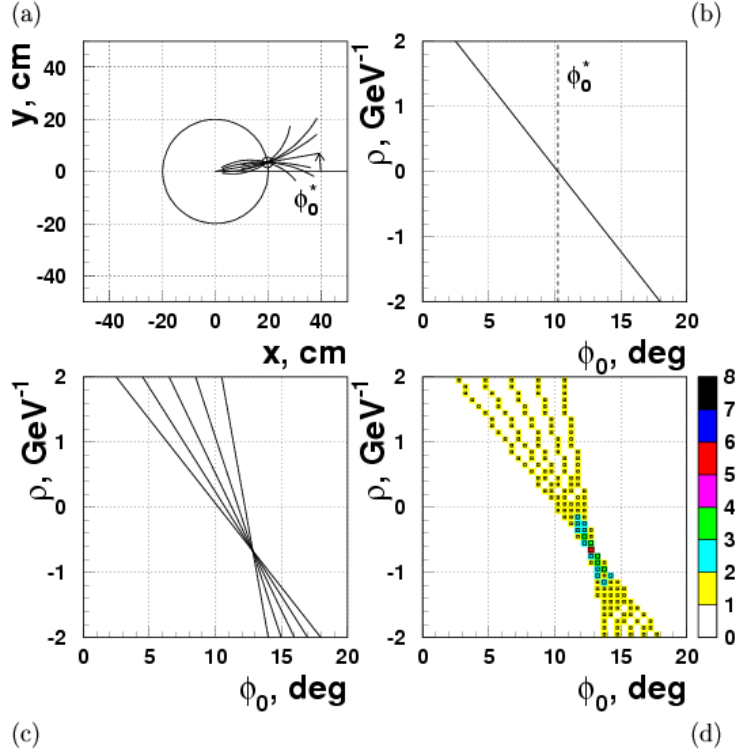


Figure 4.1: Sample track reconstruction with HTF. Plot a) shows the family of tracks that can be associated with a given hit. Plot b) shows the representation of the family of tracks associated with a given hit in curvature-azimuthal angle ( $\rho - \phi_0$ ) space. Plot c) shows the representation of 5 hits in  $\rho - \phi_0$  space. The intersection of these lines indicate the values of the true parameter values for the track that generated these hits. Plot d) illustrates how these lines are used to fill a histogram, where the intersection is determined as the local maximum.[59]

three types of hit misses are:

- **Inside Misses:** Missed hits between the innermost and outermost hits on the track
- **Forward Misses:** Missed hits after the outermost hit on the track
- **Backward Misses:** Missed hits before the innermost hit on the track

Together, forward and backward misses are referred to as outside misses.

For a track to pass selection, it must satisfy the following:

- The track must have at least four hits, with hits in axial and stereo layers of the complete tracking system.
- The total number of hits must greater than five times the total number of misses.
- The total number of outside misses must be less than seven.
- The total number of inside misses must be less than four.
- The track must have fewer than three inside misses in the SMT.
- For tracks with inside misses:
  - The total of inside and forward misses must be less than five.
  - The total of inside and backward misses must be less than four.

The tracks which pass these requirements are then filtered for duplicate or near duplicate tracks. This is done by sorting the remaining track candidates by the number of hits (in descending order), the number of misses (in ascending order) and the fit  $\chi^2$  (in ascending order). Candidates with axial hits that are not shared with earlier entries in the list are accepted, and candidates that do share hits with previous entries are accepted if:

- $N_{shared} \leq \frac{2}{3}N_{tot}$

- $N_{shared} \leq \frac{N_{tot}}{5}$  and  $N_{tot} - N_{shared} > 3$

Where  $N_{tot}$  is the total number of axial hits on a track and  $N_{shared}$  is the number of those hits that are in common with previous track candidates.

Finally, the remaining tracks are grouped by common vertices by an algorithm similar to the one in described in Section 4.2[60]. These vertices are required to have five tracks with  $\chi^2 < 36$ . The track candidates are then re-sorted, filtered as before except that those associated with a vertex are “granted” two addition unshared hits, and previously accepted hypotheses may be rejected, with a preference for keeping candidates that are associated to a vertex.

The tracking efficiency under these conditions are measured by [61] to be approximately 95% for low  $p_T$  tracks, as shown in Figure 4.2

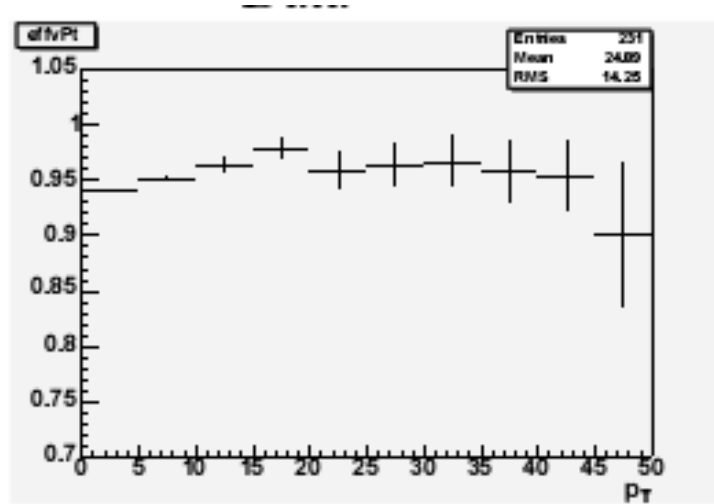


Figure 4.2: Tracking efficiency in data measured with single muons. [61]

## 4.2 Vertex Reconstruction

The vertexing algorithm[56] is used to determine the position of the hard-scatter interaction that was responsible for triggering the event. Finding the primary vertex is a two pass process. Initial vertex candidates are built from tracks that satisfy loose selection requirements. In the second pass, the track selection cuts are tightened and the vertices are refit from the remaining tracks. The primary vertex is chosen with a probabilistic method based on the associated track momenta.

In the first pass of the vertex finding algorithm, tracks are required only to have a transverse momentum greater than  $0.5 \text{ GeV}/c^2$ , greater than one SMT hit and the significance of the distance of closest approach ( $\frac{DCA}{\sigma_{DCA}}$ ) to the detector origin must be less than 100. These tracks are fit to a common vertex position with a Kalman filter[60] algorithm. If the resulting  $\chi^2$  of the fit is greater than ten, the track with the largest contribution is removed, and the process is repeated until the vertex fit  $\chi^2$  is less than ten. This process is then repeated over the excluded tracks to identify additional vertices, and this set of preliminary vertices is then passed to the second pass of the algorithm.

In the second pass, the preliminary vertex positions are used to determine the location of the beam spot. The first pass algorithm is applied again, with the exception that tracks are required to have a DCA significance of less than three with respect to the measured beam spot. In order to separate the primary vertex from the



grazing minimum bias collisions, each vertex is given a likelihood value that is formed from the associated track momenta[62]. For each track associated with any vertex, a probability,  $P(p_T)$  is assigned such that:

$$P(p_T) = \frac{\int_{\log_{10}(p_T)}^{\infty} F(x) dx}{\int_{\log_{10}(0.5)}^{\infty} F(x) dx} \quad (4.1)$$

Where  $F(x)$  is the distribution of  $x = \log_{10}(p_T)$  for tracks from Monte Carlo minimum bias as shown in Figure 4.3. For each vertex, the product of these probabilities for each associated track is calculated and weighted by the track multiplicity to form a probability that the vertex is a minimum bias vertex. The vertex with the lowest probability for being a minimum bias vertex is selected as the primary vertex.

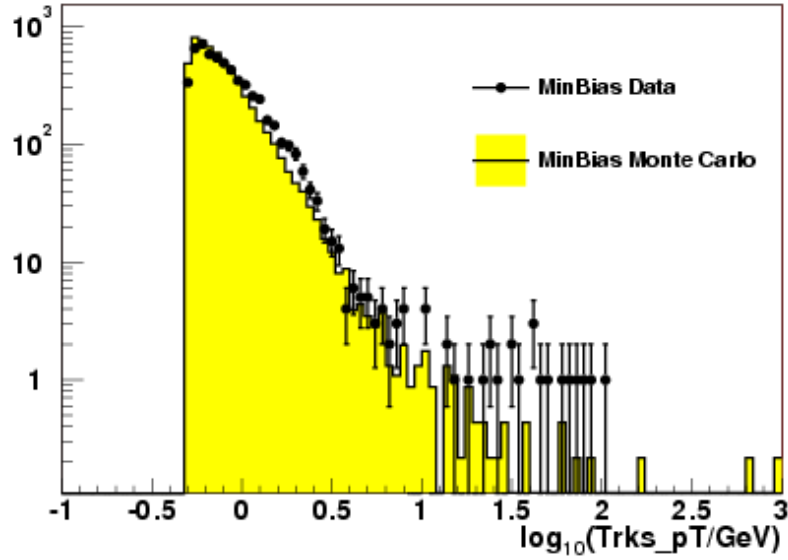


Figure 4.3: Distribution of  $\log_{10}(p_T)$  for tracks from minimum bias events. The data distribution is taken from from a sample of  $Z \rightarrow \mu\mu$  events.

### 4.2.1 Vertex Fitting

Vertex fitting is accomplished with a Kalman filter[60], which is an algorithm to identify the vertex position,  $\vec{x} = (x, y, z)$  and the momentum  $q_k$  for every track  $k$  associated with it. Every track is represented as a vector of track parameters,  $\mathbf{m}_k$ , with components  $z_0, \phi, \cot(\theta)$ , impact parameter, and curvature. For each vertex, a measurement vector and its error matrix may be defined as:

$$\vec{d}^m = \begin{pmatrix} \mathbf{m}_1 \\ \mathbf{m}_2 \end{pmatrix} \quad (4.2)$$

$$V = \begin{pmatrix} V_1 & 0 \\ 0 & V_2 \end{pmatrix} \quad (4.3)$$

A function  $\vec{d}(\vec{q})$ , then defines the track parameters for a given  $\vec{q}$ . With this information, the Kalman filter algorithm then minimizes the equation:

$$\chi^2 = (\vec{d}^m - \vec{d}(\vec{q}))^T V^{-1} (\vec{d}^m - \vec{d}(\vec{q})) \quad (4.4)$$

through an iterative procedure described in[56] to find the vertex fit parameters.

## 4.3 Muons

Muons are first reconstructed locally in the muon system before being matched to tracks in the tracking detectors. In the muon system, hits in the drift chambers are used to make local track segments in each layer (A, B, and C) of the muon system. Hits in the scintillator paddles are added to these segments. Segments

consistent with a common trajectory are merged into local muon tracks[63]. The local tracks are then matched to central tracks identified in the CFT and SMT to form a global muon. Segment reconstruction begins by only considering PDT and MDT hits consistent in time with a beam crossing. This helps to reject backgrounds from the radioactive environment and (anti-) protons which have scattered off the beam pipe or the Tevatron magnets. The timing of the hits in each wire of a drift chamber constrain the location of the muon to a circle surrounding the wire. All possible pairs of hits within a chamber are formed, provided that they are not on the same drift circle and are separated by less than 20 cm in the  $y$  direction. Additionally, two wire hits may not be in the same plane of wires unless they are consistent with a track passing between adjacent wires, see Figure 4.4.

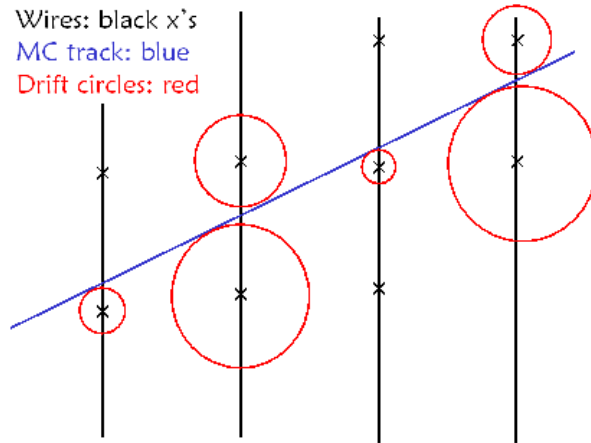


Figure 4.4: Sample of a muon traversing a drift chamber. Tracks are constrained by the hits timing information to lie on circles (red) around the wires that contain hits. [63]

Pairs of hits are combined into track segments of three or more hits and fit to a straight line, with every permutation allowed. The segments are sorted first by the number of hits and then by the fit  $\chi^2$ . All but the first four of these segments are used to reconstruct local muons. Nearby scintillator hits in the same layer are associated with the segment. Segments in each layer are then matched to one another and fit again into local tracks, although the fit is not required to converge[64]. The toroid provides a local  $p_T$  measurement for muons with segments in both the A and B or C layers of the muon system. In the cases where the fit does not converge, an estimate of the muon  $p_T$  is obtained by using the bending angle between segments. The resolution of transverse momentum in the muon system is limited at low energies by multiple scattering in the iron toroid and at high energies by the resolution of the drift chambers and the scintillators.

If the local fit converges, the five standard track parameters 4.2.1 are obtained from the resulting momentum measurement, the A layer position, and the propagation of the track back to the point of closest approach to the primary vertex. All central tracks with  $p_T > 1$  GeV and  $\Delta\phi < 1$  and  $\Delta\theta < 1$  are considered for matching to the local muon track. To match one of these tracks to a local muon track, a new set of track parameters  $P_f$  are calculated as an average of the central track and local muon track parameters,  $P_{trk}$  and  $P_{loc}$ , weighted by their uncertainties:

$$P_f = (E_{trk}^{-1} + E_{loc}^{-1})^{-1}(E_{trk}^{-1}P_{trk} + E_{loc}^{-1}P_{loc}) \quad (4.5)$$

where  $E_{trk}$  and  $E_{loc}$  are the central and local track error matrices. The match is obtained by taking the central track with the minimum  $\chi^2$ , where[65]:

$$\chi^2 = (P_{trk} - P_{loc})^T (E_{trk} + E_{loc})^{-1} (P_{trk} - P_{loc}). \quad (4.6)$$

When the local muon fit does not converge, local muon tracks are propagated to the A layer only and the closest central track in  $\theta - \phi$  space is chosen as the track match, provided it satisfies the initial criteria for the  $\chi^2$  matching. For the purposes of this dissertation, all muon kinematic variables are those of the central track, even when the local muon fit converges.

<b>nseg</b>	<b>Muon Type</b>	<b>Track match</b>
3	local muon track	Yes
2	BC segment	Yes
1	A-segment	Yes
0	Central track	Yes
-1	A-segment	No
-2	BC-segment	No
-3	Local muon track	No

Table 4.1: Muon nseg definitions.

After a muon is found, it is assigned a category,  $nseg$ , depending on whether it contains A, B, or C layer segments and the presence of a matching track, as shown in Table 4.1 [66]. A quality is also defined as being either tight, medium, or loose based on the  $nseg$  and the number and location of hits in the muon system[67].

## 4.4 Photon Reconstruction

To reconstruct photons, a clustering algorithm known as *CellNN* is used to reconstruct clusters of energy in the calorimeter. Since photons are expected to deposit most of their energy in a narrow region of the electromagnetic section of the calorimeter, only clusters that have at least 90% of their energy contained in the electromagnetic calorimeter are considered. Further cuts to limit the width of the cluster are applied once the cluster has been found.

### 4.4.1 The CellNN Algorithm

The CellNN algorithm creates clusters in a two step process. First clusters are made on a layer by layer (or floor by floor) basis. These floor clusters are then combined into global calorimeter clusters. The floor by floor clustering begins by searching for a local energy maximum cell to serve as a seed cell for the floor cluster. This cell is defined to be any cell with an energy above a threshold of 200 MeV whose energy is greater than that of each of its neighbors. In the EM calorimeter, a neighboring cell is defined as any cell which shares a face, so that each EM cell has only 4 neighbors. The algorithm then iterates through cells in order of decreasing energy down to a threshold of 25 MeV, and each cell is added to the floor cluster that contains its highest energy neighbor. The cluster centroid is computed as an energy weighted mean of the positions of all cells belonging to the floor cluster. In

the case where a cell could be put into more than one cluster, the energy in each cell at the boundary between separate clusters is shared based upon a parameterization of shower shapes and the distance of the cell to the cluster centroid described in[68]. In the case of EM floor clusters which have seed cells that share a corner, the difference between the minimum energy of the two seed cells and the maximum energy of the two common neighbor cells are compared to a threshold of 150 MeV. If this difference is below the threshold, the two clusters are merged, see Figure 4.5

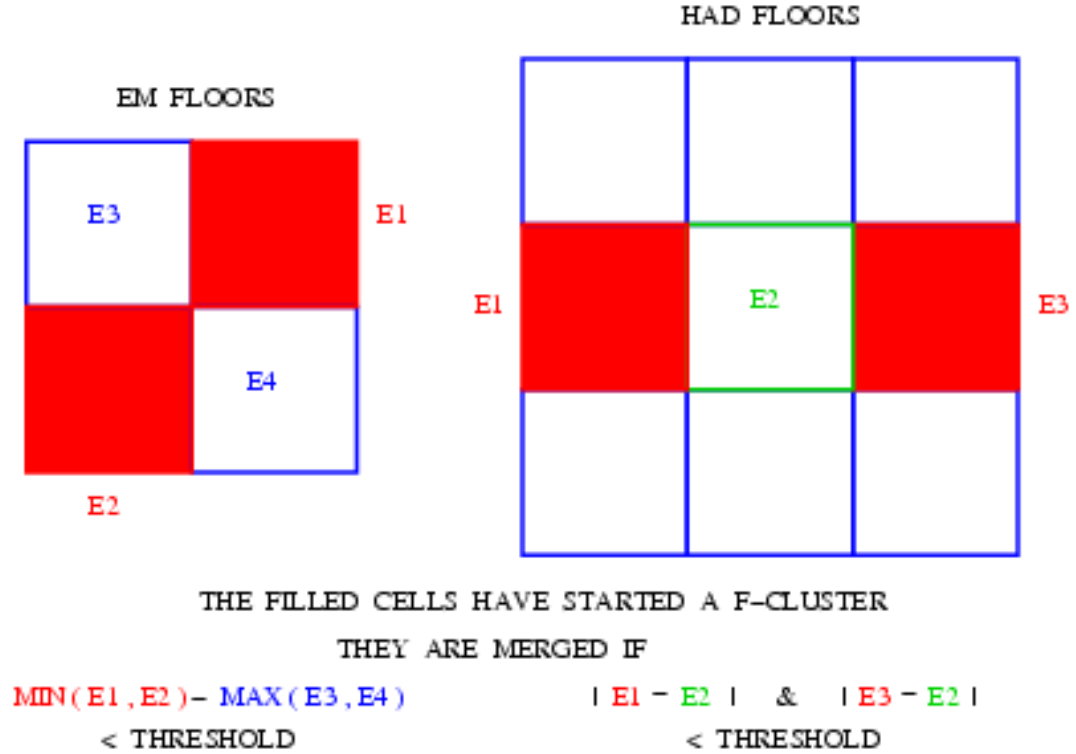


Figure 4.5: Floor cluster merging procedure in the CellNN algorithm.[68]

Once the floor clusters are built, the global clustering begins by using each floor

cluster in the third layer of the EM-cal as a seed cluster. Floor clusters in EM4 are added to a global cluster if their centroids lie in a cone defined by a given radius (7cm at layer 3) and in the direction defined by the line from the primary vertex to the EM3 floor clusters centroid. This same procedure is applied on up through the calorimeter into the hadronic section for the reconstruction of jets, and then back down to the first and second layers of the electromagnetic calorimeter. If no floor clusters are found at EM3, EM4 floor clusters will then initiate global clusters, and so on up through the calorimeter until a non-empty floor is found. If a floor cluster cannot be merged with another floor cluster, then it will start its own global cluster. Global clusters are not allowed to have a missing floor in the middle of the cluster, except in special regions of the hadronic layers. If a floor cluster can be merged with multiple clusters from the starting floor, the floor clusters energy is shared with each of the starting global clusters based upon a shower shape parameterization described in [18] and the cell distance to the cluster centroid, similar to the sharing of energy for cells in floor clusters. The longitudinal shower shape of each global cluster is then examined. If a significant minimum occurs in either EM4 or FH1, the global cluster is then split into two separate clusters: an EM cluster and a hadronic cluster, and the cells in the floor containing the minimum share their energies with each cluster. Global clusters are then kept if their total energy is above a threshold of 1 GeV.



## Chapter 5

### Event Selection

The analyses that follow were performed on data taken by the DØ detector between April of 2002 and August of 2004, corresponding to approximately  $550 \text{ pb}^{-1}$  of data, as shown in Figure 5.1.

Proton-antiproton collision events at the Tevatron occur at a rate of 2.5 MHz. The rate at which events can be recorded to tape is limited to 50 Hz, which means that an experiment must very carefully define which events are of enough interest to be written to tape. In the two analyses of  $X(3872)$  decays outlined in this paper, the  $X(3872)$  is searched for in decays to  $J/\psi$ 's plus other particles. The reason for choosing these decay modes rests primarily with our ability to trigger. The inclusive  $J/\psi$  production cross section at the Tevatron is extremely high, approximately  $240 \text{ nb}$ [69], and because of their characteristic decays to  $\mu^+\mu^-$ , they are relatively easy to trigger. The initial discovery of  $X(3872)$  was in the decay mode  $X(3872) \rightarrow J/\psi\pi^+\pi^-$ . A study of this state at DØ should therefore begin with this decay mode.

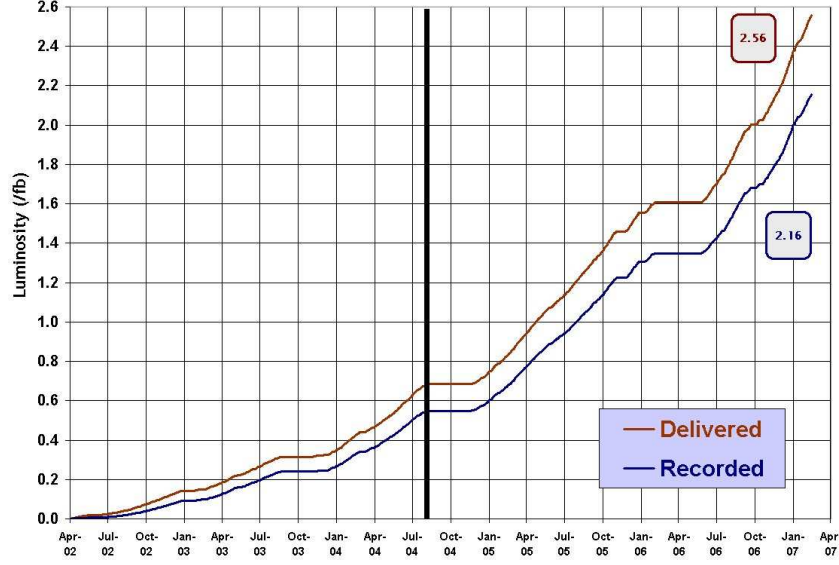


Figure 5.1: Integrated luminosity at DØ from 2002 to the present. The data sample used in the following analyses were collected before August 2004, which is denoted by the vertical line.

Additionally, one of the possible charmonium assignments for the  $X(3872)$  ( $J^{PC} = 1^{++}$ ) should couple strongly to  $J/\psi\gamma$ , and thus  $J/\psi\gamma$  candidate events are also selected for study.

## 5.1 Dimuon triggers

Triggering on  $J/\psi$  candidate events begins in the level 1 muon trigger system which scans the muon system for signatures of muons. At level 1 these signatures are separated into four categories based on loose and tight requirements in either muon scintillator or wire chambers. Loose scintillator triggers require only an A layer

scintillator hit, and loose wire triggers require an A layer scintillator hit matched to an A layer wire stub. Tight requirements in the scintillator search for matches between A and B layer scintillator hits in the forward system and A and C layer hits in the central system, while tight wire triggers match A and B layer wire stubs to A and B layer scintillators in the forward section and A and C layer wire stubs to A and C layer scintillator hits. At level 2 these muon candidates are then matched to tracks in the central tracker, and the trigger is fired if the track matched muon candidates satisfy a pre-defined  $p_T$  cut and a track match quality cut.

The primary trigger responsible for triggering  $J/\psi$  decaying to  $\mu^+\mu^-$  is called DMU1\_1L1MM2. This trigger requires that two muons meeting tight scintillator requirements[70] are present at level 1. At level 2, only one muon meeting the level 2 medium quality[71] requirements is required for an event to pass. At level 3, the trigger is satisfied if there is a primary vertex with z-coordinate within  $\pm 35$  cm of the center of the detector, and one loose and one medium[72] central muon candidates with  $p_T$  greater than 2 GeV.

## 5.2 Dimuon Skim

Because DØ is a multi-purpose detector, the dimuon triggers used in this analysis are run in conjunction with many other triggers that are used for other analyses. A large fraction of the full data set that is written to tape naturally contains events

that would be thrown out during selection cuts. In order to reduce processing times for physics groups, the full data set is divided up into smaller subsets known as “skims.” An event is tagged for one or more skims during reconstruction based upon a set of predefined selection criteria based on the physics objects reconstructed in the event. Because the final states in this analysis depend on the reconstruction and identification of a  $J/\psi$  decaying to  $\mu^+\mu^-$ , a dimuon skim known as AA\_JPSI is used as the initial data set. This skim tags events that meet the following requirements:

- The event must contain two certified muons of opposite charge.
- At least 2 muons must have transverse momentum greater than 1.5 GeV.
- Each muon must be associated with a track that contains at least one hit in the CFT.
- At least one of the muon in the event must have *nseg* equal to 3.
- For muons with *nseg* greater than 0, its transverse momentum must be greater than 1.5 GeV
- For muons with *nseg* equal to 0:
  - The dimuon transverse momentum must be greater than 4.0 GeV.
  - a muon in calorimeter track (MTC) is searched for.

- $\text{CalEsig}() > 0.015 * \text{CalNLayer}()$ , where  $\text{CalEsig}$  is the significance of energy given to an MTC track, and  $\text{CalNLayer}$  is the number of calorimeter layers associated with an MTC track
- Its total momentum must be less than 7 GeV.
- The transverse momentum of the second muon must be greater than 2.5 GeV.
- The  $\chi^2$  of the global muon fit must be less than 25 for both particles.
- The dimuon invariant mass must be greater than 2.5 GeV.
- If the dimuon mass is greater than 3.6 GeV:
  - $n_{\text{seg}}$  greater than 1 for both muons
  - Each muon must have a transverse momentum greater than 2.5 GeV.

Note that events are selected independently of trigger requirements. After selecting the skim, events are further required to have fired any dimuon trigger. Also note that the dimuon invariant mass is the Lorentz invariant mass of the dimuon system.

### 5.3 $J/\psi\pi^+\pi^-$ candidate selection

To select  $J/\psi\pi^+\pi^-$  candidates, events which fired a dimuon trigger are searched for dimuon candidates which are required to have a common vertex, opposite charge,

the candidate  $p_T$  is greater than 5 GeV, and an invariant mass within the  $J/\psi$  mass window of 2.80 to 3.35 GeV, as shown in Fig. 5.2. Each muon is also required to have a matched track, and  $nseg$ , see Table 4.1, greater than zero. Two charged tracks

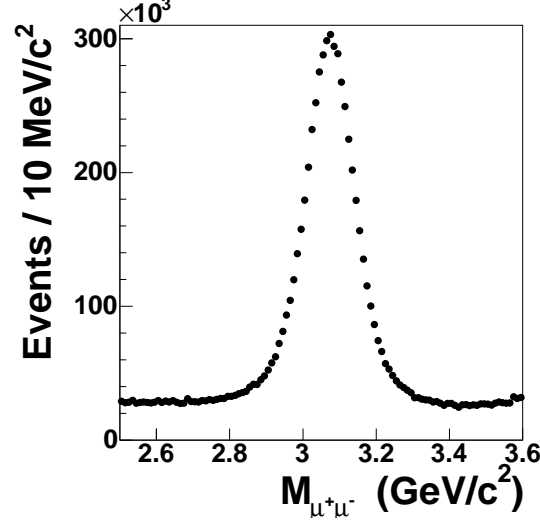


Figure 5.2: Dimuon invariant mass spectrum in the  $J/\psi$  mass window.

with opposite charge are then added to the  $J/\psi$  candidate under the assumption that they represent the path of charged pions. The 4 tracks constituting the  $J/\psi\pi^+\pi^-$  candidate are then required to have at least one hit between them in the silicon in order to remove bad tracks. The candidate is also required to have a 4 track vertex  $\chi^2$  less than 16. After applying these basic quality cuts, the invariant mass distribution is plotted, as  $M(\mu^+\mu^-\pi^+\pi^-) - M(\mu^+\mu^-)$  to remove the resolution effect of the  $J/\psi$ , see Fig. 5.3. In this sample, the obvious peak corresponds to the well known  $\psi(2S)$  charmonium state which also decays prominently to  $J/\psi\pi^+\pi^-$  [18].

In the expected mass window ( $0.73 < \Delta M < 0.81$  GeV) for the  $X(3872)$ , no

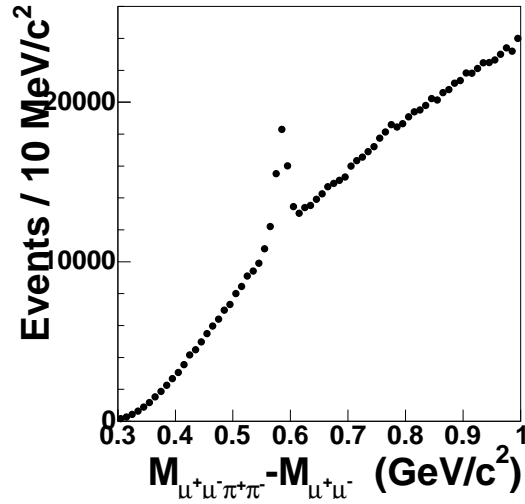


Figure 5.3:  $M(\mu^+\mu^-\pi^+\pi^-) - M(\mu^+\mu^-)$  With only basic quality cuts applied. The invariant mass difference between the 4-particle candidate and the dimuon candidate is used in place of the 4 particle invariant mass in order to cancel resolution effects.

obvious peak is observed, indicating that combinatoric backgrounds dominate over any signal. In order to determine whether the  $X(3872)$  is in this sample, as many random combinations of tracks as possible must be removed. In order to accomplish this, the lowest transverse momentum tracks are removed, as they are the largest sources of combinatoric backgrounds. Since the  $X(3872)$  is not a particularly heavy object, it is dangerous to cut too hard on transverse momentum for risk of removing the signal. The transverse momentum of all tracks is plotted in Figure 5.4. In order to remove a significant number of fake tracks, a transverse momentum cut is made for each pion candidate track that requires  $p_T^{\pi^\pm}$  to be greater than 0.7 GeV.

The resulting invariant mass distribution, shown in Figure 5.5 still shows that the sample is dominated by combinatoric backgrounds, with little evidence for  $X(3872)$ .

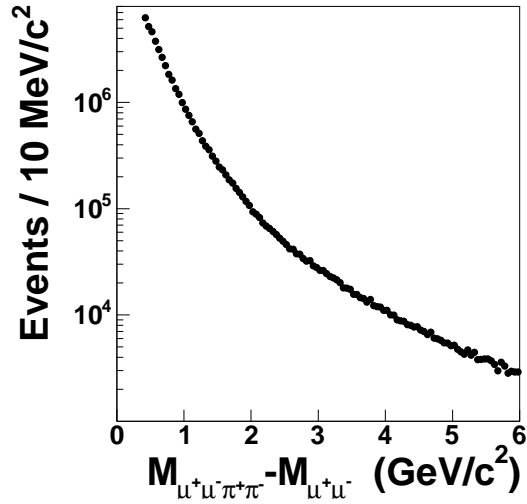


Figure 5.4: Transverse momentum of tracks in events selected by the dimuon skim.

In order to further reduce combinatoric backgrounds, a variable  $\Delta R = \sqrt{\Delta\eta^2 + \Delta\phi^2}$  is computed for each pion track momentum with respect to the momentum of the 4 track candidate at the point of closest approach to the primary vertex. Both pion track candidates are required to have  $\Delta R$  values less than 0.4. The resulting invariant mass distribution after applying this cut is shown in Figure 5.6.

The tracks that are accepted are then combined, under the assumption that the non-muon tracks are charged pions, to form an  $X(3872)$  candidate. While the above kinematic cuts were made to reduce the combinatoric background inherent in hadronic collisions, the combinatoric backgrounds are still very high. To make the combinatorics more manageable, a further cut was introduced based upon the BELLE collaboration's observation that the di-pion invariant mass spectrum was



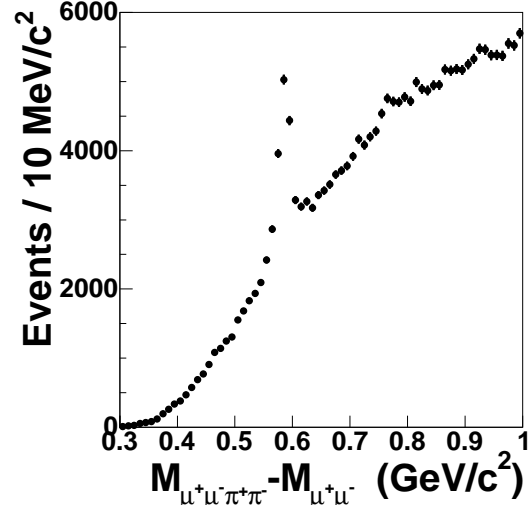


Figure 5.5:  $M(\mu^+\mu^-\pi^+\pi^-) - M(\mu^+\mu^-)$  with only basic quality cuts in addition to a pion  $p_T$  cut.

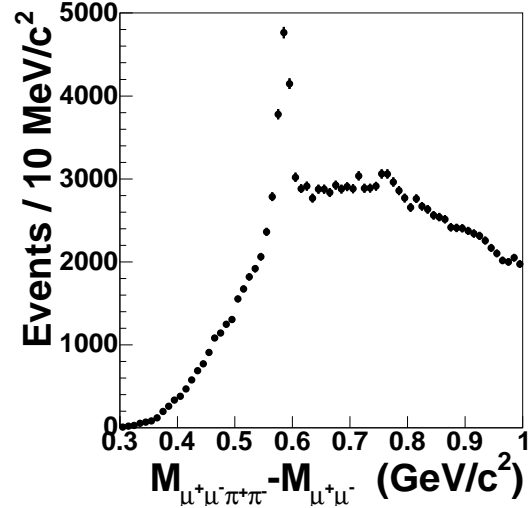


Figure 5.6:  $M(\mu^+\mu^-\pi^+\pi^-) - M(\mu^+\mu^-)$  with only basic quality cuts in addition to a cut on each pions  $p_T$  and  $\Delta R$ .

heavily skewed toward the upper kinematic limit[2]. Noting this, a further cut, requiring the two pion reconstructed invariant mass to be greater than 0.52 GeV, was

used. The result of these selection criteria is shown in Figure 5.7

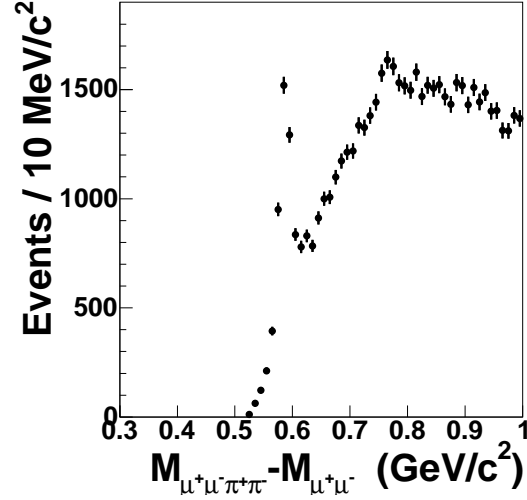


Figure 5.7:  $M(\mu^+\mu^-\pi^+\pi^-) - M(\mu^+\mu^-)$  with all analysis cuts applied.

As can be seen from Figure 5.7, a peaking structure near the expected mass of the  $X(3872)$  is seen. In Chapter 6 this data sample will be analyzed to make a measurement of the mass of the  $X(3872)$ . At the same time, the  $X(3872)$  content of this sample will be compared to the  $\psi(2S)$  charmonium state in a number of production and decay variables. A measurement of the lifetime properties of these two states will also be performed at that time. It is well known that charmonium production at the Tevatron proceeds through “prompt”  $p\bar{p}$  interactions as well as through  $B$  meson decay. Measurements of the  $X(3872)$  prompt fraction can test the charmonium hypothesis. If it is found that the  $X(3872)$  has a significantly different prompt fraction than other well known charmonium states, then charmonium hypotheses could be severely limited. However, before proceeding with these analyses, there is one other

dataset that will be used for analysis.

## 5.4 $J/\psi\gamma$ selection

This decay channel was selected for several reasons. First, an observation of  $X(3872)$  in this decay channel would require that the  $C$  parity of  $X(3872)$  be positive. Although other experiments have proclaimed this to be the most likely result, observation of this decay channel would leave no doubt. Secondly, for some charmonium hypotheses, the naive expectation would be that this channel should dominate due to the fact that it is an isospin conserving decay while the decay to  $J/\psi\pi^+\pi^-$  is not. More recent calculations however have stated that this does not have to be the case however. Lastly, for nearly every proposed theoretical interpretation of the  $X(3872)$ , the expected dominant decay channels involve neutral particles in the final state, primarily photons or neutral pions. While the DØ detector was not designed to detect these particles individually at such low energies, it is not impossible to do so. Searching for the  $X(3872)$  in this decay channel then is a natural place to start testing the limits of the DØ detector.

$J/\psi$  candidates were selected for this channel in much the same way as the above section, but with the further requirements that the muons from the  $J/\psi$  candidate have an  $n_{\text{seg}}$  value greater than 1, and that the  $p_T^{J/\psi}$  be greater than 7 GeV. The central electromagnetic calorimeter is then searched for CellNN clusters. These clusters

are required to have at least 90% of their energy in EM cells, and no more than one cell at layer 1 in order to reduce the contributions from  $\pi^0$ ,  $\eta$  and other hadrons that decay into two photons. A track match veto is also applied which requires that the spatial  $\chi^2$  probability of the best potential track match be less than 1% to eliminate most of the contribution from electrons from our sample. The clusters that are found by this method constitute the photon candidates. The energy of the candidate photons are taken to be the sum of the energy deposited in each cell associated with the cluster. In order to reconstruct the 4-vector of the photon, the momentum vector is determined as the vector with a magnitude equal to the reconstructed energy in the direction of the line passing through the  $J/\psi$  decay vertex and the energy weighted centroid of the cluster at the third layer of the electromagnetic calorimeter. With the momentum of the photon determined, it is then combined with the  $J/\psi$  to form an  $X(3872)$  candidate, and the resulting invariant mass distribution plotted in Figure 5.8, again in the variable  $\Delta M = M(\mu^+\mu^-\gamma) - M(\mu^+\mu^-)$ .

As can be seen from Figure 5.8, the  $\chi_c$  states appear as a strong peak, signaling that this sample certainly contains a large number of photons. However, no such peaking structure is obvious in the  $X(3872)$  mass region. In Chapter 7, this sample will be examined with more scrutiny and a limit on the relative branching ratio for this state will be set.

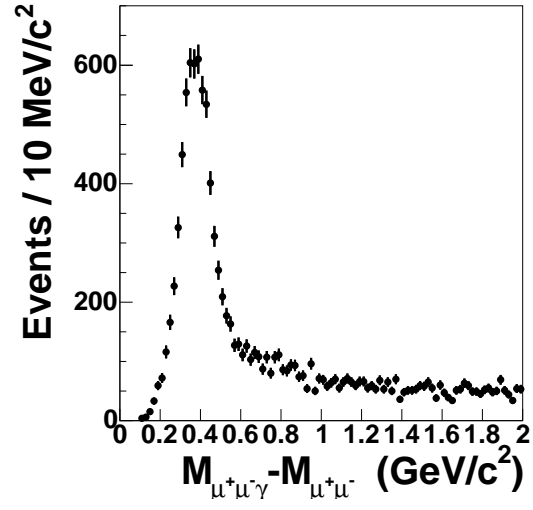


Figure 5.8:  $M(\mu^+\mu^-\gamma) - M(\mu^+\mu^-)$  with all analysis cuts applied.

## Chapter 6

### Analysis of $X(3872) \rightarrow J/\psi\pi^+\pi^-$

#### 6.1 Monte Carlo Simulation

Monte Carlo simulation can be a poor description of the data, therefore Monte Carlo is used primarily to understand resolution effects and mass biases for the two expected physics signals in the data, the  $\psi(2S)$  and  $X(3872)$ . Two different Monte Carlo samples were used. The first sample consisted of  $\psi(2S)$  decaying to  $J/\psi\pi^+\pi^-$ , and the second represented  $X(3872)$  decaying in the same manner. Because little is understood about the composition of  $X(3872)$ , this sample was created by simulating a “heavy”  $\psi(2S)$  in which the  $\psi(2S)$  mass was artificially set to 3872 MeV. These simulated events are then passed through a detector simulator which simulates the outputs of the DØ detector, and subsequently run through the reconstruction algorithms outlined in Chapter 4. With 23,000 simulated X events and 24,000 simulated  $\psi(2S)$  events, the mass difference  $M(J/\psi\pi^+\pi^-) - M(J/\psi)$  for each candidate from

the reconstructed events are plotted in Figure 6.1.

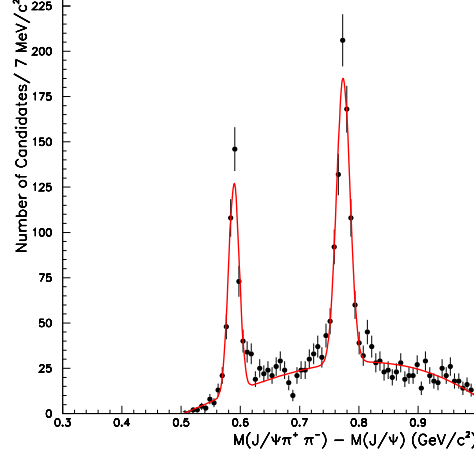


Figure 6.1: Invariant mass difference distribution in Monte Carlo for combined  $X(3872)$  and  $\psi(2S)$  samples.

This distribution is then fit to a 3rd order polynomial background shape plus two Gaussian to represent the  $X(3872)$  and  $\psi(2S)$ . The results of this fit indicate that we should expect the  $X(3872)$  width to be  $27\% \pm 10\%$  wider than that  $\psi(2S)$  peak, and that we should expect to find the  $X(3872)$  mass difference at  $0.773 \pm 0.00060$  GeV and the  $\psi(2S)$  mass difference at  $0.589 \pm 0.00057$  GeV.

## 6.2 Mass Measurement

To measure the mass of the  $X(3872)$ , the mass difference plot of Figure 5.7 is fit to a background function plus two signal Gaussian, one each for the  $\psi(2S)$  and  $X(3872)$ . The background function is chosen to be a 3rd order polynomial for the

purposes of keeping the fit simple and because it describes the data well. The fit was performed using the MINUIT minimization processes on a  $\chi^2$  between the data and the fit curve. Because MINUIT, or any other minimization software for that matter, is a numeric algorithm, the resulting fit is somewhat dependent on the initial guesses made for each parameter in the fit. This is due to the fact that the software cannot distinguish between an absolute minimum and a local minimum if a local minimum occurs far from any other minimum of a function. As initial guesses, the expected mass difference and peak width for the  $\psi(2S)$  and  $X(3872)$  obtained from the Monte Carlo are used, along with parameters for the background curve that approximately follow the shape observed in data. An initial round of fitting is first performed assuming no contribution from  $X(3872)$ . For these initial fits, the errors for each bin in the expected  $X(3872)$  signal region are artificially set to a very large number (in this case, 100,000) so that effectively these points do not contribute to the fit and allow us to determine a background shape with these bins excluded. A first fit is performed fixing the mean and width of the Gaussian representing the  $\psi(2S)$  signal to values expected from Monte Carlo, and fitting to a 3rd order polynomial plus a single Gaussian, shown in Figure 6.2. The fixed values are then allowed to float and a fit to the same function is performed again, see Figure 6.3. At this point, a good description for the background has been found, and a new function which consists of the background function and single Gaussian of the first two fits plus an extra Gaussian representing the  $X(3872)$  contribution is defined. The errors on the bins in



the  $X(3872)$  region are reset to their original values, and the initial guesses for the mean and width of the new  $X(3872)$  Gaussian are set to the mean and width of the peak described by the heavy  $\psi(2S)$  Monte Carlo. With these initial guesses, the final fit is performed, see Figure 6.4. On the sample created by the cuts defined in Section 5.3, this fitting procedure yields a mass difference measurement for the  $X(3872)$  of  $0.7647 \pm .0024 \text{ GeV}$  with  $799 \pm 134$  events in the  $X(3872)$  Gaussian. For the  $\psi(2S)$  a mass difference of  $0.5865 \pm 0.0003 \text{ GeV}$  is measured, with  $2592 \pm 81$  events in the  $\psi(2S)$  Gaussian. The difference in the measured value of the  $\psi(2S)$  mass and it's PDG value ( $0.5891 \text{ GeV}$  [18]) is used in Section 6.2.1 to set the systematic error on the  $X(3872)$  mass. The full results of the fit are shown in Table 6.1. The significance of the  $X(3872)$  peak can also be approximated through the  $\chi^2$  difference of the fit to a background function only and the fit to background plus a Gaussian  $X(3872)$ . The significance level is then approximated from the  $p$ -value where  $p = 1 - F(\Delta\chi^2; n)$ , where  $F(\Delta\chi^2; n)$  is the  $\chi^2$  probability distribution function for  $n$  additional degrees of freedom. In the fitting procedure described above,  $\Delta\chi^2 = 93.34$  and the number of additional degrees of freedom are the 3 extra fit parameters associated with the  $X(3872)$  signal Gaussian. The  $p$ -value is then  $5.42 \times 10^{-20}$ . This  $p$ -value represents the probability that the data in the region of the  $X(3872)$  mass are better described by our choice of a 3rd order polynomial background representation than the same 3rd order polynomial plus a Gaussian to represent an additional signal.

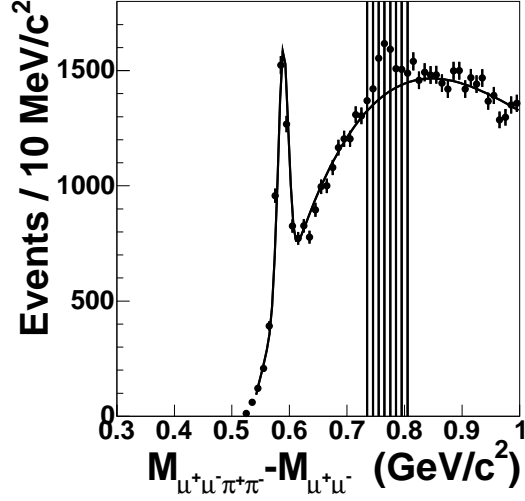


Figure 6.2: Result of fitting  $\chi^2$  fit with fixed  $\psi(2S)$  signal Gaussian, and large errors in  $X(3872)$  mass window.

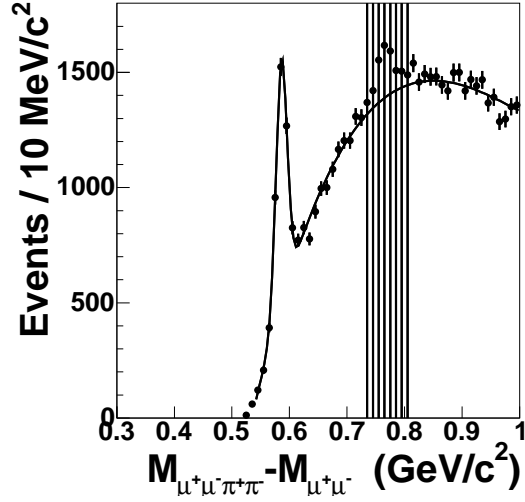


Figure 6.3: Result of fitting with  $\psi(2S)$  Gaussian released, ignoring the  $X(3872)$  mass window.

### 6.2.1 Systematic Error

The systematic error on the mass measurement of the  $X(3872)$  was determined by taking the difference between the PDG value of  $M(\psi(2S)) - M(J/\psi)$ [18] and the

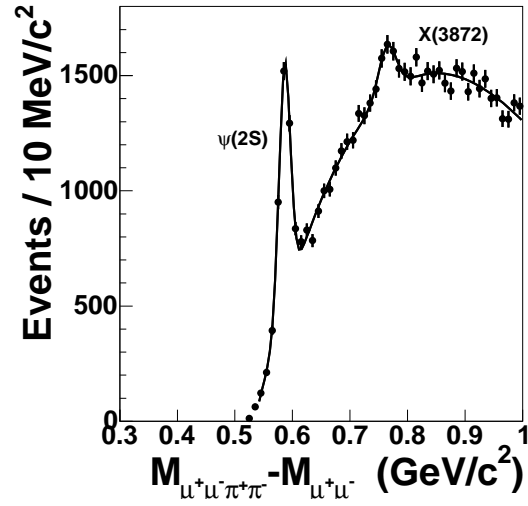


Figure 6.4: Result of final fit with Gaussian for  $X(3872)$  added.

$\psi(2S)$ norm	$1048.7 \pm 33.8$
$\psi(2S)$ mean	$0.5865 \pm 0.0003$
$\psi(2S)$ width	$0.009861 \pm 0.000307$
polynomial 0 <sup>th</sup> order	$-1.417 \times 10^4 \pm 35.7$
polynomial 1 <sup>st</sup> order	$4.581 \times 10^4 \pm 78.3$
polynomial 2 <sup>nd</sup> order	$-4.268 \times 10^4 \pm 100.2$
polynomial 3 <sup>rd</sup> order	$1.235 \times 10^4 \pm 83.7$
$X(3872)$ norm	$209.1 \pm 32.5$
$X(3872)$ mean	$0.7647 \pm 0.0024$
$X(3872)$ width	$0.01525 \pm 0.00321$

Table 6.1:  $J/\psi\pi^+\pi^-$  mass fit results with a bin width of 0.01 GeV.

DØ value of  $M(\psi(2S)) - M(J/\psi)$  and scaling by the fitted mass difference between the  $X(3872)$  and  $J/\psi$ . This scale factor is added to the fitted mass and given a 100%

error, yielding a final mass measurement of  $\Delta M = 0.7681 \pm .0024(\text{stat}) \pm .0034(\text{sys})$ .

The central value corresponds to an  $X(3872)$  mass of 3865 MeV. Other sources of systematic errors were found to be negligible.

### 6.3 Comparison to $\psi(2S)$ Charmonium State

A comparison of the  $X(3872)$  state to the charmonium state  $\psi(2S)$  was performed by selecting several production and decay variables and comparing the distribution of  $\psi(2S)$  and  $X(3872)$  with respect to these variables. Due to low statistics and the high contributions by backgrounds however, it was chosen to only utilize two bin histograms. The separation value of these two bins are chosen to be either a physically informative value or at a value in which roughly half of the total event sample lies on either side of the cut. The variables chosen for comparison, along with the value of the bin separation are:

- rapidity, with bins of  $|y| < 1$ , and  $|y| \geq 1$
- 2d distance from primary vertex to decay vertex,  $dl_{xy}$ , with bins of  $dl_{xy} \leq 0.01$ , and  $dl_{xy} > 0.01$
- $p_T$  of  $X(3872)/\psi(2S)$  candidate, with bins of  $p_T \leq 15$ , and  $p_T > 15$
- isolation,  $I$ , with bins of  $I = 1$ , and  $I < 1$
- $\cos \theta_\mu$ , with bins of  $|\cos \theta_\mu| \geq 0.4$ , and  $|\cos \theta_\mu| < 0.4$

- $\cos \theta_\pi$ , with bins of  $|\cos \theta_\pi| \geq 0.4$ ,  $|\cos \theta_\pi| < 0.4$

where isolation is defined as:

$$I = \frac{|\vec{p}_{cand}|}{\left| \vec{p}_{cand} + \sum_{conetrks} \vec{p}_{trk} \right|} \quad (6.1)$$

and the summation is over all tracks around the  $X(3872)$  candidate such that,  $\Delta R = \sqrt{\Delta\phi^2 + \Delta\eta^2} < 0.5$  with respect to the  $\eta, \phi$  direction of the  $X(3872)$  candidate. The term  $\cos \theta_\pi$  is defined by first boosting the  $X(3872)$  candidate and the pions from the  $X(3872)$  candidate into the dipion rest frame. The angle  $\theta_\pi$  is then defined to be the angle between the candidates direction and the direction of one of the pions. Likewise, for the term  $\cos \theta_\mu$  this procedure can be repeated by boosting into the dimuon rest frame and taking the angle between the candidate and one of the muons. From this angle, the helicity of the dipion and dimuon systems can be inferred. For each of these variables, the sample is split into two at the cut value, and using the same mass fitting procedure as discussed in Section 6.2. The number of  $X(3872)$  and  $\psi(2S)$  in each bin are obtained. The results are reported in Table 6.3, and plotted in figures 6.5, 6.6, 6.7, 6.8, 6.9, and 6.10. Figure 6.11 condenses these results into one plot as the fraction of the total number of  $X(3872)$  and  $\psi(2S)$  that appear in each region.

	Variable	$\psi(2S)$ yield	$X(3872)$ yield
(a)	$ y  < 1$	$1552 \pm 62$	$494 \pm 78$
	$1 <  y  < 2$	$1046 \pm 60$	$319 \pm 71$
(b)	$ \cos \theta_\mu  \geq 0.4$	$1285 \pm 56$	$349 \pm 65$
	$ \cos \theta_\mu  < 0.4$	$1306 \pm 63$	$474 \pm 81$
(c)	$ \cos \theta_\pi  \geq 0.4$	$1192 \pm 57$	$410 \pm 73$
	$ \cos \theta_\pi  < 0.4$	$1407 \pm 58$	$397 \pm 70$
(d)	$p_T > 15 \text{ GeV}$	$876 \pm 46$	$267 \pm 57$
	$p_T \leq 15 \text{ GeV}$	$1714 \pm 68$	$531 \pm 82$
(e)	$dl_{xy} \leq 0.01 \text{ cm}$	$1898 \pm 70$	$526 \pm 85$
	$dl_{xy} > 0.01 \text{ cm}$	$694 \pm 41$	$278 \pm 51$
(f)	$I = 1$	$544 \pm 30$	$156 \pm 28$
	$I < 1$	$2058 \pm 74$	$658 \pm 95$

Table 6.2: Yields of  $\psi(2S)$  and  $X(3872)$  for different ranges of variables. The fitted widths of  $\psi(2S)$  and  $X(3872)$  are not constrained in the initial selection, however over the ranges listed in these tables, the Gaussian widths for  $\psi(2S)$  and  $X(3872)$  are fixed to the values obtained in the fit over the full sample. The uncertainties in this table reflect only the uncertainty in fitted Gaussian normalization and do not reflect the small uncertainties in background

## 6.4 Lifetime Analysis

The  $X(3872)$  decays to  $J/\psi\pi^+\pi^-$  through QCD interactions, resulting in a lifetime too short to be measured with the DØ detector. Useful information can still be obtained through a lifetime analysis of the  $X(3872)$ . At the BELLE experiment,  $X(3872)$  is produced through decays of  $B$  mesons, which decay through weak interactions, and thus exhibit large and measurable lifetimes. At the Tevatron, however,

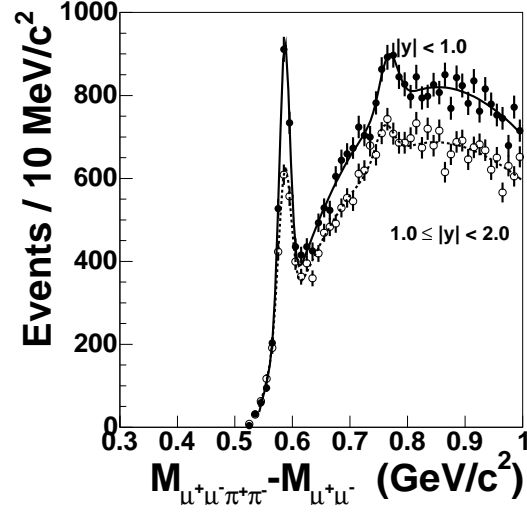


Figure 6.5:  $\Delta M$  distribution for the two ranges of rapidity in the  $\mu^+\mu^-\pi^+\pi^-$  system.

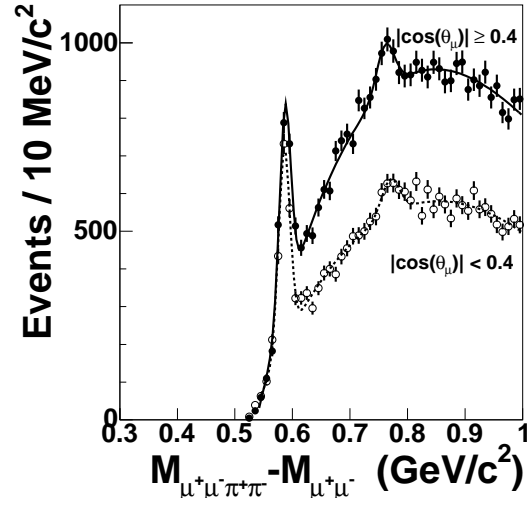


Figure 6.6:  $\Delta M$  distribution for the two ranges of  $|\cos \theta_\mu|$  in the  $\mu^+\mu^-\pi^+\pi^-$  system.

$X(3872)$  may be produced directly through  $p\bar{p}$  collisions and also through decays of  $B$  mesons. By observing the pseudo-proper time associated with the  $X(3872)$ , it is possible to determine the ratio of these two production mechanisms at the Tevatron

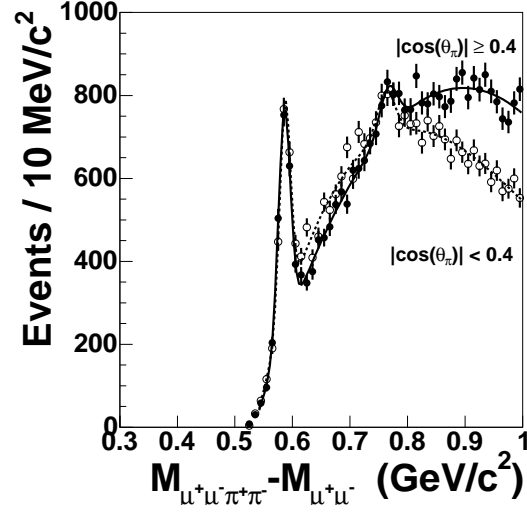


Figure 6.7:  $\Delta M$  distribution for the two ranges of  $|\cos \theta_\pi|$  in the  $\mu^+\mu^-\pi^+\pi^-$  system.

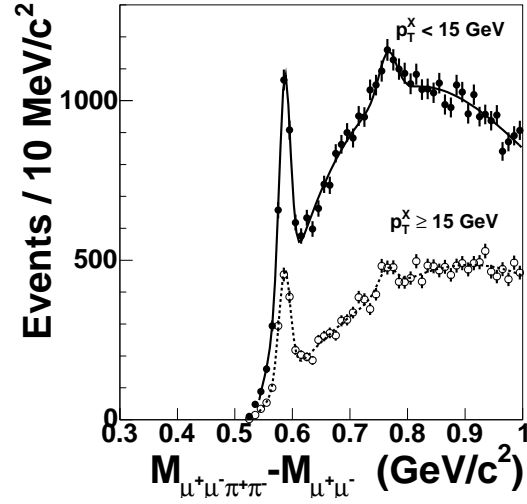


Figure 6.8:  $\Delta M$  distribution for the two ranges of  $p_T$  in the  $\mu^+\mu^-\pi^+\pi^-$  system.

without fully reconstructing the decay. In order to determine the fraction of directly produced  $X(3872)$  events, a simultaneous likelihood fit to a background and signal region is performed on the proper lifetime distribution of the  $J/\psi$  used in the analysis.



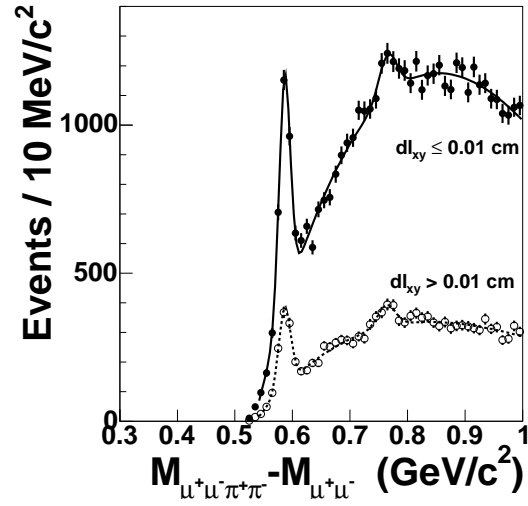


Figure 6.9:  $\Delta M$  distribution for the two ranges of  $dl_{xy}$  in the  $\mu^+\mu^-\pi^+\pi^-$  system.

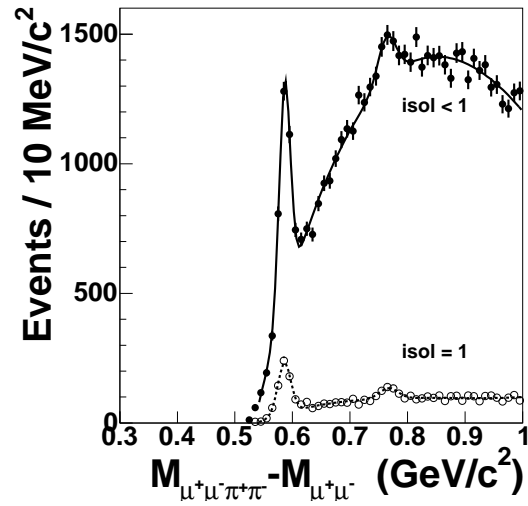


Figure 6.10:  $\Delta M$  distribution for the two ranges of isolation in the  $\mu^+\mu^-\pi^+\pi^-$  system.

The proper lifetime,  $\tau$  of any particle is defined such that:

$$c\tau = \frac{ML_{lab}}{|\vec{p}|} \quad (6.2)$$

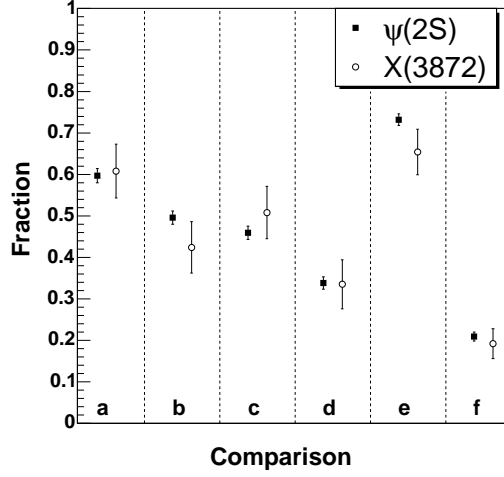


Figure 6.11: Comparison of event-yield fractions for  $X(3872)$  and  $\psi(2S)$  in the regions: (a)  $|y|$  of  $J/\psi\pi^+\pi^- < 1$ ; (b)  $\cos\theta_\mu < 0.4$ ; (c)  $\cos\theta_\pi < 0.4$ ; (d)  $p_T(J/\psi\pi^+\pi^-) > 15 \text{ GeV}/c$ ; (e) effective transverse proper decay length,  $dl_{xy} < 0.01 \text{ cm}$ ; (f) isolation  $= 1$

Where  $\tau$  represents the proper lifetime, or lifetime of a particle in its rest frame,  $M$  is the particle mass,  $\vec{p}$  is the particle's 3-momentum vector and  $L_{lab}$  is the distance traveled by the particle in the lab frame. In the case of  $X(3872)$ ,  $\psi(2S)$ ,  $J/\psi$ , and other charmonium states, the proper lifetime is so short that it is indistinguishable from zero within the DØ tracking resolution. However, due to the large lifetime of  $B$  mesons, one can extract the ratio of “prompt” production with respect to production through  $B$  decay. In order to extract this ratio, a pseudo-proper lifetime is constructed where  $L_{lab}$  is defined to be the distance from the primary vertex to the  $J/\psi$  decay vertex. Due to the poorer tracking resolution in the  $z$  direction, the pseudo-proper lifetime is only calculated in the transverse plane, so that the pseudo-proper time

becomes

$$c\tau_{xy}^{pseudo} = \frac{M_{J/\psi} dl_{xy}}{p_T^{J/\psi}}. \quad (6.3)$$

The distribution of this quantity is plotted for signal and background regions in the mass distribution, see Figures 6.12 and 6.13, and a simultaneous pseudo-proper-lifetime fit is performed over both regions.

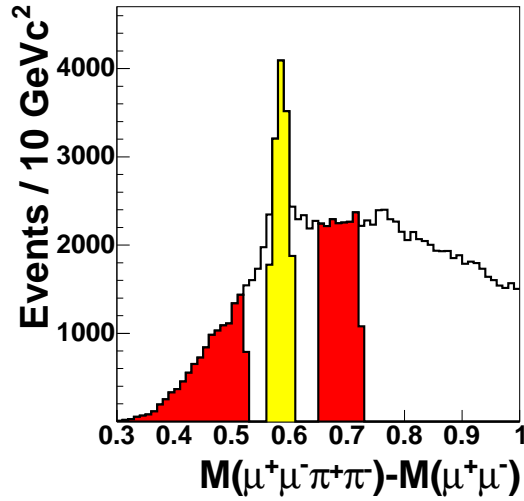


Figure 6.12: Mass regions used in the  $\psi(2S)$  lifetime fit.

The background region for this fit is taken from the sidebands of the  $X(3872)$  such that each sideband lies more than  $3\sigma$  away from the mean measured  $X(3872)$  and  $\psi(2S)$  mass, and an equal number of events are contained in each sideband. The signal region is defined as being a  $2\sigma$  region around the measured mass of the  $X(3872)$ .

Simultaneously, the background region and the signal regions are fit to a background distribution plus a signal contribution. In the background region, the signal

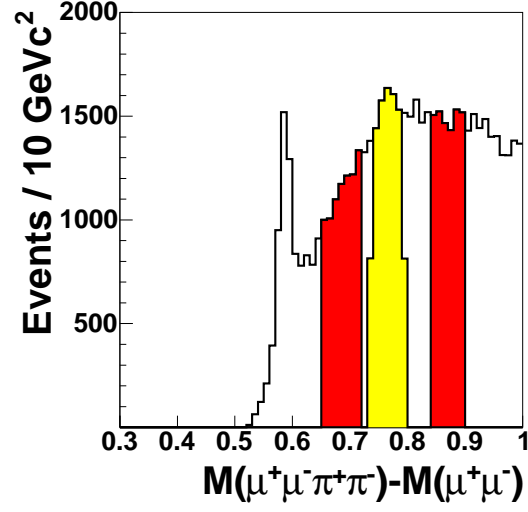


Figure 6.13: Mass regions used in the  $X(3872)$  lifetime fit.

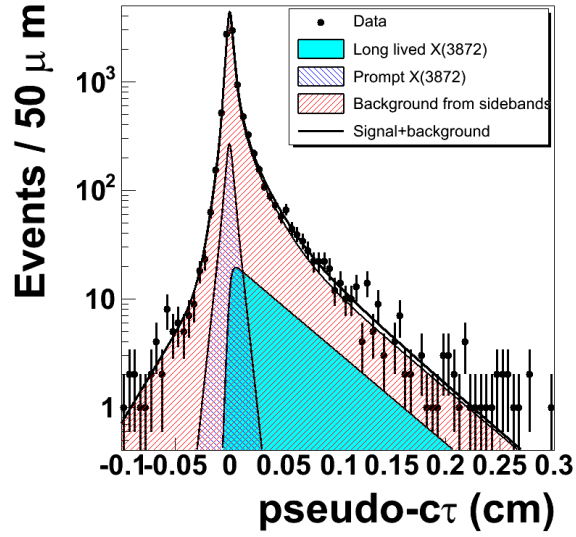


Figure 6.14: Lifetime distribution for the  $\mu^+\mu^-\pi^+\pi^-$  system in the  $X(3872)$  mass window.

contribution is set to zero. The background function consists of a double Gaussian

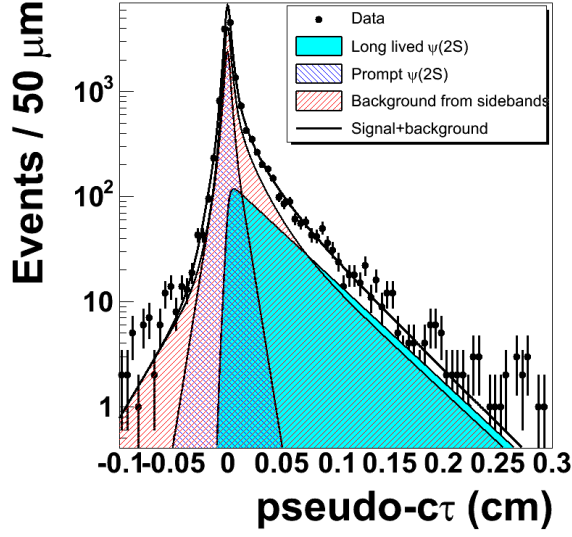


Figure 6.15: Lifetime distribution for the  $\mu^+\mu^-\pi^+\pi^-$  system in the  $\psi(2S)$  mass window.

and symmetric exponential to describe prompt background plus one negative exponential tail and two positive exponential tails. The signal function consists of a double Gaussian and symmetric exponential to describe the prompt component and a single exponential to describe the long lived component. All parameters are given initial guesses and allowed to float, except for the parameter which describes the fractional signal contribution in the signal region. This parameter is fixed based on the results given in section 6.2. The resulting fit is shown in Figure 6.14, and yields a prompt fraction of  $70.0 \pm 6.66\%$ . This fitting procedure is repeated for the  $\psi(2S)$ , utilizing the data sample without an  $M(\pi\pi)$  cut. The fit results are shown in Figure 6.15 and yield a prompt fraction of  $77.1 \pm 1.29\%$ . These prompt fractions, specifically the  $\psi(2S)$  prompt fraction will be an important part of the limit calculation in Chapter

7. Additionally, the  $\psi(2S)$  prompt fraction was measured on a sample with a tighter cut on muon nseg and  $J/\psi$  transverse momentum to reflect the muon cuts utilized in Chapter 7. The  $X(3872)$  prompt fraction further confirms that the primary mode of  $X(3872)$  production at the Tevatron occurs directly through  $p - \bar{p}$  collisions rather than through the decay of  $B$  mesons.

## 6.5 Summary of Results

In this chapter it was shown that the  $X(3872)$  is observed at DØ in the decay mode to  $J/\psi\pi^+\pi^-$  with a measured mass difference  $\Delta M = 0.7675 \pm 0.0024(\text{stat}) \pm 0.0033(\text{syst})$  GeV and  $1011 \pm 156 X(3872)$  events. Further analysis of production and decay properties showed that in the variables chosen for study, the  $X(3872)$  exhibited similar properties to the charmonium state  $\psi(2S)$ . Further angular analysis and dipion mass spectrum analysis capabilities at DØ are limited due to the large combinatoric backgrounds and the resolution capabilities of the DØ tracking. It has also been shown that production of the  $X(3872)$  at the Tevatron proceeds not only through  $B$  meson decay, as observed by the Belle and Babar collaborations, but also directly through  $p\bar{p}$  collisions. It is shown that such “prompt” production is in fact the dominant production channel, with  $70.0 \pm 6.66\%$  of events being produced in this manner. This ratio is consistent with charmonium production at DØ and could have implications on the interpretation of  $X(3872)$  as a weakly bound meson molecule.

## Chapter 7

### $X(3872) \rightarrow J/\psi\gamma$ Analysis

Because Figure 5.8 shows no obvious excess of events near the mass of the  $X(3872)$ , an upper limit for the relative branching ratio,  $R$ , is measured.

$$R = \frac{BR(X(3872) \rightarrow J/\psi\gamma)}{BR(X(3872) \rightarrow J/\psi\pi^+\pi^-)} \quad (7.1)$$

$$R = \frac{N_{X \rightarrow J/\psi\gamma}^{obs}}{N_{X \rightarrow J/\psi\pi^+\pi^-}^{obs}} \frac{\epsilon_{J/\psi\pi\pi}}{\epsilon_{J/\psi\gamma}} \quad (7.2)$$

The term  $\epsilon_{xyz}$  represents the efficiency of reconstructing  $X(3872)$  decaying to a final state  $xyz$ , and  $N_{xyz}^{obs}$  represents the number of observed candidates in decay mode  $xyz$ .

It is also assumed that all  $J/\psi$  decays to  $\mu^+\mu^-$ .

To minimize the use of Monte Carlo simulation, these efficiencies are determined using data through the convenient calibration states  $\chi_{c1,2}$  and  $\psi(2S)$  which decay

prominently to  $J/\psi\gamma$  and  $J/\psi\pi^+\pi^-$  respectively. The efficiencies can then be estimated as:

$$\epsilon_{J/\psi\pi\pi} = \frac{N_{\psi(2S)}^{obs}}{\sigma_{\psi(2S)}L} \quad (7.3)$$

$$\epsilon_{J/\psi\gamma} = \frac{N_{\chi_c}^{obs}}{\sigma_{\chi_c}L} \quad (7.4)$$

Where  $\sigma$  represents the inclusive production cross section of the particle in question and  $L$  represents the integrated luminosity of the dataset. These efficiencies as formulated include effects from detector acceptance as well. In order to estimate the relative efficiencies of these two final states from the calibration states, a measurement of the cross section times branching ratio for each of the calibration states is needed. The CDF experiment provides just such a measurement from Run I of the Tevatron[73]. This measurement however emphasizes direct production of  $\psi(2S)$  and  $\chi_c$ , which is known to account for roughly 70% of the samples seen at DØ. Thus, in order to make use of the quantities measured by CDF, a measurement of the prompt production fraction for both  $\psi(2S)$  and  $\chi_c$  is required. The relative branching fraction of interest then becomes:

$$R = \frac{N_{X \rightarrow J/\psi\gamma}^{obs}}{N_{X \rightarrow J/\psi\pi^+\pi^-}^{obs}} \frac{N_{\psi(2S)}^{obs}}{N_{\chi_c}^{obs}} \frac{\sigma_{\chi_c}^{prompt}}{\sigma_{\psi(2S)}^{prompt}} \frac{f_{\psi(2S)}^{prompt}}{f_{\chi_c}^{prompt}} \frac{\Delta\epsilon_{X \rightarrow J/\psi\pi\pi}}{\Delta\epsilon_{X \rightarrow J/\psi\gamma}}, \quad (7.5)$$

where  $f^{prompt}$  represents the measured prompt production fraction of a given particle in the sample, and the terms  $\Delta\epsilon$  are added as multiplicative factors to account for the effect of kinematic differences between the  $X(3872)$  and the calibration states in



each channel. These factors are primarily derived from the Monte Carlo simulations, and will be discussed in section 7.1.

There is no obvious sign of  $X(3872) \rightarrow J/\psi\gamma$  in the data. Thus the term in equation (7.5),  $N_{X \rightarrow J/\psi\gamma}^{obs}$  presents a problem. Rather than try to set a limit on this term and translate that number into a limit on  $R$ , equation (7.5) is instead reformulated to be the number of signal events predicted for any given value of  $R$ . Thus,

$$N_{X \rightarrow J/\psi\gamma}^{pred} = R N_{X \rightarrow J/\psi\pi\pi}^{obs} \frac{N_{\chi_c}^{obs}}{N_{\psi(2S)}^{obs}} \frac{\sigma_{\psi(2S)}^{prompt}}{\sigma_{\chi_c}^{prompt}} \frac{f_{\chi_c}^{prompt}}{f_{\psi(2S)}^{prompt}} \frac{\Delta\epsilon_{X \rightarrow J/\psi\gamma}}{\Delta\epsilon_{X \rightarrow J/\psi\pi\pi}}. \quad (7.6)$$

This prediction is then added to a background estimate in a Bayesian limit calculator[74] in order to directly set a limit on the ratio  $R$ .

## 7.1 Monte Carlo Simulation of Expected Signals

In the  $J/\psi\gamma$  decay mode, a large contribution from the  $\chi_{c1}$  and  $\chi_{c2}$  states is expected. To model the expected distribution from these states, Monte Carlo is created for the production of  $\chi_{c1}$  and  $\chi_{c2}$ . These states are then required to decay to  $J/\psi\gamma$  with the restrictions imposed that the photons are central ( $|\eta| < 1.1$ ), the photon  $p_T$  is greater than 1.5 GeV, and the  $J/\psi$  is required to decay to two muons such that each muon carries transverse momentum greater than 4.0 GeV. These requirements are imposed to ensure that the final state particles of interest are energetic enough to pass reconstruction cuts efficiently. Applying the event selection cuts of section 5.4 to the Monte Carlo samples, mass distributions shown in Figures 7.1, 7.2 are obtained.

From the Monte Carlo, it is seen that the masses of the  $\chi_c$  states are reconstructed to be approximately 50 MeV too low. This is due to the fact that the energy of each photon is taken to be the sum of the deposited energy in each calorimeter cell with no correction applied for showers that likely begin in the solenoid.

As with the previous analysis, Monte Carlo for  $X \rightarrow J/\psi\gamma$  is created as a  $\chi_{c1}$  with mass 3872 MeV. This is done to determine the expected mass window of the  $X(3872)$ . The mass distribution of the simulated  $X(3872)$  is shown in Figure 7.3.

The samples for  $\chi_{c1}$  and  $X(3872)$  are fit to distributions consisting of a Gaussian and one or two exponential tails. The  $\chi_c$  is given only one tail in the high mass region due to the fact that turn-on effects diminish the effect of a low mass tail. This fit is performed on the  $\chi_{c1}$  Monte Carlo only. For this fit, entries in Figure 7.1 above  $\Delta M = 0.8$  are excluded and assumed to be the result of simulated calorimeter noise. The results of this fit are shown in Figure 7.4. The fitted ratio of the exponential decay constant to the Gaussian width is found to be  $1.772 \pm 0.168$ , and the fitted ratio of exponential normalization to the Gaussian normalization is found to be  $0.1576 \pm 0.0302$ . In the case of the  $X(3872)$ , the particle is far enough away from the turn-on curve that the tails are expected to be symmetric. The parameters found in the  $\chi_{c1}$  fit are then used to fix the tails in the fit to the  $X(3872)$  distribution, where in this case,  $\Delta M$  values above 1.2 GeV are excluded. The result of the  $X(3872)$  Monte Carlo mass fit can be seen in figure 7.5. This fit will set the  $X(3872)$  mass window, at plus or minus  $2.5\sigma$  around the Gaussian mean later in the analysis at  $0.7034 \pm 0.2014$  GeV,

in which we should expect to find 93% of the  $X(3872)$  sample we might have.

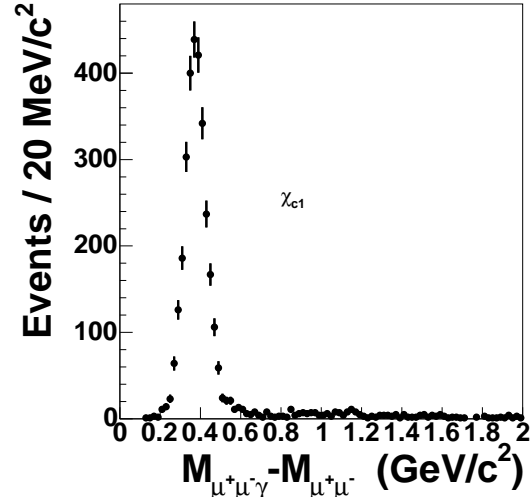


Figure 7.1:  $\chi_{c1} \rightarrow J/\psi \gamma$  Monte Carlo after applying analysis cuts.

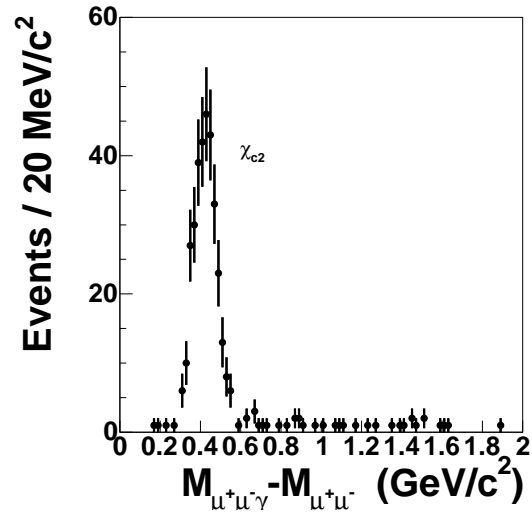


Figure 7.2:  $\chi_{c2} \rightarrow J/\psi \gamma$  Monte Carlo after applying analysis cuts

The Monte Carlo is also used to estimate the efficiency ratio of  $X(3872)$  and  $\chi_c$ . This is estimated by counting the number of events in each sample that pass the

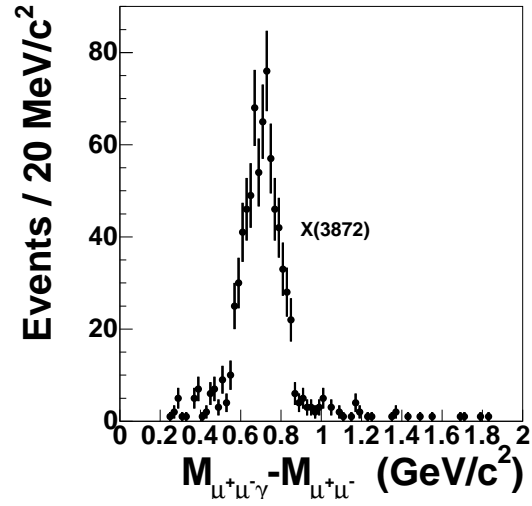


Figure 7.3: Monte Carlo simulation of  $X(3872) \rightarrow J/\psi\gamma$ , by creating  $\chi_{c1}$  particles with a mass of 3872 MeV.

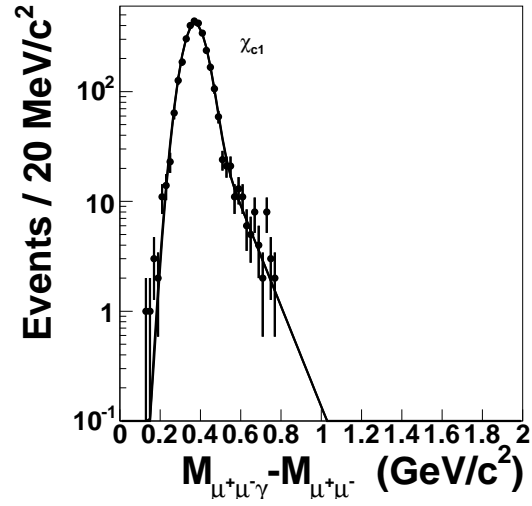


Figure 7.4:  $\chi_{c1} \rightarrow J/\psi\gamma$  fitted to a Gaussian plus an exponential tail, shown in log scale.

analysis cuts.

$$\Delta\epsilon = \frac{\frac{N_X^{pass}}{N_X^{total}}}{\frac{N_{\chi_c}^{pass}}{N_{\chi_c}^{total}}} \quad (7.7)$$

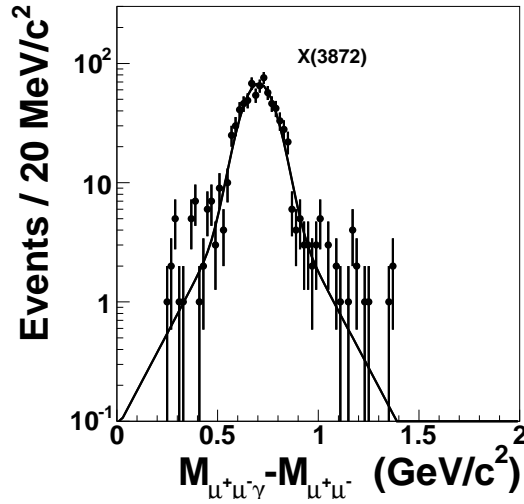


Figure 7.5:  $X(3872) \rightarrow J/\psi\gamma$  fitted to a Gaussian plus symmetric exponential tails, shown in log scale.

The samples used consisted of 31,268 simulated  $\chi_{c1}$  events and 7,419 simulated  $X(3872)$  events. The number of candidates passing analysis cuts are 3044 and 783 respectively, resulting in a  $\Delta\epsilon_{X \rightarrow J/\psi\gamma} = 1.08 \pm 0.05$ . The extra efficiency to reconstruct  $X(3872)$  is due to the fact that the photon  $p_T$  distribution for the  $X(3872)$  is skewed toward higher  $p_T$  photons than that of the  $\chi_c$  due to the extra mass of the  $X(3872)$ . Similarly, the Monte Carlo samples shown in Figure 6.1 were used to determine  $\Delta\epsilon_{X \rightarrow J/\psi\pi\pi} = 0.74 \pm 0.11$ .

## 7.2 Backgrounds

In the process of setting a limit on the relative branching fraction, the determination of expected background levels in the  $X(3872)$  mass window plays a very central

role. In an analysis where there is clear evidence for a signal peak, fitting techniques are often adequate to describe the background shape underneath the signal peak. However, in this case we are searching for what is apparently a small excess over background, and thus, it is crucial to estimate the expected background as accurately as possible.

### 7.2.1 Sources of Background

In this analysis, three sources of background are considered:

- Correlated dimuons and photons. These can take the form of fake or real  $J/\psi$ 's plus energy deposited in the calorimeter. This arises as a result of some physics process for which we get only partial reconstruction or a mis-reconstruction. This source of background is assumed to take on the same distributions as that of dimuons that fall in the  $J/\psi$  sidebands plus a photon; shown in Figure 7.6.
- Uncorrelated dimuons and photons. This primarily takes the form of a real  $J/\psi$  that gets combined with a calorimeter cluster as a result of either electronic noise, or as a result of some other physics process in the event that is independent of the process that created the  $J/\psi$ . This source of background is modeled through “event mixing”, where a  $J/\psi$  from one event is combined with a calorimeter cluster from another, randomly selected, event. The  $\Delta M$  distribution for this source is shown in Figure 7.7.

- Correlated dimuons and photons arising from  $B$  meson decays. While this can be considered a sub-set of source 1, it is considered separately due to the possibility that the sideband data incorrectly estimate the weight given to this production mechanism. This source was modeled with Monte Carlo, and it's  $\Delta M$  distribution is shown in Figure 7.8. The Monte Carlo used required the production of a  $B$  meson, which decayed into a final state of a  $J/\psi$  and either a photon or a  $\pi^0$  with transverse momentum greater than 1.5 GeV.

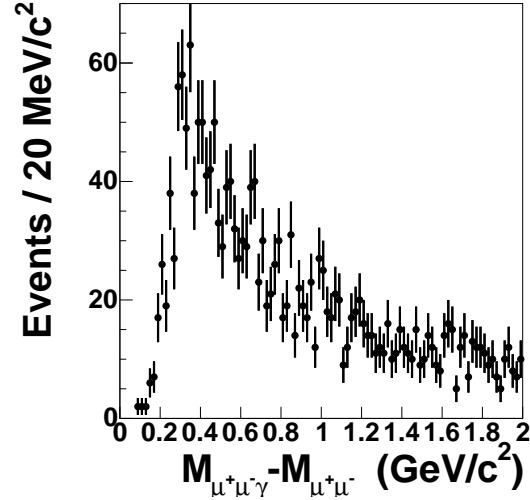


Figure 7.6:  $J/\psi$  sideband plus photon  $\Delta M$  distribution.

A first estimate for the background levels of the data sample is obtained by fixing the normalization of the sideband distribution to the level indicated in the  $J/\psi$  mass plot ( 15% of total). After fixing this background component, the other two components are fit to the data distribution in the region of  $1 \text{ GeV} < \Delta M \leq 2 \text{ GeV}$ . A second estimate can also be obtained by releasing the fixed sideband level and

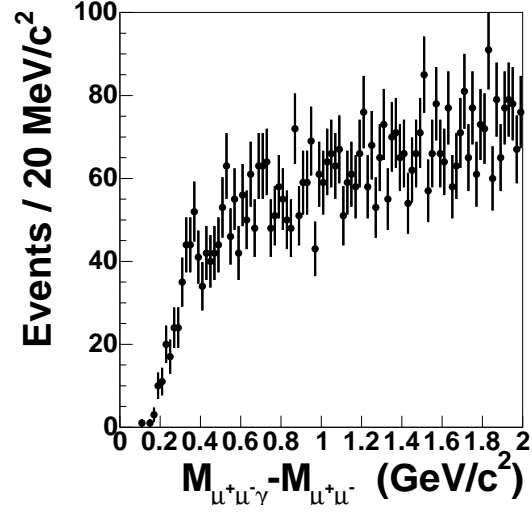


Figure 7.7:  $J/\psi$  plus “Event mixed” photon  $\Delta M$  distribution.

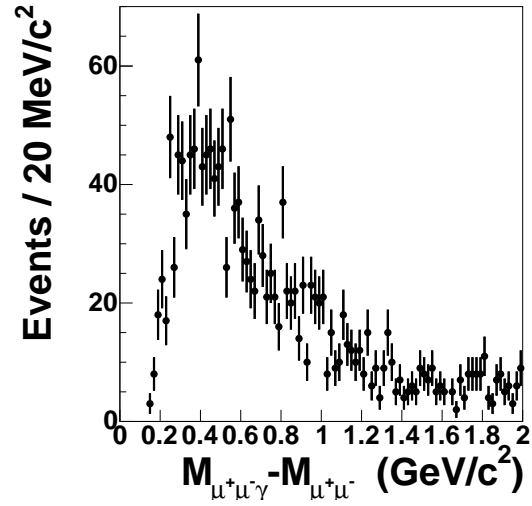


Figure 7.8:  $J/\psi$  plus photon from B decay Monte Carlo  $\Delta M$  distribution.

allowing all 3 components to float. The results of these two fitting procedures are summarized in Table 7.2.1, and shown in Figures 7.9 and 7.10. As can be seen, these results are not consistent with each other, and it is clear that a better determination of



the contribution to background from these three sources is necessary. This dilemma is solved by performing a fit with more information. In section 7.3, the mass fit is combined with a fit to pseudo-proper time information. This is made possible due to the fact that it is possible to determine the pseudo-proper time distributions for each of the background components.

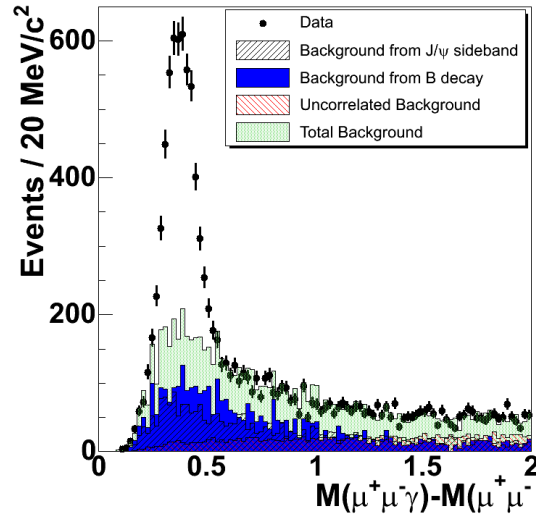


Figure 7.9: Fit to  $J/\psi\gamma$  mass distribution with fixed sideband contribution. The  $\chi_c$  and  $X(3872)$  components are left out of the plot.

### 7.3 Lifetime Analysis

Due to the fact that the best estimates available for  $\chi_c$  and  $\psi(2S)$  production cross sections only discuss direct production of these states, it is necessary then to determine what fraction of the  $\chi_c$  and  $\psi(2S)$  were produced directly from  $p\bar{p}$  collisions

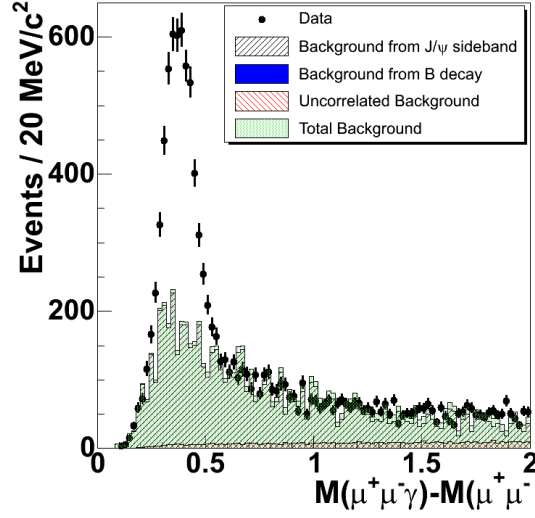


Figure 7.10: Fit to  $J/\psi\gamma$  mass distribution with floating sideband contribution. The  $\chi_c$  and  $X(3872)$  components are left out of the plot.

as opposed to the decay of  $B$  mesons. For both the  $\psi(2S)$  and  $\chi_c$  samples, the method followed for the determination of prompt fractions is much like the procedure outlined in section 6.4. However, in the case of the  $\chi_c$  fit, there is one major deviation. Simultaneous to the lifetime fitting of the  $J/\psi\gamma$  sample, a mass fit is also included. This allows for a more precise estimation of the contributions of each background source due to the fact that it can be reasonably assumed that each source of background carries a known lifetime distribution. It is assumed that the  $J/\psi$  sideband-modeled source exhibits a lifetime distribution equivalent to that of just the  $J/\psi$  background (sideband). It is also assumed that the uncorrelated background should exhibit a lifetime distribution equivalent to that of the entire  $J/\psi$  (signal and background) sample. Further, it is assumed that the  $B$  decay contribution has a lifetime distribution of

Fixed Sideband Contribution		
Component	Normalization (events)	Norm Error (events)
$\chi_{c1}(\text{MC})$	3571	212
$\chi_{c2}(\text{MC})$	518	201
X(3872)(3872)(MC)	0	$5 \times 10^{-5}$
$B$ decay (MC)	3502	278
Uncorrelated	1673	153
Sideband	2074	0
Floating Sideband Contribution		
$\chi_{c1}(\text{MC})$	2996	254
$\chi_{c2}(\text{MC})$	846	237
X(3872)(3872)(MC)	0	$1 \times 10^{-5}$
$B$ decay (MC)	0	$8 \times 10^{-4}$
Uncorrelated	672	285
Sideband	7036	479

Table 7.1: Results of separate methods of mass fitting. Due to the similarity of the  $B$  decay and sideband contributions, mass fit results are unstable.

a simple decaying exponential (convoluted with a resolution double Gaussian). To obtain these distributions, a sample of  $J/\psi$ 's are obtained and processed through the lifetime fitting procedure discussed in Section 6.4, the results of which will be used in the simultaneous mass and lifetime fit on the  $J/\psi\gamma$  sample. In order to make the  $J/\psi$  sample as consistent with the  $J/\psi\gamma$  sample, it is noted that the requirement of central calorimeter clusters imposes an implicit  $\eta$  cut on the  $J/\psi$  candidates of the

$J/\psi\gamma$  sample. To account for this effect, and the effect it has on lifetime resolution, the contribution of each  $J/\psi$  in the  $J/\psi$  sample is weighted with respect to  $\eta$ . The eta distributions of the  $J/\psi\gamma$  sample and the  $J/\psi$  sample are shown in Figures 7.12 and 7.11 respectively. The weighting distribution is shown in Figure 7.13, and the results of the lifetime fit is shown in Figure 7.14.

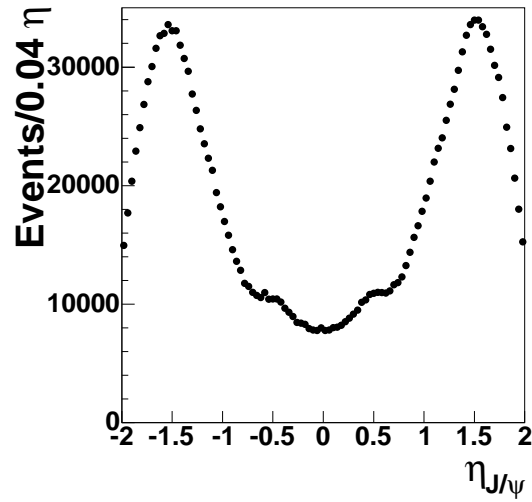


Figure 7.11:  $\eta$  distribution of all  $J/\psi$  candidates.

### 7.3.1 Simultaneous Mass and Lifetime Fitting

The estimation of the  $\chi_c$  prompt fraction is performed simultaneously to an estimation of the net contribution of each background source. This is made possible due to our ability to determine the pseudo-proper time distribution for each background component as mentioned above. A maximum log likelihood fit is performed similar to that of section 6.4. In this case, the likelihood function is expanded to

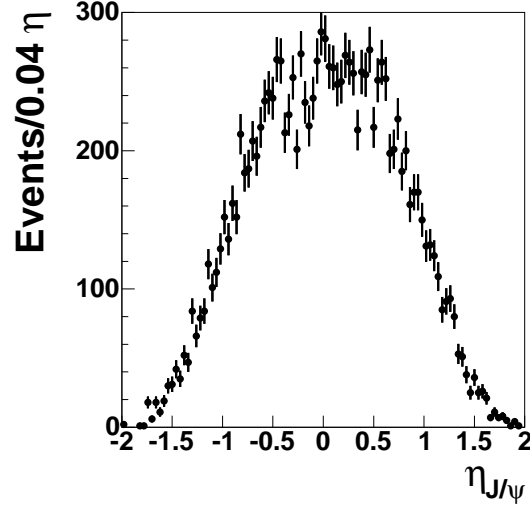


Figure 7.12:  $\eta$  distribution of  $J/\psi$  candidates in  $J/\psi\gamma$  sample.

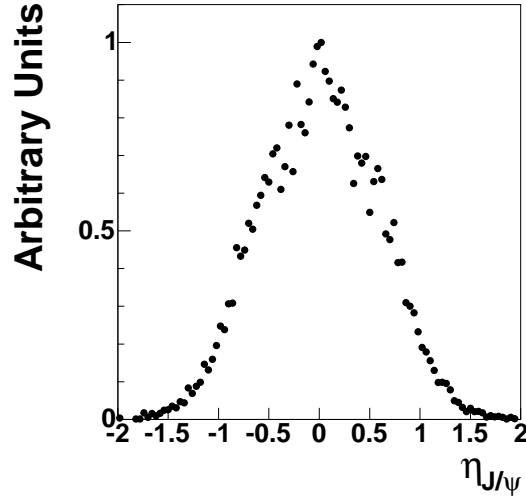


Figure 7.13: weight, as a function of  $\eta$  applied to  $J/\psi$  candidates for lifetime fitting.

include the mass distribution in data and the mass distribution of each background component. The data are separated into two subsets for fitting, one subset extending from  $0.9 < \Delta M \leq 2.0$ , and one subset from  $0 < \Delta M \leq 0.48$ . These ranges are

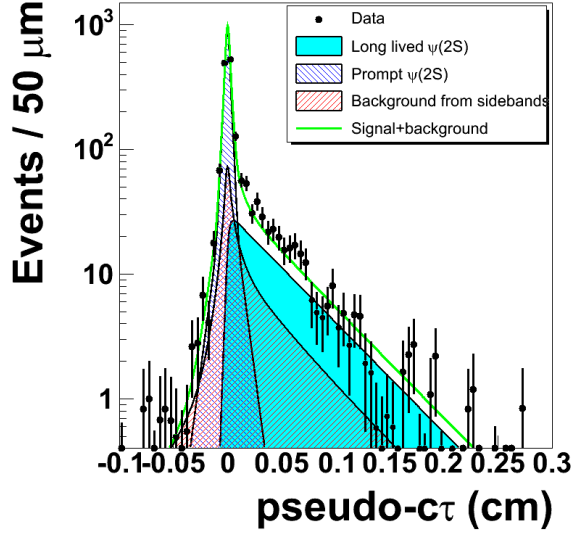


Figure 7.14: Result of lifetime fit on  $J/\psi$  sample.

chosen to stay well away from the  $X(3872)$  mass window in the fit. Each data point,  $(\Delta M, c\tau_{pseudo})$ , is assigned a likelihood if its  $\Delta M$  falls into one of the two ranges such that:

$$L = \begin{cases} \sum_{i=b,s,u} f_i^{bkg} (l_i(c\tau) + m_i(\Delta M)) & 0.9 < \Delta M \leq 2.0 \\ f_{\chi}^{sig} \times l_{\chi}(c\tau) + (1.0 - f_{\chi}^{sig}) \times \left( \sum_{i=b,s,u} f_b^{sig} \times l_b(c\tau) \right) & 0 < \Delta M \leq 0.48 \end{cases} \quad (7.8)$$

In the above likelihood function, The functions  $l_i(c\tau)$  represent the pseudo-proper time distribution attributed to the  $i$ th background component, where  $b$  represents background from  $B$  meson decay,  $s$  represents the component described by the  $J/\psi$  sideband, and  $u$  represents the uncorrelated background described through event mixing. The functions  $m_i(\Delta M)$  represent the mass distributions of each background

component in the background region, taken from Figures 7.8, 7.6, and 7.7. To ensure that each  $m_i$  is given equal weight, all  $m_i$  are normalized to 1 in the background region. The terms  $f_i^{bkg}$  represent the fraction of background described by each background component. It should be noted that  $f_u^{bkg} = 1.0 - f_s^{bkg} - f_b^{bkg}$ , and is thus not included in the fit. The terms  $f_i^{sig}$  represent these same fractions in the  $\chi_c$  signal region, which are directly related to the  $f_i$  terms in the background region by

$$f_i^{sig} = \frac{f_i^{bkg} N^{bkg} \frac{\sum_{\Delta M=0}^{0.48} m_i(\Delta M)}{2.0}}{\sum_{i=b,s,u} f_i^{bkg} N^{bkg} \frac{\sum_{\Delta M=0}^{0.48} m_i(\Delta M)}{2.0}}. \quad (7.9)$$

The fraction of  $\chi_c$  in the signal region is then

$$f_\chi = 1 - \frac{\sum_{i=b,s,u} f_i^{bkg} N^{bkg} \sum_{\Delta M=0}^{0.48} m_i(\Delta M)}{N^{sig}} \quad (7.10)$$

where  $N^{bkg}$  and  $N^{sig}$  are the number of events in the background and signal regions respectively. The background lifetime functions in the likelihood,  $l_i$  are all known and their parameters are fixed to their known values obtained from the  $J/\psi$  lifetime fit. For the functions  $f_s$  and  $f_u$ , these are fixed to the  $J/\psi$  sideband distribution and the total (signal + background) lifetime distribution in the  $J/\psi$  mass

window respectively. The function  $f_\chi$  is parameterized in the same way as the  $J/\psi$  signal function described above; a long lived decaying exponential, and a prompt double Gaussian with symmetric exponential tails. These parameter describing these signal components are allowed to float along with their respective normalizations. After defining the likelihood, the MINUIT fitting software is again called to minimize  $-\log L$ . The results of this minimization are shown in Table 7.2, and in Figures 7.15 and 7.16. Most importantly, from this fit, one is able to extract the  $\chi_c$  prompt fraction, and the total number of  $\chi_c$ . By examining the mass distribution with the fitted background components and the data minus fit plot, Figures 7.17, 7.18, one can see that there are no obvious excesses in the  $X(3872)$  signal region. A fit to the  $\chi_c$  peak to a Gaussian plus an exponential tail, where the ratio of the tail length to Gaussian width is fixed in Monte Carlo, and extract the total number of  $\chi_c$ s in the data sample.

## 7.4 Limit on the ratio $\frac{BR(X(3872) \rightarrow J/\psi\gamma)}{BR(X(3872) \rightarrow J/\psi\pi^+\pi^-)}$

The limit on  $\frac{BR(X(3872) \rightarrow J/\psi\gamma)}{BR(X(3872) \rightarrow J/\psi\pi^+\pi^-)}$  is set through the DØ standard method which utilizes Bayes' theorem. Bayes' theorem states that

$$p(\sigma, \lambda | \mathbf{n}) = \frac{\mathbf{p}(\mathbf{n} | \sigma, \lambda) \pi(\sigma, \lambda)}{\int \int \mathbf{p}(\mathbf{n} | \sigma, \lambda) \pi(\sigma, \lambda) d\lambda d\sigma}, \quad (7.11)$$

where  $\sigma$  is the *parameter of interest*, which in this case is the relative branching fraction. All other parameters are represented above by  $\lambda$  and are known as *nuisance*



$f_b^{bkg}$	$0.034 \pm 0.024$
$f_s^{bkg}$	$0.529 \pm 0.060$
$f_{\chi_c}^{prompt}$	$0.832 \pm 0.018$
$\chi_c$ long-lived slope	$0.0516 \pm 0.0038$ cm
fraction of prompt $\chi_c$ in exponential tail	$0.101 \pm 0.027$
slope of prompt $\chi_c$ tail	$0.00827 \pm 0.00147$ cm
Total Number of $\chi_c$	$4431 \pm 163$ events

Table 7.2: Results of  $J/\psi\gamma$  simultaneous mass and lifetime fit. Note that widths of prompt double Gaussian were fixed from the  $J/\psi$  lifetime fit, as were their relative normalizations.

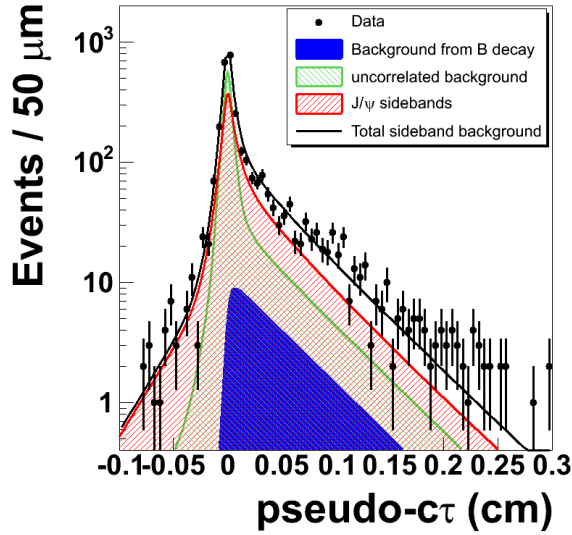


Figure 7.15: Lifetime fitting results on the  $J/\psi\gamma$  sideband.

parameters. The function  $\mathbf{p}(\mathbf{x}|\sigma, \lambda)$  is known as the *model density*, which represents the expected probability of observing  $\mathbf{n}$  events given the values of the parameters  $\sigma, \lambda$ . As this is a counting experiment, This probability density is taken to be a Poisson

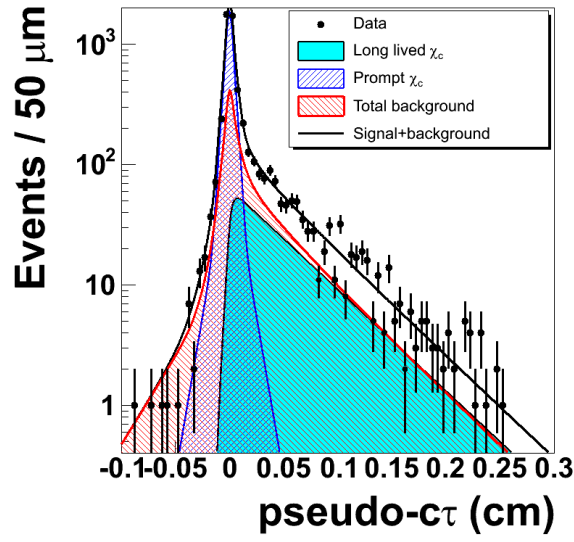


Figure 7.16: Lifetime fitting results in the  $\chi_c$  signal region.

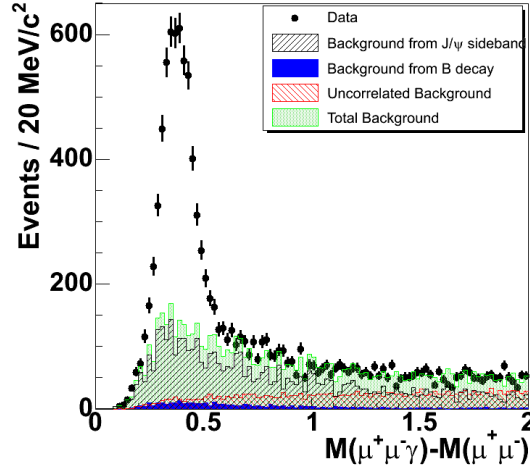


Figure 7.17:  $J/\psi\gamma$  mass distribution with the contribution from each background component overlaid as determined by simultaneous mass/lifetime fit.

distribution,

$$p(n|\sigma, \lambda) = \text{Poisson}(n, a\sigma + b). \quad (7.12)$$

where  $\mathbf{a}$  represents number of expected events in the  $X(3872)$  mass window for

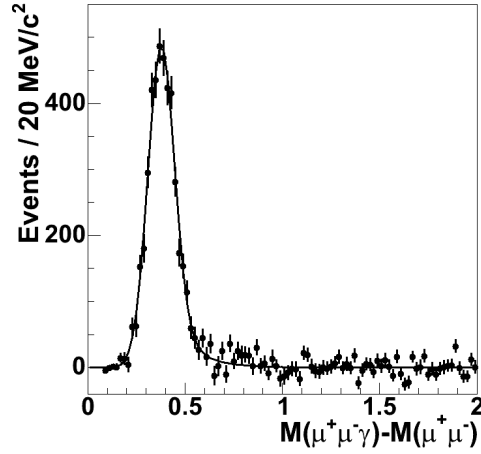


Figure 7.18:  $J/\psi\gamma$  mass distribution with background components subtracted and fit to a Gaussian with an exponential tail.

a relative branching fraction of 1, and  $\mathbf{b}$  represents the expected background in the mass window. The *prior density*,  $\pi(\sigma, \lambda)$ , can be factorized

$$\pi(\sigma, \lambda) = \pi(\lambda|\sigma)\pi(\sigma), \quad (7.13)$$

into a prior that involves only the parameter of interest and one that involves the nuisance parameters conditional on the value of the parameter of interest. In our case, we assume that the nuisance parameters are independent of the parameter of interest, and thus  $\pi(\lambda|\sigma) = \pi(\lambda)$ . The prior  $\pi(\lambda)$  is modeled as a multivariate Gaussian with a known mean and covariance matrix obtained from estimates of these parameters. The prior  $\pi(\sigma)$  is taken to be a flat prior over an interval of likely values. The posterior density  $p(\sigma, \lambda|\mathbf{n})$  is then integrated of the nuisance parameters to obtain the final

posterior probability density  $p(\sigma|\mathbf{n})$ . The upper limit,  $\sigma^u$  is found through:

$$CL = \int_0^{\sigma^u} p(\sigma|\mathbf{n}) d\sigma \quad (7.14)$$

where  $CL$  is the desired confidence level, which in this case is set at 90%.

### 7.4.1 Bayesian Limit Calculation

To set a limit on the relative branching fraction  $\frac{BR(X(3872) \rightarrow J/\psi\gamma)}{BR(X(3872) \rightarrow J/\psi\pi^+\pi^-)}$ , the data from Figure 5.8 are plotted over an interval given by the fitted, expected  $X(3872)$  mass window given in section 7.1, as shown in figure 7.19. In addition to this, the results of the simultaneous lifetime and mass fit are used to scale the distributions for each background component, see Figures 7.6, 7.7, 7.8 to the nominal contribution from each background component. These are also plotted in the same mass window, see Figures 7.20, 7.21, 7.22. Because there is also some contribution from the  $\chi_c$  tails in this mass window, a plot of the expected  $\chi_c$  distribution in this mass window is also created, using the results of the simultaneous mass and lifetime fit to set the normalization, see Figure 7.23. This histogram is drawn based upon the fitted MC distribution. A histogram for the expected  $X(3872)$  mass distribution is also drawn for this mass window, see Figure 7.24, based entirely upon the fit given in Figure 7.5, and normalized to 0.93, the fraction of the fitted  $X(3872)$  Monte Carlo mass distribution that falls within this window. These histograms are used by a Bayesian limit calculator to arrive at an upper limit on the relative branching ratio

$\frac{BR(X(3872) \rightarrow J/\psi\gamma)}{BR(X(3872) \rightarrow J/\psi\pi^+\pi^-)}$ . In the Bayesian limit calculation, the model distribution is set

to

$$\mathbf{p}(\mathbf{n}|\sigma, \lambda) = \mathbf{Poisson}\left(\mathbf{n}, N_{X(3872) \rightarrow J/\psi\gamma}^{pred|R=1} R + \sum_i \mathbf{b}_i\right) \quad (7.15)$$

where  $N_{X(3872) \rightarrow J/\psi\gamma}^{pred|R=1}$  is taken from equation 7.6 with  $R$  set to 1 which is repeated below in equation 7.16, and the terms of which are given in table 7.3

$$N_{X \rightarrow J/\psi\gamma}^{pred|R=1} = N_{X \rightarrow J/\psi\pi\pi}^{obs} \frac{N_{\chi_c}^{obs}}{N_{\psi(2S)}^{obs}} \frac{\sigma_{\psi(2S)}^{prompt}}{\sigma_{\chi_c}^{prompt}} \frac{f_{\chi_c}^{prompt}}{f_{\psi(2S)}^{prompt}} \frac{\Delta\epsilon_{X \rightarrow J/\psi\gamma}}{\Delta\epsilon_{X \rightarrow J/\psi\pi\pi}}. \quad (7.16)$$

The terms  $\mathbf{b}_i$  represent the predicted background in each background channel, side-band, uncorrelated,  $B$  decay, and spill over from the  $\chi_c$ . These background estimations are taken from Figures 7.20, 7.21, 7.22, and 7.23. This model distribution is taken bin by bin. The prior distribution  $\pi(\lambda)$  is set to the fitted  $X(3872) \rightarrow J/\psi\gamma$  mass distribution obtained from Monte Carlo, as shown in Figure 7.24. The nuisance variables in this case are the mass and  $N_{X(3872) \rightarrow J/\psi\gamma}^{pred|R=1}$  and the  $\mathbf{b}_i$  background coefficients which are modeled through a multivariate Gaussian with means  $m_i$  and covariance matrix  $\Sigma$  taken from the simultaneous mass and lifetime fitting. The prior  $\pi(R)$  is taken as a flat prior.

The posterior probability distribution obtained from this calculation is shown in figure 7.25, and the 90%  $CL$  upper limit is found to be at  $R < 1.5$ .

Term	Value
$N_{X \rightarrow J/\psi \pi \pi}^{obs}$	$613 \pm 110$
$N_{\chi_c}^{obs}$	$4430 \pm 163$
$N_{\psi(2S)}^{obs}$	$5738 \pm 156$
$\frac{\sigma_{\psi(2S)}^{prompt}}{\sigma_{\chi_c}^{prompt}}$	$0.17 \pm 0.026 [73]$
$f_{\chi_c}^{prompt}$	$0.832 \pm 0.018$
$f_{\psi(2S)}^{prompt}$	$0.771 \pm 0.013$
$\Delta\epsilon_{X \rightarrow J/\psi \gamma}$	$1.08 \pm 0.05$
$\Delta\epsilon_{X \rightarrow J/\psi \pi \pi}$	$0.74 \pm 0.11$

Table 7.3: Values of parameters used to determine  $N_{X \rightarrow J/\psi \gamma}^{pred|R=1}$ . The terms  $N_{X \rightarrow J/\psi \pi \pi}^{obs}$ ,  $N_{\psi(2S)}^{obs}$  are determined by imposing additional cuts on the muons of sample used in Chapter 6. Those cuts are  $nseg > 1$  for each muon, and  $p_T(J/\psi) > 7$  GeV and applying the same fitting procedure as in section 6.2

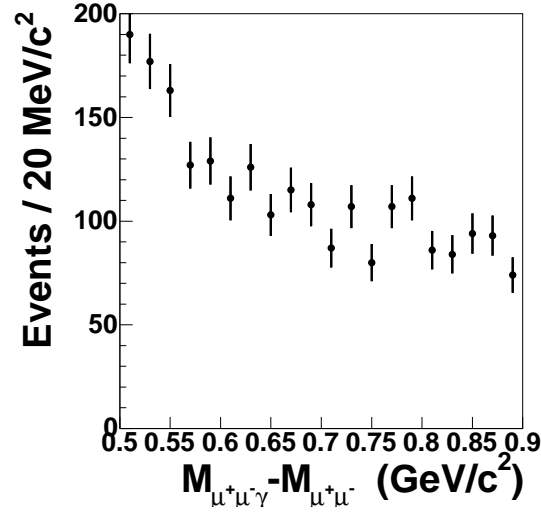


Figure 7.19: data in expected  $X(3872)$  mass window.

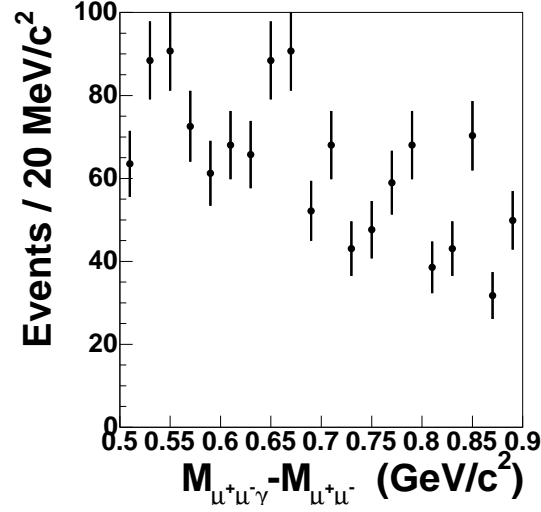


Figure 7.20:  $J/\psi$  sideband background contribution in expected  $X(3872)$  mass window.

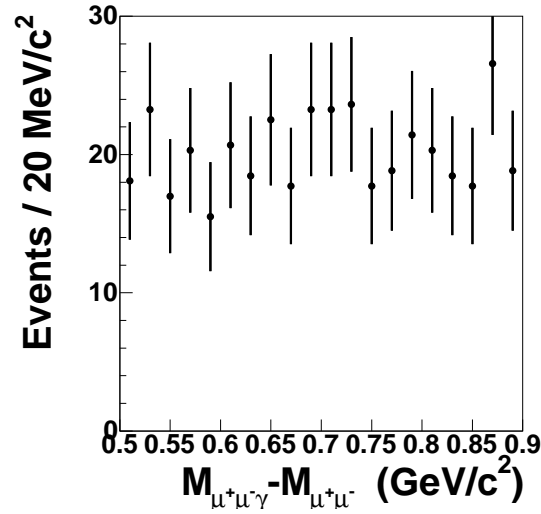


Figure 7.21: Uncorrelated background contribution in expected  $X(3872)$  mass window.

## 7.5 Summary of Results

In this chapter it has been shown that  $J/\psi\gamma$  is not a dominant decay channel of the  $X(3872)$  as is naively expected for the  $2^3P_{1++}$  charmonium model based on

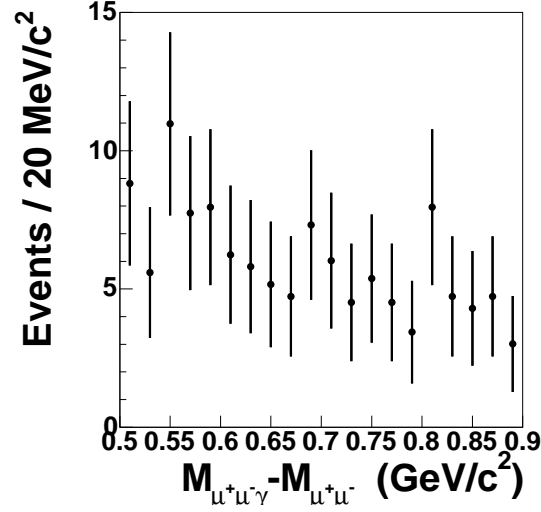


Figure 7.22:  $B$  meson decay background contribution in expected  $X(3872)$  mass window.

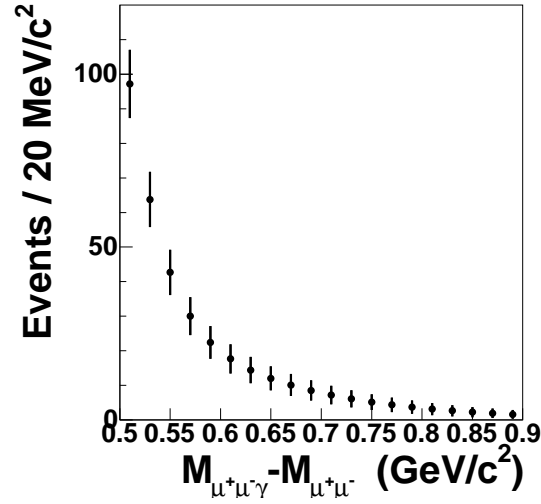


Figure 7.23:  $\chi_c$  contribution in expected  $X(3872)$  mass window.

isospin arguments. At 90% CL, the ratio of branching fractions of this decay channel with respect to the discovery decay channel to  $J/\psi\pi^+\pi^-$  is less than 1.5. This is in agreement with evidence for the discovery of this decay channel at both Belle and



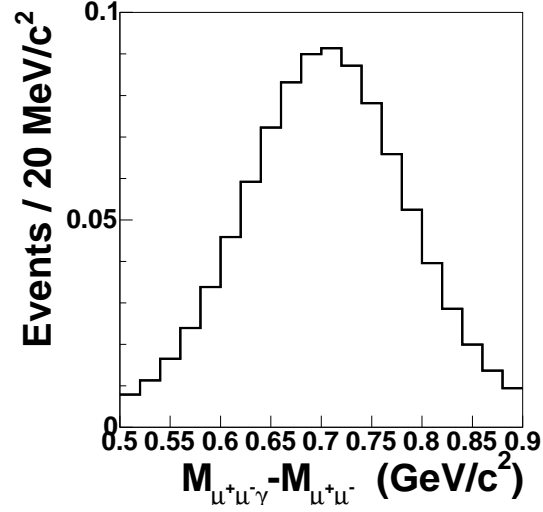


Figure 7.24:  $X(3872)$  mass distribution expected  $X(3872)$  mass window.

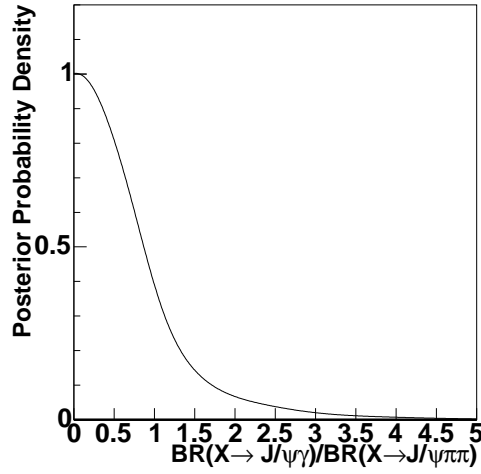


Figure 7.25: Posterior probability density.

Babar. Belle observes a  $4\sigma$   $X(3872)$  peak in this decay channel resulting in a relative branching fraction of  $0.15 \pm 0.5$ , while Babar measures this ratio to be 0.24 with a significance of  $3.4\sigma$ . If the evidence for this decay channel at Belle and Babar stand,

this will definitively measure the  $C$  parity of the  $X(3872)$  to be positive, as well as confirm that the discovery decay channel is in fact an isospin violating decay channel. In light of some recent studies however, this does not seem to settle the question of whether the  $X(3872)$  should be interpreted as a conventional charmonium state or a meson molecule, as it has been shown that it is possible for conventional  $2^3P_{1++}$  charmonium to both violate isospin and have a small rate to  $J/\psi\gamma$ . Both of these effects are also features of the meson molecule interpretation as well.

## Chapter 8

### Summary of Results

Since the  $X(3872)$  was discovered by the Belle Collaboration in August 2003, its interpretation through the Standard Model has been difficult. Many possible interpretations have been proposed due to its close proximity to the  $D\overline{D}^*$  mass threshold, ranging from a new state in the charmonium spectrum to a 4-quark state to a weakly bound meson molecule. Probing the  $X(3872)$  is also made difficult due to low statistical samples at  $e^+e^-$  colliders and large combinatoric backgrounds at hadron colliders such as the Tevatron. This paper presented the results of probes of this state performed at the DØ detector.

#### 8.1 Observation of $X(3872)$

In Chapter 6 it was shown that the  $X(3872)$  is present in the data sample collected at DØ and its mass is measured to be  $0.7861 \pm 0.0024(\text{stat}) \pm 0.0034(\text{sys.})$  GeV

greater than the mass of the well known  $J/\psi$  charmonium state. It is also shown that the  $X(3872)$  behaves similarly to the charmonium state  $\psi(2S)$  with respect to several production and decay properties. It is also shown that  $X(3872)$  production at the Tevatron is dominated through direct  $p\bar{p}$  interactions, rather than through  $B$  meson decay, similar to known charmonium states. A prompt fraction of  $70.0 \pm 6.66\%$  is measured for the  $X(3872)$ .

## 8.2 Search for $X(3872)$ Decaying to $J/\psi\gamma$

In Chapter 7 a search for  $X(3872)$  decaying to  $J/\psi\gamma$  was performed. This search did not reveal evidence of  $X(3872)$  decaying to this channel. A 90% CL limit on the relative branching fraction to this channel was set at 1.5. This result would seem to indicate that the  $X(3872)$  cannot be a candidate for the  $\chi_{c1}(2P)$  charmonium state due to isospin arguments. Recent calculations have thrown these arguments into doubt however, and seem to imply that this charmonium level would not have to be dominated by  $J/\psi\gamma$  decays if its mass is at 3872 MeV. Therefore this state cannot yet be ruled out.

## Bibliography

- [1] Belle, A. Abashain *et al.*, Nucl. Instrum. Meth. **A479**, 117 (2002).
- [2] S.-K. Choi *et al.*, Phys. Rev. Lett. **91**, 262001 (2003).
- [3] K. Abe, Properties of the X(3872) at Belle, 2004, hep-ex/0408116.
- [4] Belle, R. Chistov, Phys. Rev. Lett. **93**, 051803 (2004).
- [5] G. Gokhroo and G. Majumder, Phys. Rev. Lett. **97**, 162002 (2006).
- [6] BaBar, B. Aubert *et al.*, Nucl. Instrum. Meth. **A479**, 1 (2002), hep-ex/0105044.
- [7] BaBar, B. Aubert *et al.*, Phys. Rev. Lett. **93**, 041801 (2004).
- [8] BaBar, B. Aubert *et al.*, Search for an X(3872) charged partner in the decay mode  $X \rightarrow J/\psi \pi^- \pi^0$  in the  $B$  meson decays  $B^0 \rightarrow X^- K^+$  and  $B \rightarrow X^- K_s$ , 2004, hep-ex/0408083.
- [9] BaBar, B. Aubert *et al.*, Phys. Rev. D **71**, 031501 (2005).
- [10] BES Collaboration: J. Z. Bai *et al.*, Nucl. Instrum. Meth. **A458**, 627 (2001).
- [11] CLEO, S. E. Kopp, Nucl. Instrum. Meth. **A384**, 61 (1996).
- [12] C. Z. Yuan, X. H. Mo, and P. Wang, Phys. Lett. B **579**, 74 (2004).
- [13] CLEO, S. Dobbs, Phys. Rev. Lett. **94**, 032004 (2005).
- [14] K. Abe, Experimental constraints on the possible  $J^{PC}$  quantum numbers of the X(3872), 2005, hep-ex/0505038.
- [15] CDF, D. Acosta *et al.*, Phys. Rev. **D71**, 032001 (2005), hep-ex/0412071.
- [16] CDF, A. Abulencia *et al.*, Phys. Rev. Lett. **96**, 102002 (2006).
- [17] CDF Collaboration, Analysis of the quantum numbers  $J^{PC}$  of the X(3872), 2006, hep-ex/0612053.

- [18] S. Eidelman *et al.*, Phys. Lett. B **592**, 1+ (2004).
- [19] C. Meng and K.-T. Chao, Decays of the  $X(3872)$  and  $\chi_{c1}(2P)$  charmonium, 2007, hep-ph/0703205.
- [20] Y. S. Kalashnikova, Phys. Rev. Lett. **72**, 034010 (2005), hep-ph/0506270.
- [21] C. Quigg, The Lost Tribes of Charmonium, 2004, hep-ph/0407124.
- [22] G. Wagner and for the BABAR Collaboration, Recent results on two-photon and tau physics at BABAR, 2003, hep-ex/0305083.
- [23] BaBar, B. Aubert *et al.*, Phys. Rev. Lett. **92**, 142002 (2004), hep-ex/0311038.
- [24] T. Barnes and S. Godfrey, Phys. Rev. D **69**, 054008 (2004).
- [25] S. Pakvasa and M. Suzuki, Phys. Lett. B **579**, 67 (2004).
- [26] E. Eichten, K. Gottfried, T. Kinoshita, K. D. Lane, and T. M. Yan, Phys. Rev. D **21**, 203 (1980).
- [27] E. J. Eichten, K. Lane, and C. Quigg, Phys. Rev. D **69**, 094019 (2004).
- [28] CDF, D. Acosta *et al.*, Phys. Rev. Lett. **93**, 072001 (2004).
- [29] DØ, V. M. Abazov *et al.*, Phys. Rev. Lett. **93**, 162002 (2004).
- [30] BaBar, B. Aubert *et al.*, Phys. Rev. D **71**, 071103 (2005).
- [31] CLEO, C. Cawlfeld *et al.*, Phys. Rev. Lett. **98**, 092002 (2007).
- [32] N. A. Tornqvist, Z. Phys. **C61**, 525 (1994), hep-ph/9310247.
- [33] N. A. Tornqvist, Phys. Lett. B **590**, 209 (2004).
- [34] A. Astier *et al.*, Phys. Lett. B **25**, 294 (1967).
- [35] A. B. Wicklund, D. S. Ayres, D. Cohen, R. Diebold, and A. J. Pawlicki, Phys. Rev. Lett. **45**, 1469 (1980).
- [36] J. Weinstein and N. Isgur, Phys. Rev. Lett. **48**, 659 (1982).
- [37] J. Weinstein and N. Isgur, Phys. Rev. Lett. **27**, 588 (1983).
- [38] J. Weinstein and N. Isgur, Phys. Rev. Lett. **41**, 2236 (1990).
- [39] M. B. Voloshin and L. B. Okun', Soviet Journal of Experimental and Theoretical Physics Letters **23**, 333 (1976).

- [40] A. de Rújula, H. Georgi, and S. L. Glashow, Phys. Rev. Lett. **38**, 317 (1977).
- [41] M. Bander, G. L. Shaw, P. Thomas, and S. Meshkov, Phys. Rev. Lett. **36**, 695 (1976).
- [42] V. A. Novikov *et al.*, physrep **41**, 1 (1978).
- [43] N. A. Törnqvist, Phys. Rev. Lett. **67**, 556 (1991).
- [44] A. V. Manohar and M. B. Wise, Nuclear Physics B **399**, 17 (1993), hep-ph/9212236.
- [45] T. E. O. Ericson and G. Karl, Phys. Lett. B **309**, 426 (1993).
- [46] E. S. Swanson, Phys. Lett. B **588**, 189 (2004), hep-ph/0311229.
- [47] L. Maiani, F. Piccinini, A. D. Polosa, and V. Riquer, Phys. Rev. Lett. **71**, 014028 (2005), hep-ph/0412098.
- [48] B. A. Li, Phys. Lett. B **605**, 306 (2005).
- [49] K. K. Seth, Phys. Lett. B **612**, 1 (2005).
- [50] D. V. Bugg, Phys. Lett. B **598**, 8 (2004).
- [51] T. Skwarnicki, International Journal of Modern Physics A **19**, 1030 (2004).
- [52] J. Thompson, FERMILAB-TM-1909.
- [53] Accelerator Concepts Rookie Book,  
[http://www-bdnew.fnal.gov/operations/rookie\\_books/rbooks.html](http://www-bdnew.fnal.gov/operations/rookie_books/rbooks.html), 2004.
- [54] DØ, V. M. Abazov *et al.*, (2005), physics/0507191.
- [55] DØ, S. Abachi *et al.*, Nucl. Instrum. Meth. **A338**, 185 (1994).
- [56] A. Garcia-Bellido, S. Lager, F. Rizatdinova, A. Schwartzman, and G. Watts, Primary Vertex Certification in p14., 2004, DØ Note 4230.
- [57] A. Askew, *Measurement of the  $W\gamma \rightarrow \mu\nu\gamma$  Cross Section, Limits on Anomalous Trilinear Vector Boson Couplings, and the Radiation Amplitude Zero in  $p\bar{p}$  Collisions at  $\sqrt{s} = 1.96$  TeV.*, PhD thesis, Rice University, 2004.
- [58] DØ, L. Groer, DØ Calorimeter Upgrades for Tevatron Run II, in *Proceedings for the IXth International Conference on Calorimetry in Particle Physics, Annecy, France, Oct 9-14, 2000.*, 2000, DØ-Note 4240.

- [59] A. Khanov, HTF: Histogramming Method for Finding Tracks. The Algorithm Description, 2000, DØ Note 3778.
- [60] H. Greenlee, The DØ Kalman Track fit, 2003, DØ Note 4303.
- [61] E. Varnes, Track Reconstruction efficiency measurement with single muons, 2004, DØ Note 4317.
- [62] A. Schwartzman and M. Narain, Probabilistic Primary Vertex Selection, 2002, DØ Note 4042.
- [63] O. Peters, Muon Segment Algorithm, 2001  
[http://www-d0.fnal.gov/nikhef/muon\\_reco/segmentreco](http://www-d0.fnal.gov/nikhef/muon_reco/segmentreco)
- [64] F. Deliot, The Fit Algorithm in muo\_trackreco.  
<http://www-d0.fnal.gov/deliot/fitalg.ps>
- [65] L. Chevalier *et al.*, Track Parameter Error Matrix Propagation in Matter and Magnetic Field, Error Matrices Combination, 2001  
<http://www-clued0.fnal.gov/~tuchming/myprop.ps>
- [66] The DØ Muon Algorithm and Identification Groups, Content of the p13 Muon Thumbnail, 2003, DØ Note 4091.
- [67] Muon Certification page,  
[http://www-d0.fnal.gov/phys\\_id/muon\\_id/d0-private/certif/p14/index.html](http://www-d0.fnal.gov/phys_id/muon_id/d0-private/certif/p14/index.html)
- [68] L. Duflot and M. Ridel, The CellNN Algorithm: Cell Level Clustering in the DØ calorimeter, 2001, DØ Note 3923.
- [69] <http://www-cdf.fnal.gov/physics/new/bottom/030327.blessed-jpsixsec>.
- [70] J. Temple, R. McCroskey, and K. Johns, Upgrade of Level 1 Muon Trigger Logic for the v13 Trigger List, 2006, DØ Note 4566.
- [71] A. Maciel, S. Uzunyan, C. Leonidopoulos, and J. Kowalkowski, The L2-Muon Trigger Methods and Algorithms, 2005, DØ Note 4756.
- [72] D. Bauer, V. Lesne, and R. Jesik, Level 3 Muon Tools: p16 certification, 2004, DØ Note 4470.
- [73] F. Abe *et al.*, Phys. Rev. Lett. **79**, 578 (1997).
- [74] DØ, I. Bertram *et al.*, FERMILAB-TM-2104.